Eidgenössische Technische Hochschule Zürich
Swiss Federal Institute of Technology Zurich

D ERDW
EARTH SCIENCES

Master Thesis

Deep Alpine fluids: Origin, pathways and dynamic remobilization in response to hydraulic stimulations at the Bedretto Underground Laboratory for Geoenergies (BULGG)

Submitted to the Department of Earth Science ETH Zurich
Geological Institute, Engineering Geology

Under supervision of:
Dr. Bernard Brixel, Swiss Federal Institute of Technology (ETH), Zurich
Prof. Dr. Cara Magnabosco, Swiss Federal Institute of Technology (ETH), Zurich

Submitted by:
Moira Arnet
moira.arnet@gmail.com
15-065-709

Zurich, 30.10.2021

Abstract

A detailed knowledge of deep (>1km) groundwater systems and their hydrochemical variability is of high importance, since i) such systems play a central role in the future planned extraction and production of energy in Engineered Geothermal Systems (EGS) and ii) a better grasp on subsurface fluid chemistry has the potential to be a powerful monitoring tool in complex underground applications.

This thesis aims to contribute to the general understanding of hydrochemistry in deep fluids in systems comparable to EGS reservoirs and explain the observed hydrochemical variability also in terms of differences in source, recharge, percolation or geological conditions and to understand to what extent and how hydraulic stimulation causes mixing of different water types at reservoir scale. Therefore, a one-year hydrochemical monitoring program was done at the ETH rock laboratory BULGG (Bedretto Underground Laboratory for Geo-Energies) and the 5 km long BULGG host tunnel during a reservoir stimulation phase.

The results reveal high spatial isotopic and ionic variability of the BULGG groundwater along the 5 km long tunnel. The driving factor of isotopic variability is understood to be caused by an altitude-effect (with local isotopic anomalies, possibly caused by glacier and stream contributions), which is preserved in the subground by local recharge patterns, (sub-)vertical fluid flow and reduced lateral mixing.

The ionic variability is mainly caused by subsurface water-rock interactions, where the fluids are suspected to get overprinted by i) site-wide water-rock interactions with constantly productive geochemical sources leading to an linear increase of the sulfate, calcium, sodium and chloride concentration with generally increasing residence times and ii) water-rock interactions of locally variable source productivity, leading mainly to fluctuating fluoride and carbonate patterns in the fluids along the tunnel.

Three major water types could be accounted along the Bedretto tunnel, which are linked to the following three hydrochemical end-member specific characteristics: i) surface water source, ii) mineralisation degree and iii) local geochemical overprints. The hydrochemical end-member are interpreted as follows: (EM1) Low-elevation surface source of young age and local geochemical source for carbonate, (EM2) glacier-influenced, high-elevation surface source of young age and local geochemical source for fluoride, carbonate and sodium and (EM3) high-elevation surface source of more elevated age, local geochemical carbonate sink and sodium-excess source.

Long-term hydrochemical monitoring in the immediate vicinity of the stimulated reservoir could not be associated with any mixing signals, implying that i) mixing did not occur or ii) the contrast between end-members included in the mixing process is too low and the mixing signal got diminished by natural (random) temporal variability in the BULGG groundwater. However, short-term cross-hole monitoring revealed a clear mixing process, where the hydrochemical mixing signal characteristics indicate a complex signal involving mixing between several end-member waters present between the injection and production well.

Contents

List of Figures

List of Tables

1 Introduction

Enhanced geothermal systems (EGS) have the potential to generate baseload power in regions without volcanic or hydrothermal activity. In Switzerland, the energy strategy formulated in 2011 aims to replace conventional energy production with renewable sources by 2050, with EGS expected to provide a large proportion of supply. EGS energy extraction is accomplished by artificially increasing the permeability of crystalline rock in the deep, hot subsurface ($>$ 3 km) to create hydraulic connections between an injection well and a production well. This connectivity is then used to heat cold surface water, from which electricity is generated. An increase in permeability can be achieved by hydraulic stimulation, which can be divided into two main mechanisms: i) hydraulic shearing of existing fractures or the creation of new (induced) fractures by ii) hydraulic fracturing. Hydraulic stimulation is performed by injecting large volumes of water at high rates to pressurize the rock. Such procedures are associated with several as yet unresolved problems. One of the main obstacles observed is triggered earthquakes that are large enough to be felt at the surface. Costly operations like the Basel and St.Gallen pilot-and-demonstration projects in Switzerland, or the more recent pilot wells near the city of Pohang, South Korea, have had to be shut down because of unexpectedly large earthquakes or complex fluid behavior at wellheads. Such outcomes, unfortunately, highlight our limited ability to predict where injected fluids flow and how much they mix with indigenous fluids.

As a result, the last few years have seen a significant push for applied research through scaled-down, controlled hydraulic stimulation experiments involving highly-monitored scientific boreholes. Such experiments, usually carried out from deep tunnels, involve the injection and circulation of fluids at various pressures and temperatures to observe the nearby response of the rock mass, providing a unique opportunity to study how complex environments in the subsurface dynamically respond to anthropogenic fluid injections. In Switzerland, for example, comprehensive stimulation and circulation experiments at the 10m-scale were performed as part of the "In-Situ Stimulation and Circulation (ISC)" project at the Grimsel Rock Laboratory. The ISC experiment investigated the thermo-hydro-mechanical response of crystalline rocks down at 0.5 km depth, geologically belonging to the External Crystalline Aar Massif. Similar experiments are now planned over a larger scale (closer to actual reservoir conditions) in the Bedretto Underground Laboratory for Geoenergies (BULGG) in the Rotondo granite belonging to the Gotthard Massif in the External Swiss Alps. The depth of this laboratory is also deeper ($>$ 1 km), involving therefore higher pressures and deeper (hence warmer) fluids. A recent hydraulic stimulation campaign at BULGG is aimed at a soft geothermal stimulation, in which reservoir depths (between 200 and 400 meters below tunnel) are sequentially addressed. This technique of stimulating the reservoir in small steps is called 'multi-stage geothermal stimulation' and is patented by Geo Energy Suisse.[1] Multiple stimulation stages with progressively increasing injection volumes and continuous seismic monitoring ensure a controlled stimulation of the geothermal reservoir.

One aspect that is also currently tackled in the Bedretto Laboratory, which was overlooked in

[1] www.geo-energie.ch/tiefengeothermie/unsere-technologie/, accessed in September 21

Grimsel ISC experiment, is the importance of fluid chemistry. Groundwater chemistry in alpine massifs has been shown to be diverse, involving different water types emerging from multiple sources and various pathways (H. Schassmann (1984); Pastorelli et al. (2001); U. S. Ofterdinger (2001); Maréchal & Etcheverry (2003); Tomonaga et al. (2017); Bucher et al. (2012)). Such hydrochemical imprints can be disturbed in various ways by hydraulic stimulation works. Natural earthquakes triggered by hydraulic stimulations have been shown to mix fluids with different chemical compositions by e.g. creating new flow paths during stress build-up and failure on existing faults (Manga et al. (2012); Skelton et al. (2019); Borgonie et al. (2019)). To be able to detect mixing between end-members (in hydraulic stimulated systems, the end-members are generally constrained of i) the injection fluid and ii) the formation water), it is crucial to find conservative (i.e. chemically inert) environment-specific tracers. With knowledge of the conservative hydrochemical tracer concentrations of the mixed end-members, the degree of mixing (mix ratio) can be estimated which could further yield insights into flow processes and reveal the fate of injection fluids in a stimulated reservoir (Christophersen et al. (1990); Christophersen & Hooper (1992); Hooper (2003); Laaksoharju et al. (2008)).

Apart from mixing driven mechanisms (fluid-fluid interactions), stimulation-induced seismicity can also lead to many other processes causing a change in subsurface hydrochemistry, like water-rock interactions. A recent study performed at the Grimsel Rock Laboratory for example found coseismic spikes in helium and argon concentrations matching the onset of strain responses of hydraulic stimulations in a near by tunnel (Roques et al., 2020).[2] A further example of hydrochemical changes in relation with hydraulic stimulations have recently be shown by Stillings et al. (2020), who has observed at the Grimsel Rock Laboratory that reservoir-induced seismicity can correspond to a significant drop in pH. Grinding and breaking rock cores confirmed that microseismic damage can significantly acidify water, likely through the creation of surface silanols and silica radicals from fresh rock surfaces (Stillings et al., 2020).

This thesis aims to complete a one-year monitoring program to support the multi-stage stimulation treatments at BULGG planned in winter 2020 and spring 2021 based on hydrochemical analyses of fluids present in the Bedretto tunnel. The hydrochemical variability of the BULGG groundwater is targeted to potentially use the encountered variation to track artificially induced mixing processes between injection and formation fluids due to hydraulic stimulation (injection of several hundreds of cubic meters water). This allows to evaluate hydrochemistry as a tool to detect mixing at BULGG, as well as helps the interpretation of how fluids mix in the deep fluid system. Comprehensive characterization of initial hydrochemical variability in deep groundwater systems includes a general knowledge on fluid origin, fluid-fluid and water-rock interactions, water types and present hydrochemical end-members.

[2] According to Roques et al. (2020), this either reflect the release of radiogenic helium and argon accumulated between mineral grains in intact rock or the remobilization of stagnant fluids trapped in low-permeability regions (where the water is much older compared to water in permeable fractures, and therefore enriched in noble gases). Which of the two mechanisms is more likely, however, is still unclear and the authors acknowledged some uncertainties in the identification of hydrogeochemical end-members, revealing the importance of early baseline geochemical characterization

2 Study Site

2.1 Site Location and Infrastructure

The Bedretto laboratory, located in the Central Swiss Alps near the city of Airolo, Switzerland, is built around the central portion of a 5'221 m long tunnel accessed through the Ronco portal, about 10 km west of Airolo (figure 2a). Originally the tunnel was used as an adit to the Furka Base railway tunnel during construction between 1973 and 1982. This tunnel (hereafter referred to as the Bedretto tunnel) has been retrofitted recently to support the construction of an underground rock laboratory 2 km from the Ronco portal led by ETH Zurich. This laboratory includes multiple scientific boreholes and is located about 1.0 km below surface. Ventilation and power are now provided from the Ronco portal up to TM 2300.[3] Inflows are drained across the entire 5.2 km section of the tunnel by gravity towards the Ronco portal (tunnel slope of 0.2 - 1.7% (Jordan, 2019)). Only few sections across the tunnel have been shotcreted or supported by steal arches (structural support is mainly required near the Ronco portal), providing therefore a unique opportunity to sample fluids continuously over more than 5 km. The tunnel is of about 3 to 4 meters height.

The Bedretto tunnel cuts through a high-relief alpine catchment of approximately 40 km^2, culminating at the 3192 meter high Pizzo Rotondo mountain peak. The study area's land surface varies from 1400 and 3192 meter above sea level (m asl). Half of the area lies above 2500 m asl, reflecting the steep topography: 50% of the slopes are larger than 30°, and 11% of them exceed 50°. Only a small portion of the less elevated and steep areas on the northern Bedretto valley flank are vegetated.

Figure 1: The Bedretto Underground Laboratory for Geoenergies (BULGG) after 2 kilometers in the Bedretto tunnel.

[3]TM = tunnelmeter from the Ronco portal.

2.2 Early Studies

Early studies in the region have been conducted by Hafner (1958) and (Steck et al., 1976), who provided an extensive petrographic description of the Rotondo granite and adjacent lithologies. The Bedretto tunnel construction was accompanied by Schneider (1985) and Keller & Schneider (1982), who focused on structural, geological and hydrological characteristics of the Rotondo granite revealed during the tunnel construction. Later, Priest (1993) performed scanlines surveys. V. H. Lützenkirchen (2002) investigated the characteristics of structural features in the study area and introduced a classification scheme of the existing structural features, which is applied in this thesis. Subsurface flow processes were investigated by U. S. Ofterdinger (2001) based on a hydrochemical survey of tunnel inflow in the northern most tunnel section ($\sim$ 1.5 km from the Furka Base tunnel), including environmental isotopes, major ions and standard water quality parameters.

2.3 Geological Setting

2.3.1 Geological Units and Mineralogy

Geologically, the Bedretto tunnel is situated in the Gotthard Massif, which belongs to the External Central Massifs of the Swiss Alps and consists of prevariscan polymetamorphic crystalline basement rocks such as paragneisses, migmatites, amphibolites, serpentinites (V. H. Lützenkirchen, 2002), as well as magmatic intrusions of Variscian age (Zangerl et al., 2006).

Figure 2b provides a geological cross section (Keller & Schneider, 1982) along the tunnel, illustrating the main units. The vast majority of the tunnel intersects the Rotondo granite, a massive dome-shaped granitic Variscian intrusion, light grey colored and characterized by a fine-grained and equigranular fabric (Hafner, 1958). This granite is mostly isotropic but developed at some locations a weak foliation with a NE-SW strike (V. Lützenkirchen & Loew, 2011). Zircon dating revealed an age of 294.3 $\pm$ 1.1 Ma (Sergeev et al., 1995). The Rotondo granite host multiple NE-SW striking and steeply dipping mafic dikes also known as lamprophyres (Oberhänsli, 1986) (one example intersects the Bedretto tunnel at TM$\sim$2794 with a thickness of about 4 - 5 meters). Aplitic dikes also occur, but are substantially smaller (about 1 m) in comparison to mafic dikes (Hafner, 1958). The contact between the Rotondo granite and gneisses from the basement of the Gotthard massif is sharp, and occurs at TM 1143. The geological unit in direct contact with the Rotondo granite, is known as the Prato-series (PS) and consists of banded, mesocrate biotite schists, felsic mica paragneisses and amphibolites. Near the Ronco portal, the series transitions to (partly carbonate) garnet bearing hornblende rocks (hbl-schists, gneisses and amphibolites) belonging to the Tremola-series (TS) (Hafner, 1958). Within the TS, the tunnel cuts through a landslide (which is characterized as a flexural toppling structure and about 350 meters long, see figure 2) (Vlasek, 2018).

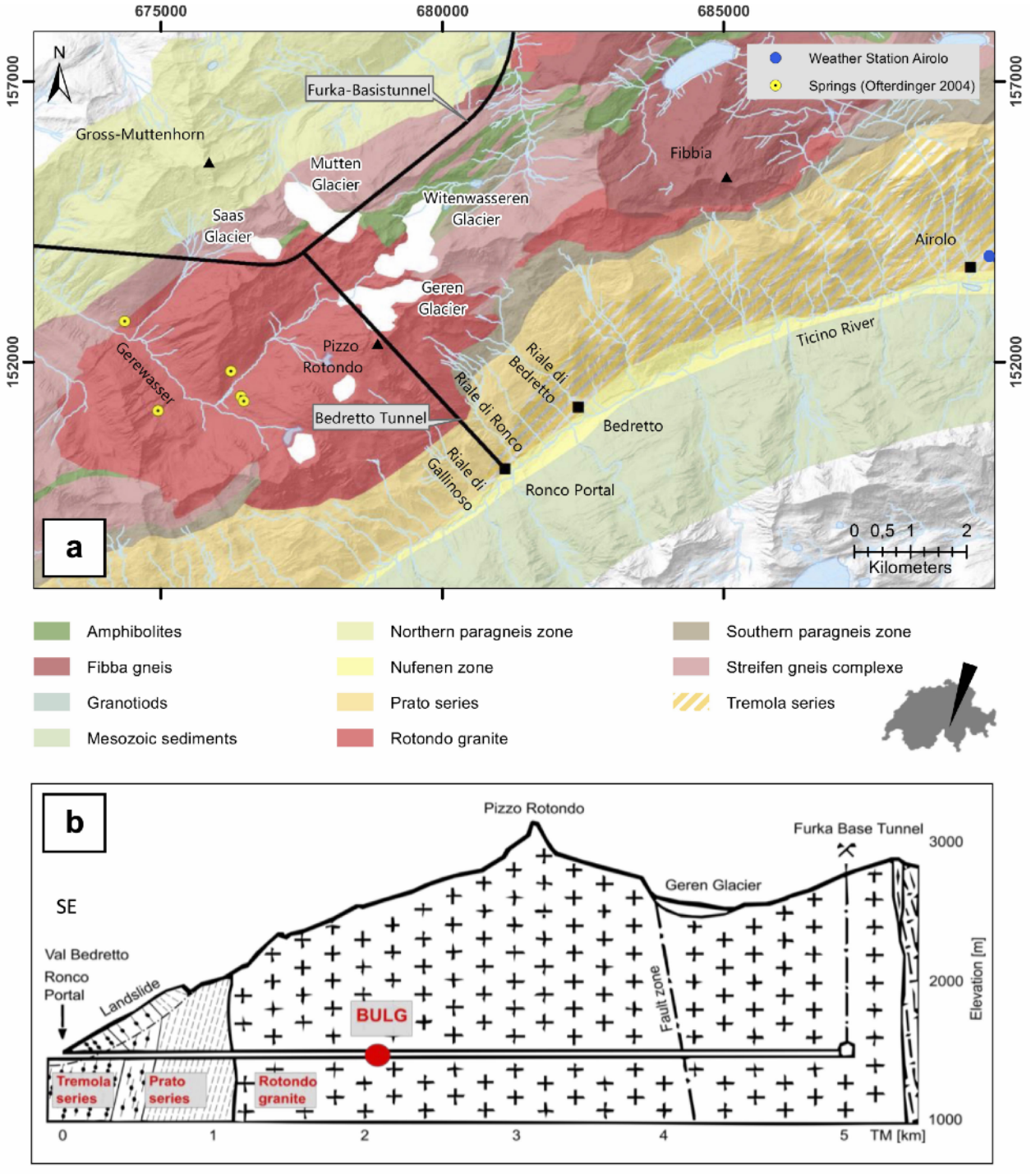

Figure 2: (a) Geological-tectonic map of the study area including present surface water courses (Source: Geovite ETHZ/ Geological Atlas 25 Swisstopo, accessed in January 2021). (b) Geological cross section along the Bedretto tunnel modified from Keller & Schneider (1982).

The bulk mineralogical assemblage of lithologies present across the study area is summarized in table 8 (Appendix A). The mineralogy of the Rotondo granite is composed of 25% to 35% quartz, 20% to 40% potassium feldspar, 20% to 35% albite (however, note that the albite content decreases gradually towards the margin of the Rotondo granite body to below 10 %), 2% to 7% anorthite, and 5% to 10% biotite. Accessory minerals (< 1%) in the Rotondo granite include garnet, chlorite, epidote, apatite, zircon and ores (Hafner, 1958). Not reported by Hafner (1958), but observed during the construction and during a surface field trip in August 2020 is the presence of pyrite in the Rotondo granite (U. S. Ofterdinger, 2001).

The mineralogy of the major lithologies in gneisses (Prato-series/ Tremola-series) shows high variability, as seen in table 8 (Appendix A). Compared to the Rotondo granite, the gneisses are in general characterized by a higher biotite content (PS) and additional major contents of primary minerals like epidot, carbonate, hornblende, chloride (TS) and garnet (PS). The quartz and feldspar content is generally (with exceptions) lower in the gneiss units compared to the Rotondo granite. The albite content in the Rotondo granite plagioclase is generally lower than the percentage observed in the gneissic units (TS/PS).

V. Lützenkirchen & Loew (2011) provide a comprehensive mineralogical description of fault rocks in the Rotondo granite and characterized secondary mineral products such as chlorite (secondary biotite product), sericitization and corrosion of feldspars, corrosion of quartz and precipitation of albite, zeolites, carbonates and pyrite (synkinematic minerals formed during brittle deformation).

2.3.2 Structural Geology

The Rotondo granite is dissected by brittle structures extending over a large range of scales, from meter to decameter-scale fractures up to km-scale brittle and brittle-ductile fault zones and ductile shear zones (V. Lützenkirchen & Loew (2011) and Jordan (2019)). Priest (1993) distinguished four major fracture sets (FS) (table 1). The first set, striking perpendicular to the tunnel (FS1 in table 1), and the E-W striking fracture set (FS2 in table 1) include the largest features (fault zones) in the study area (V. H. Lützenkirchen, 2002).

Table 1: Mean Orientation of the four major fracture sets (FS) present in the study region based on the dataset of Priest (1993) and Schneider (1985), adapted from U. S. Ofterdinger (2001).

Fracture Set	Mean orientation strike/dip
FS1	049/75 SE
FS2	080/83 SE
FS3	140/86 SW
FS4	170/79 SW

The total fracture spacing evolution along the Bedretto tunnel was estimated by V. H. Lützenkirchen (2002) (also based on previous structural studies performed at BULGG by Priest (1993), Schneider (1985)) and visualised in figure 12. It is apparent, that the fracture spacing in the front part is in between 50 - 100 meters, where the highest fracture spacing was accounted around the BULGG laboratory. From the laboratory towards the Fukra-Basetunnel portal, the fracture spacing decreases gradually. The tunnel section between TM∼4000 - TM 5200 is defined by very low fracture spacing (in between 10 - 20 meters).

V. H. Lützenkirchen (2002) estimated the persistency of major fault zones (present in FS 1 and FS 2) to be regional, defined in his study as at least 2 km. The less prominent features (mainly in FS 3 and FS 4) can be traced over several 10's of meters (Jordan, 2019) .

(a) (b)

Figure 3: Two examples of brittle fault zones in the Bedretto tunnel. a) Fault zone at TM1993 (alternatively referred to as 'badboy'), where the core material has completely decomposed to fault gouge materials (Swiss Army knife for scale). (b) Brittle-ductile fault zone including a central fault filled with cataclasites and fault gouge material (Field hand meter for scale).

According to V. H. Lützenkirchen (2002), approximately 73% of fault zones in the Bedretto tunnel nucleated on pre-existing ductile structures. These faults, according to V. H. Lützenkirchen (2002), developed damage zones of several meters around a central principal fault core. Detailed structural

mapping across the tunnel indicates that fault cores are filled with cataclastic material and tend to be surrounded by dense fracture networks. In some cases, this cataclastic material has been completely decomposed into fault gouge materials of several centimeters thickness (figure 3). The dark green-grey gouge material has a relatively high content of fines, which can be rich in mica, biotite and/or clays (the mineralogy has its origin in the mica-rich foliation planes) (V. H. Lützenkirchen, 2002).

Most fault zones in the Bedretto tunnel (80%) are brittle-ductile fault zones. These are generally less than 4 m wide, however, some exceed 10 meters. Such faults are generally associated with high inflows and are responsible for the major water inflows in the Bedretto tunnel (see section 2.4.3). Brittle fault zones (27% of the fault zones mapped by V. H. Lützenkirchen (2002)) developed, instead, less densely fractured damage zones and lack a fault core. Their orientation is generally foliation sub-parallel.

2.4 Hydrological Setting

2.4.1 Surface Waters

Infiltration into the mountain block may derive from varying sources, including: snow and rain precipitation, surface waters (lakes, ponds and streams), glaciers or subsurface ice (Slaymaker, 1974).In the study region, the mean annual precipitation (MAP) over the last 60 years can be estimated from nearby weather stations, where MAP amounts to 1640 mm (measured in Airolo at 1170 m asl) to 1875 mm (measured in Grimsel at 1980 m asl).[4] Snowfall ($>$ 4 days/month) occurs in Airolo from November to March and rainfall ($>$ 4 days/month) between from April to November.[5]

Further surface water bodies are formed by glaciers, which are present in the northwestern study region. Three major glaciers are located in the vicinity of the Bedretto tunnel (figure 2a). The closest one is the Geren glacier, which is situated directly above the northern part of the tunnel and drained into the Geren valley towards the Rhone river. The Witenwasseren glacier is located north of the Witenwasserenstock, where glacial meltwaters drain towards the Reuss river, which flows in a northeasterly direction. The Mutten glacier lies on the northwestern side of the Läckihorn mountain peak and also drains into the Reuss river. Two smaller glaciers are located on the western side of the study area. On the Rotondo Pass, southwest of the Rotondo summit (bounded by the Chüebodenhorn and Pizzo Rotondo), is the Pizzo Rotondo glacier. On the southeastern side of the Chüebodenhorn is the Chüeboden glacier. Another small glacier close to the surface projection of the Furka Base tunnel is the Saas glacier. Many of these glaciers have formed young glacial lakes, which were formed by the deglaciation.

Several streams drain the southeastern high-altitude (2500-2600 m asl) part of the study area close to the geological contact between the Rotondo granite and the prevariscan basement. Major tributaries close to the Bedretto tunnel from northeast to southwest are the Riale di Bedretto, Riale di Ronco and the Riale di Gallinoso. All streams flow into the Ticino river, which flows towards Airolo. U. Ofterdinger et al. (2004) reports a few notable springs in the Geren valley western to

[4] www.meteoschweiz.admin.ch, accessed in January 2021

[5] www.snow-forecast.com/resorts/Airolo/history, accessed in January 2021.

the Pizzo Rotondo (figure 2a). On the north-eastern side of the Bedretto tunnel, only one larger spring is known (coordinates: 2'680'523.5 m, 1'151'135.5 m), located in the Prato-series close to the Rotondo granite contact and discharges into the Riale di Ronco (discharge estimated of about 0.5 m^3/min, June 21).

2.4.2 Recharge and Groundwater Conditions

The recharge condition of mountain blocks and the internal percolation of fluids are influenced by many factors, such as the meteorological inputs, the topography (e.g. the catchment area, the exposition and the slope), the land use and the hydrogeological conditions of the subsurface (Gurtz et al., 1990). Groundwater recharge in the study region was investigated by U. Ofterdinger et al. (2014) using a numerical model to constrain recharge rates of hydrotopes (i.e. hydrologically homogeneous areas) across the study catchment.[6] A detailed distribution of the resulting hydrotopes can be found in figure 4. U. Ofterdinger et al. (2014) report that the hydrotopes of small glaciated areas located around the Leckihorn, Saashörner and the Rotondo summmit show the largest recharge rates, at about 40 x 10^{-4} m/d. Mid-altitude slopes and valley bottoms see moderate recharge rates in comparison, around 15 x 10^{-4} m/d. The hillslopes beneath the Saashörner and on the northern down-/mid-slope section of the Bedretto valley appear to provide substantial recharge to the Bedretto tunnel. According to U. Ofterdinger et al. (2014), nearby glaciers are the dominant sources of recharge to the northern part of the tunnel. The glaciated area between Leckihorn and Witenwasserenstock provides most of the recharge throughout the northernmost part of the tunnel, while the Geren glacier contribution is the highest around 1.5 km from the Furka tunnel entrance and decreases towards the northern tunnel portal.

Groundwater flow in fractured aquifers, such as formed by the Rotondo granite and surrounding gneiss units, depends mainly on water-conducting features, whereas water flow through the matrix is negligible at the time scales considered in this study (Brace (1980); Barton et al. (1995); Caine & Forster (1999)). Water-conducting features are zones of enhanced hydraulic conductivity, mainly formed by structural features as open fractures or fault zones generated during brittle deformation periods and built up a long-term stable flow pathways. As mentioned in section 2.3.2, the structural features at BULGG mainly strike perpendicular to the tunnel what supports fluid flow along this orientation.

The enhanced hydraulic conductivity in conductive zones causes a highly channelized flow field pattern in fractured aquifers (up to few l/s). One can estimate this property of the bulk rock by determine the hydraulic conductivity (k) of a rock mass. Masset & Loew (2010) determined the effective hydraulic conductivity (K_{eff}) of the Rotondo granite and the high grade metamorphic prevariscan gneisses in the study area based on discharge measurements in the Bedretto tunnel.[7] Masset & Loew (2010) report hydraulic conductivities in the order of 10^{-8} m/s at tunnel depth, which is consistent with other crystalline rocks in the region. The hydraulic conductivity of gneisses

[6]The model is based on the following input data: Meteorological data, the topography evolution (includes the elevation, exposition and slope of the catchment area), the land use and soil characteristics.

[7]These effective hydraulic conductivity estimates are derived from initial cumulative inflows (see figure 12) recorded every 100 m during tunnel excavation (Masset & Loew, 2010)

appears to be higher at shallow overburden depths (10^{-4} m/s between 0 - 300 m). The hydraulic conductivity of the Rotondo granite does not show any clear trend with depth.

The age of the groundwater in the northwestern tunnel section has been determined to 1.0 to 1.5 years (U. S. Ofterdinger, 2001), what suggests very short transit times for percolating fluids that reach the tunnel.

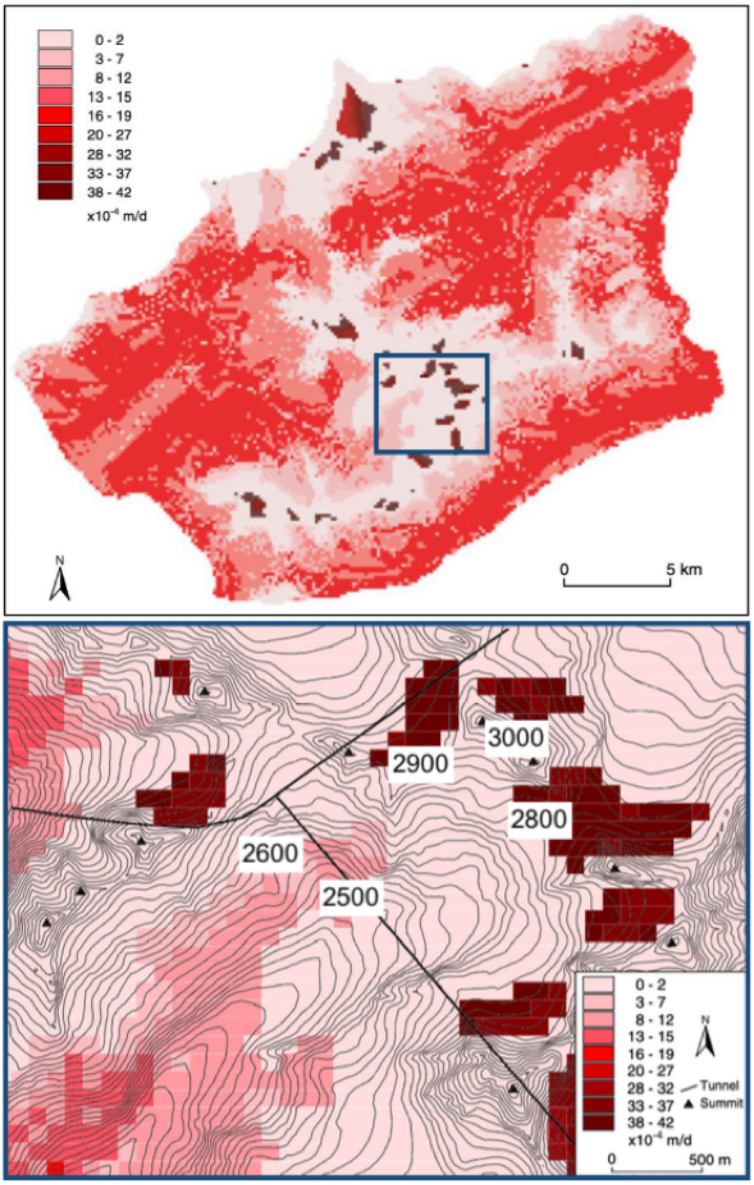

Figure 4: Groundwater recharge rates and areas estimated based on a hydrological model of the study catchment modified from U. Ofterdinger et al. (2014). The subfigure below is a zoom-in of the blue rectangle in the subfigure above. The lower subfigure shows the northwestern section of the Bedretto tunnel (black line, striking NW-SE) and its junction with the Furka Base tunnel (black line, striking NE-SW). The white rectangles display the elevation in meter above sea level.

2.4.3 Tunnel Inflows

Hydrogeological and structural studies in the Bedretto tunnel and region have shown that fluid flow is not uniform in the Rotondo granite and alternates instead between dripping zones and continuous inflow zones. Parts in the tunnel, as for example between TM 2000 - TM 2100 the low fracture density causes results in dry to dripping zones (in the order of 0.01 l/s/ discrete fracture). Zones of high fracture frequency on the opposite are wet and defined by many water inflow zones, which is especially visible in the northern part of the tunnel (TM 4200 - TM 5100, conductive zone). Very high (and rather condensed) inflows are furthermore connected to isolated major structural features like (brittle-ductile) fault zones (Masset & Loew, 2010). The highest inflows over 100 meter in the Bedretto tunnel are restricted to the following sections and major structural features: TM 300 - 400 (landslide scarp), TM 1300 - 1400 (brittle-ductile fault zone at TM∼1300), TM 2800 - 2900 (brittle-ductile fault zone at TM∼2850) and TM 4200 - 4300 (densely fractured rock mass)(Masset & Loew, 2010).

During the tunnel construction three major inflow zones were reported; 40 l/s at the brittle-ductile fault zone TM 2850, 130 l/s across the landslide (TM 180 to 360) and 35 l/s at the TM 1300-fault zone (Masset & Loew (2010); V. H. Lützenkirchen (2002)).[8] The Bedretto tunnel construction was finished almost thirty years ago and since the initial measurements were taken, the flow rate adjusted to the decreasing hydraulic gradient. The tunnel discharge from the fault zone at TM 1300 was in 2021 estimated to 16 l/s, which is based on a flow meter measurement before and after the fault zone (TM 1260 - TM 1333).[9] When comparing the measurements taken during construction (initial inflow) with measurements conducted in 2021, it is apparent that the flow rate of the 1300 fault zone decreased of at least 50% since the initial measurements.

[8] An initial discharge rate of groundwater inflow shortly after the tunnel construction is mainly connected to the release of water stored in the fractures (Moon & Fernandez, 2010). Only after this period (lasting a few hours), the groundwater level starts to be lowered (providing no infinite contribution of a surface water body is present), what decreases the hydraulic gradient (what drives fluid flow) and thus as well the fluid discharge into the tunnel.

[9] Measurement was conducted by Peter Achziger (Archen University) on the 05.05.2021

3 Research Goals

This thesis has two main goals. The first one (objective 1) is to hydrochemically characterize the natural tunnel inflows (originating from natural seeping fractures and boreholes) and surface water bodies in the proximity of BULGG. The temporal and spatial hydrochemical variability in the subsurface is intended to be used to estimate the water origin and sources, the major water-rock and fluid-fluid interactions, as well as the water types, and their hydrochemical end-members in the study region.

The second objective (objective 2) is to interpret potential shifts in hydrochemistry due to artificial injections at revervoir scale and provide insight into how hydraulic stimulation may potentially remobilize and mix different water types at BULGG.
The research questions motivating this thesis are therefore stated as follows:

- Can contrasting water chemistries in deep ($>$ 1 km) mountain blocks, as in the Bedretto laboratory, be linked to regional water sources, geology, and flow paths?
- Should we expect hydraulic stimulation to mix different water types?

4 Methodology

4.1 Workflow

The methodological workflow followed to meet the objectives is shown in figure 5. The methodology can be subdivided in the following three steps: i) sample collection, ii) analytical data acquisition and iii) data analysis.

Water samples were collected in monthly subsurface surveys between August 2020 and July 2021, surface surveys in the summer 2021 and in the context of hydraulic stimulations taking place at the Bedretto Underground Laboratory in November/December 2020 and March/May 2021.

To be able to extract the hydrochemical parameters of interest of the sampled water (standard parameters, major ions and stable isotopes), both in-situ (hand field meter) and analytical methods (laboratory instruments) have been used.

The explorative methods then were performed to evaluate the different groundwater patterns and properties, as well as to illustrate mixing processes during hydraulic stimulation. The PCA-based Cluster Analysis (CA) was performed to be able to spatially distinguish between different water types (clusters) and their relation to each other. The End-Member (EM) Analysis was done to identify present hydrochemcial end-members contributing to different water types, as well as their associated characteristics and major underlying processes accounting for the hydrochemical variability at BULGG.

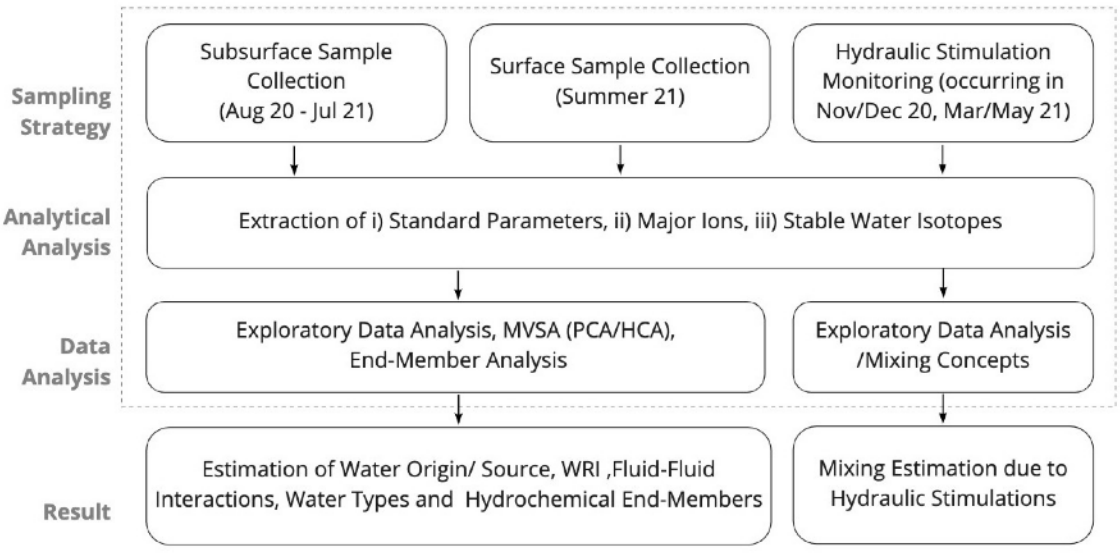

Figure 5: General overview of the methodological workflow (gray box) used to obtain the results needed to address the objectives.

4.2 Sampling Strategy

4.2.1 Subsurface Sampling

Figure 6 illustrates the sampling sites along the Bedretto tunnel and in the Underground Rock Laboratory BULGG. Four examples of sampling sites in the subsurface are visualized in figure 7.

Samples from natural tunnel inflows were obtained from a total of 58 locations. 54 sampling sites are related to natural water inflows along the Bedretto tunnel, mainly discrete fractures, zones of densely fractured rock or fault zones intersecting the tunnel. A few number of sites are connected to tunnel inflows in smaller (Ø 10cm) boreholes in the tunnel sidewalls (borehole length is unknown, observed at e.g. at TM 901, TM 755A and TM 2794). In total, 9 sampling locations correspond to deep inclined boreholes implemented at the BULGG laboratory, including 8 monitoring (up to 200 m deep) and two 400 m deep stimulation boreholes. The boreholes enabled sampling of an integrated hydrochemistry over borehole depth. Temporal and long-term packer installation furthermore allowed data acquisition in isolated depth intervals. The boreholes ST1, ST2, CB1 (/formerly MB1), CB2 (/formerly MB2), CB3 (/formerly MB3), CB4 (/formerly MB4) were occasionally sampled during 2020. The in a later stage implemented MB5, MB8 (both beginning of 2021) were additionally sampled during 2021. The observation boreholes CB1, CB3 and CB4 were only sampled during 2020, since they were grouted after the first stimulation campaign in November/ December 2020. CB2 was equipped with a long-term multi-packer system, allowing sampling using sampling tubes connected to the respective interval. During the stimulation periods, the stimulated borehole were packed to be able to individually stimulate certain borehole sections (for detailed borehole sampling information, see table 9, Appendix B).

Each site is connected to a timeseries, where most of the sites are sampled on a monthly basis, as mentioned above (expect borehole fluids, where the sampling date depends on the accessibility of borehole fluids). Some sampling sites were sampled once only to validate the general water quality spatial evolution in the data and to increase the resolution of an an observed trend.[10] The first sample is collected at TM 216 and the last sample at TM 5132, providing an average frequency of one sample every ∼85 m. Except for the samples between TM 216 - TM 1040, all sampled fractures and boreholes are situated in the Rotondo granite. The criteria used to select sampling sites was mainly based on inflow rates large enough to allow sampling 200 mL in reasonable time (< 10 min). The sampled water should also avoid direct contact with artificial support such as corrugated pipes or steel arches. However, for the sampling site at TM 3750 (big fault zone supported with a steel arch) and TM 1993 (fault zone 'BadBoy' with a water collection installation consisting of aluminium grid and plastic tubes around the fault) this was not possible.

Occasionally samples from the ditch water (drain from natural tunnel inflows) were taken. Most ditch samples were taken at TM 2097, which is before the BULGG laboratory (facing the draining direction) and source of the used injection water during hydraulic stimulation.

[10] Such samples were only sampled once and are located at TM 216, 340, 363, 1040, 2945, 4192, 4198, 4240, 4250, 4253, 4268A, 4268B, 4288, 4345, 4406A, 4406B, 4448, 4589, 5000, 5050.

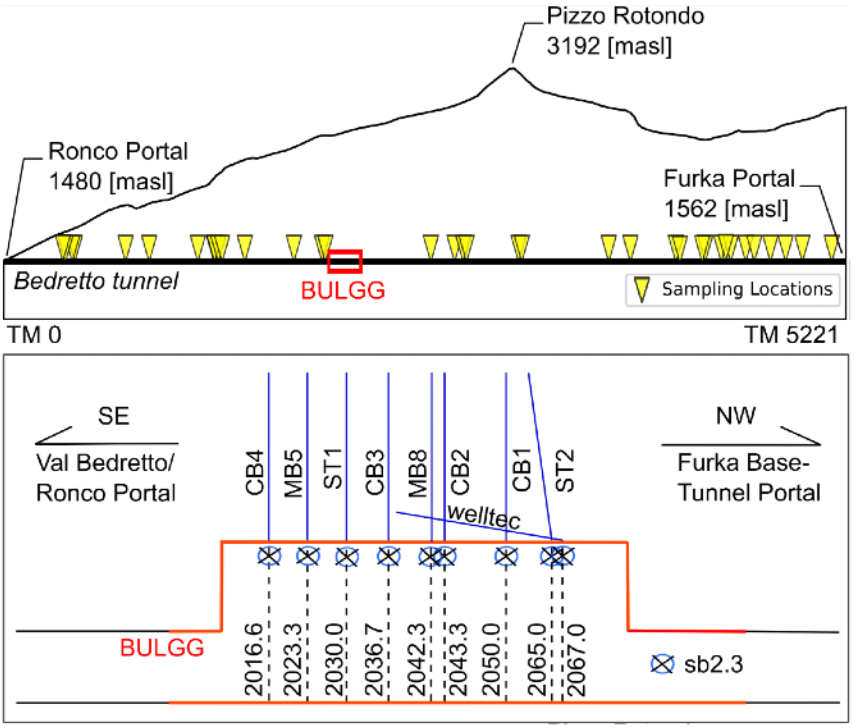

Figure 6: Conceptual cross-section of the sampling sites along the Bedretto tunnel (above, marked with yellow triangles) and the location of the sampled boreholes in the BULGG laboratory (below). Note that the figure was not drawn to scale.

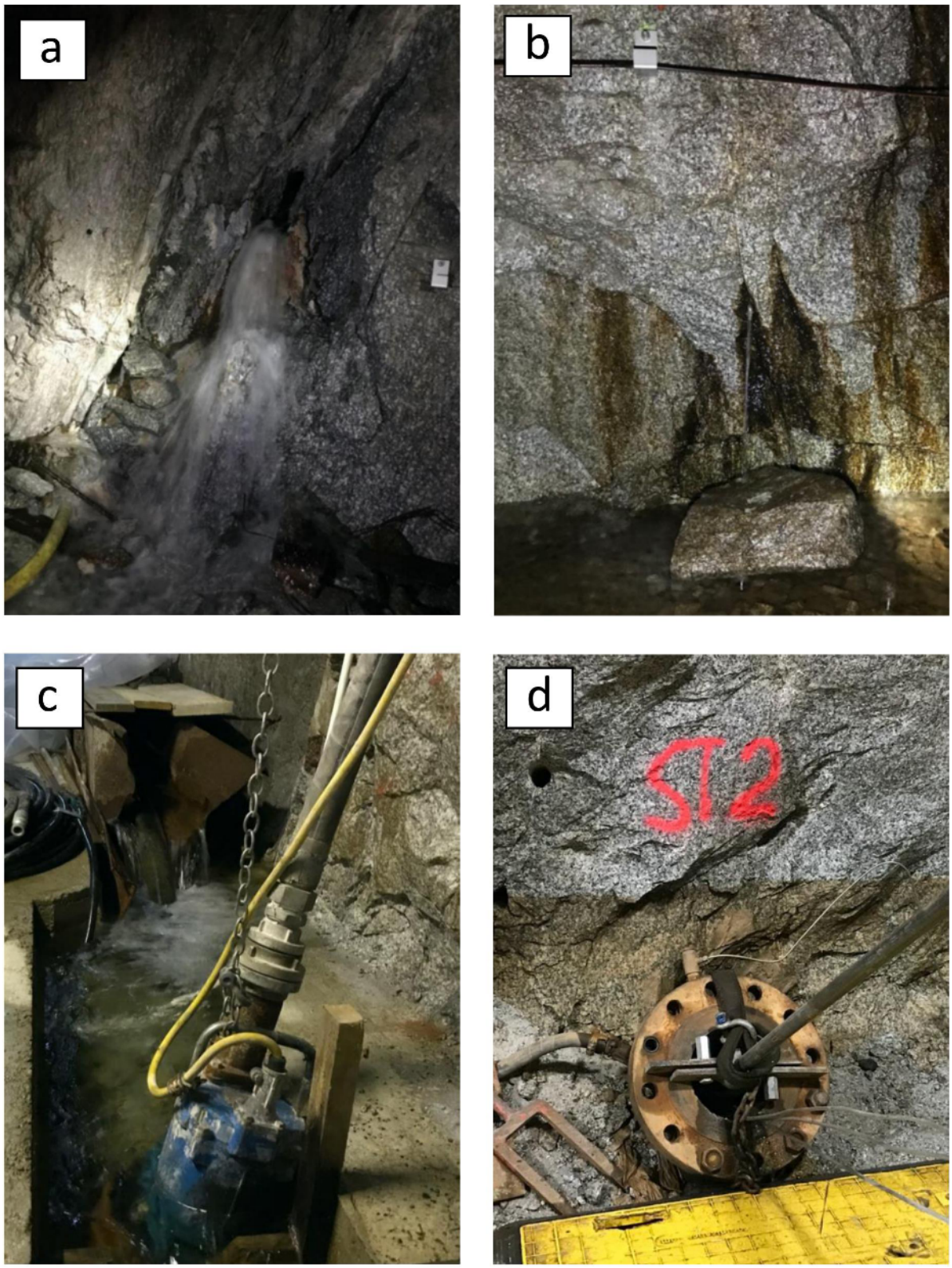

Figure 7: Four examples of sampling sites in the Bedretto tunnel. (a) High discharge rate at a seeping fault zone (sampling location TM2848 - alternatively referred to as 'NiceGirl'), (b) Intermediate flow rate at discrete fracture inflow (sampling location TM 4447), (c) Ditch water sampling location at TM∼2097, (d) Borehole fluid sampling location at the ST2 wellhead (TM 2065).

4.2.2 Surface Sampling

All surface sampling locations collected in the context of this thesis can be found in the map, displayed in figure 8.

The precipitation samples consist of three snow and four rain samples. Snow samples were collected at the Ronco portal from snow packs. The rain water samples were taken at the ETH-barracks close to the Ronco portal and represent an integration of rain water over one day.

A comprehensive sampling survey has taken place during a field trip on the 27.07.21, where 14 streams, the Ticino river (at 2'681'253 m/ 1'150'031 m) and one spring were sampled. The sampling locations are located on the northern flank of the Bedretto valley and include the streams Riale di All'Acqua, Riale di Bedretto, Riale di Ronco and Riale di Gallinoso and a spring next to the Riale di Ronco (coordinates: 2'680'523.5 m/ 1'151'135.5 m, hereafter referred to as 'Ronco spring'). All streams were sampled on valley floor elevation (1500 - 1600 m asl) and upstream (between 1900 - 1980 m asl), to be able to detect potential changes in the water constituent.

A second field trip was executed on the 21.08.21, where the focus was laid on sampling glacier melt waters and glacier lakes around the Rotondo summit. In total, 1 stream and 2 glacier lakes were sampled. The sampled stream was originating from a snow pack (~20x10x5 m^3). The lakes are both feed by the Chüeboden glacier and snow packs (note that the data from this field trip only consists of standard water quality measurements).

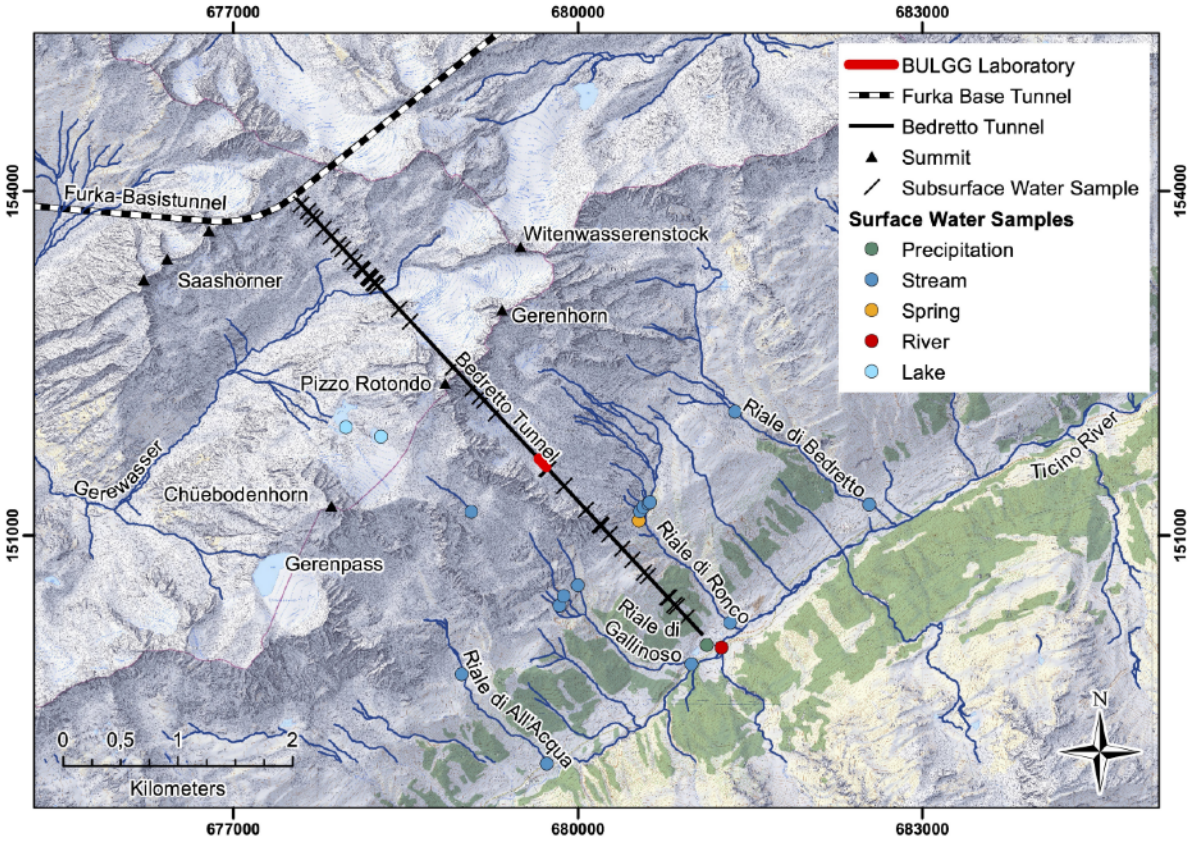

Figure 8: Overview of the sampled surface sites. Source: Geovite ETHZ (accessed in September 2021).

4.2.3 Hydraulic Stimulation Monitoring

To detect potential mixing effects in the reservoir due to hydraulic stimulation, it was attempted to monitor in i) the close vicinity of the stimulated reservoir during the sampling year (requires a long-term hydrochemcial monitoring) and ii) within the stimulated reservoir during a specific hydraulic stimulation (requires a short-term cross-borehole monitoring). The timeline of the stimulation stages are illustrated in Figure 9.

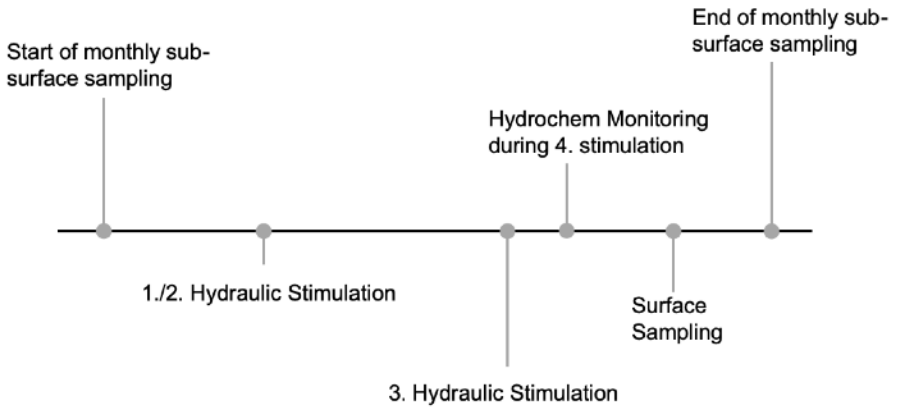

Figure 9: Timeline for the multi-stage hydraulic stimulation stages performed by GES during the sampling period in 2020/2021.

Long-term Monitoring

To detect cumulative hydrochemical shifts in the vicinity of the stimulated reservoir during the sampling year, the best possible temporal resolution was pursued at the sampling sites of interest. Two sites were chosen for the long-term monitoring program, namely the borehole CB2 and the fracture at TM 1993 (natural tunnel inflow). The CB2 borehole was of special interest, since the installed long-term (unchanged) multi-packer system allowing repeated sampling of different intervals (depths) during the entire sampling period. In CB2 four samples were taken between end of December 2020 and end of May 2021. The fracture at TM 1993 was of interest, since it is the closest sampled natural seeping fracture to the laboratory and a hydraulic connected to the reservoir is likely. This site has been sampled on 24 days distributed over the sampling period.

Short-term Monitoring

The cross-borehole short-term monitoring in the stimulated reservoir was conducted on the 23.05.21, where the ST1 (interval 1 and 2) outflow was monitored during the 220 m^3-injection into the bottom part of the ST2 (last $\sim$ 60m interval of the 400m deep stimulation borehole).[11] The distance

[11]The hydraulic stimulation was executed on the 23.05.21 by Geo Energy Suisse (GES) and was subdivided into three stages. In a first stage hydrotests for formation characterization were performed, which were related to a injection rate of 9 l/min in ST2. Three an a half hours later (1:24 pm, CET/ 11:24 am, UTC), the injection rate was increased to 30 l/min corresponding to a down hole pressure of about 23 MPa (Stage 2). At 3:39 pm (CET)/1:39 pm (UTC) the stage 3 started, connected to a injection rate increase to 90 l/min ($\sim$25 MPa injection pressure). The injection was stopped at 8:02 pm (CET)/ 6:02 pm (UTC).

between the injection and monitored intervals was 66 meters.

During the stimulation, the downhole (injection) pressure of the stimulated part in ST2, the downhole pressure of the ST1 interval 2 were monitored by Geo Energy Suisse (GES). GES furthermore installed a flow meter to continuously measure the flow rate of the ST1 interval 1 and 2 tunnel inflow. The outflow of the flow meter was connected to a pipe, leading the water to the hydrochemistry monitoring system (the monitoring system set up can be seen in figure 10). There, the electric conductivity (EC) was measured continuously before, during and after the injection period. The electric conductivity (calibrated to 25°C) of the ST1 interval 1 was measured every second during the stimulation of ST2 between the 22.05.2021 19:54:00 pm (UTC time) until the 25.05.21 13:45:17 pm (UTC time) with a temperature-conductivity logger (QL40-FTC). The electric conductivity (25°C), pH, temperature and TDS was additionally measured with a field meter (pcstestr 35) started 3 minutes after opening the borehole interval every ten minutes until the EC-logger was installed. The frequency was then extended to a measurement every hour (except during the night hours).

To be able to extract further hydrochemcial parameters (suitable tracers) of the out flowing ST1 water, 100 ml samples were taken every half hour during the expected mixing signal.

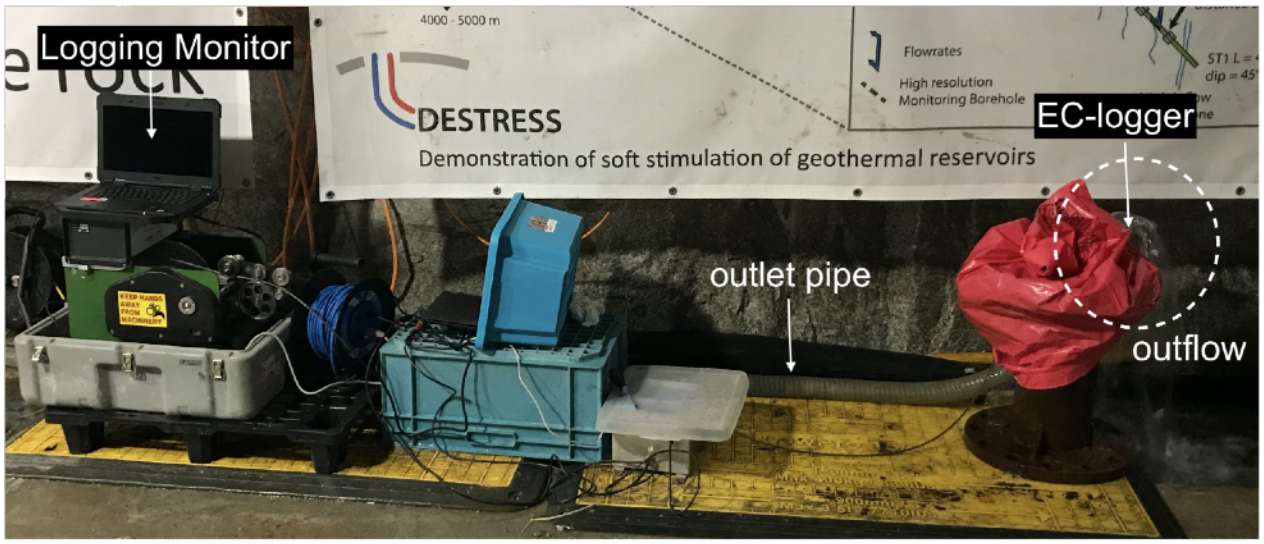

Figure 10: Temporary monitoring set-up during the hydraulic stimulation event on the 23.05.2021, measuring the electric conductivity of the ST1 interval 1 outflow while ST2 was stimulated.

4.3 Data Acquisition

All parameters of interest and data compiled as part of this thesis are summarized in table 2. Standard water quality measurements were taken directly on site, as well as the probes for major ion and isotopic analyses. These were collected in 100 mL sealed polyethylene bottles and stored at 4°C (up to one month until analysis), following standard procedures for the sampling and storage of groundwater samples. A more detailed description of the sampling strategy on site, sample labeling and storage can be found in the "Standard Operating Procedures" (SOP) file in the Appendix C.

Table 2: Overview of the hydrochemical parameters collected in the context of this thesis.

		Parameter	Unit
Standard parameters			
		Temperature (T)	[°C]
		pH, field	[n.a.]
		pH,lab	[n.a.]
		Electric conductivity,field (EC_{field})	[μS/cm]
		Electric conductivity,lab (EC_{lab})	[μS/cm]
		Total dissolved solids (TDS)	[ppm]
		Redoxpotential (ORP)	[mV]
		Flow rate (Q)	[l/s]
Major ions			
	Anions	SO_4^{2-} , HCO_3^-,CO_3^{2-}, F^-, Cl^-, NO_3^-	[ppm]
	Cations	Ca^{2+}, Na^+, K^+, Mg^{2+}	[ppm]
Stable Water Isotopes			
		$\delta^{18}O$	[‰]
		δD	[‰]

4.3.1 Standard Parameters

Standard parameters (temperature, pH, EC, TDS) for each sample were measured directly on site using an electronic field probe (EXTECH, multi parameter PCSTestr 35). The pH and EC sensors were 3-point calibrated. The pH calibration was conducted with standard calibration solutions defined by pH 4.01, 7.00 and 10.00. To calibrate the EC-sensor, solutions with a electric conductivity of 84 µS/cm, 147 µS/cm and 1413 µS/cm were used. The Redox potentials (ORP) were measured with a KBM-100 (Volcraft) probe. The total alkalinity (=carbonate alkalinity) was determined with acid titration (HACH, AL-AP).[12] Flow rates (Q) were measured using a bucket-and-stopwatch approach.

[12]The total carbonate concentration was only measured between between end of November until end of March.

4.3.2 Major Ions

Major ions[13] were analyzed by ion chromatography (IC) using a DX-120 ion chromatograph system from Dionex (thermofisher) at the Institute of Geological Sciences ETH Zurich.[14] The accuracy of the DX-120 IC system depends mainly on the signal to noise ratio of the column, which changes over time and if possible contaminants are present. The accuracy of the IC at time of use was below ±5% (pers. communication Fanny Leuenberger), and increases with decreasing ion concentration.

For each sample, two 5 mL probes were prepared, one for the anions analysis and the other for the cation analysis. Before running the samples, the EC and pH of each sample was measured using the inoLab EC-pH measuring instrument from WTW. The instrument accuracy is for pH ± 0.005 units and ± 0.5 % of the measured EC value. EC values in probes which exceed the general working range of 0-500 μS/cm were diluted 10x using a diluter (Microlab500 from Hamilton), to ensure the concentrations were within the ranges of the standards and thus improve accuracy (table 10 and 11 in Appendix C).

Note that the HCO_3^- concentrations were calculated according to Basu (2008). The calculation is based on the total alkalinity (all carbonate ions) concentration and pH measured in the field. The charge balance error (CBE) was calculated according to Freeze & Cherry (1979).

4.3.3 Stable Water Isotopes

The concentrations of water isotopes were determined using a Picarro L2130-i analyzer which is based on a Cavity Ringdown Spectrometer (CRDS) technique.[15] The analysis has been performed at the Institute of Geological Sciences of ETH Zurich. The precision of δ18O and δD measurements of the Picarro L2130-i analyzer is $< 0.025‰$ /sample and $< 0.1‰$ /sample, respectively. The 24-hour drift is $< 0.2‰$ /sample for δ18O and $< 0.8‰$ /sample for δD (Picarro, 2012).

As analysis preparation, the collected samples were filtered with 0.45 μm (millipore) filters. All samples taken from the ditch and the boreholes were additionally treated with activated carbon to remove any potential traces of oils. The probes were stored in glass vials (2 mL) at 4°C to reduce potential evaporation losses. Working standards[16] were repeatedly inserted into the probe sequence after every 5-6 samples. To avoid a memory effect (contamination of previously measured water),

[13] Mg^{2+}, Ca^{2+}, K^+, Na^+, NH_4^+, Li^+, Sr^{2+}, So_4^{2-}, Cl^-,F^-, No_3^-, No_2^-, PO_4^{3-}, Br^-

[14] Instrument Operation: To measure ion concentrations, the IC pump injects 25 μL sampling water into the charged exchange column, where the ionized species are held back (anion column: IonPac AS14/ cation comlumn: IonPacAS15). An eluant of higher affinity is then injected to exchange the ions in the column, whereas based on the retention times of the ions within the column the type and concentration of a specific ion can be estimated. As eluants a carbonate (0.286 g/L)/ hydrogencarbonate (0.253 g/L) puffer and a methanesulfonic acid (20 mM) solution were used for anions and cations, respectively.

[15] Instrument Operation: The sampling water get first sampled by a high-precision autosampler (Picarro, A0325). The autosampler then injects the fluid in the vaporizer module (Picarro, A0211). The water vapor is then inserted in the CRDS unit, where gas-phase water molecules are identified based on their unique near-infrared absorption spectrum. The instrument estimates the concentrations by measuring the decay time of an emitted laser beam, which depends on the sample characteristic wavelength adsorption (www.picarro.com/company/technology/crds, accessed in January 2021).

[16] Here, standardized Sibirian Water, Mediterranean Sea Water and Zurich Water was used.

the Picarro Autosampler was programmed to exclude the first three to four (out of seven to nine) injections from final results for each sample.

Raw measurements were post-processed directly by the Picarro software ChemCorrect, which calculates the isotopic composition as δ-value (Picarro, 2012). The δ-value was calculated by the software relative to the Vienna Standard Mean Ocean Water (VSMOW) according to the equation 1.

$$\delta^{18}O \text{ or } \delta^{2}H = \frac{R_{SAMPLE} - R_{VSMOV}}{R_{VSMOV}} * 1000 \tag{1}$$

R_{SAMPLE} and R_{VSMOV} equal to the ratio of heavier to lighter isotopes in the sample or the VSMOV water, respectively (equation 2).

$$R_{SAMPLE} = \frac{^{2}H_{SAMPLE}}{^{1}H_{SAMPLE}} \quad \text{or} \quad R_{SAMPLE} = \frac{^{18}O_{SAMPLE}}{^{16}O_{SAMPLE}} \tag{2}$$

The deuterium excess (d) has been calculated with the equation 3.

$$d = \delta D - 8 * \delta^{18}O \tag{3}$$

4.4 Data Management

The open source data management system OpenBIS was used to store and manage the field and analytical data collected as part of this thesis.[17] OpenBIS can store raw and processed data, but also methodologies, field or lab notes, as well as links to further data storage locations. The data can be directly inserted via web interface or via manually/ automatically per 'dropbox' mechanism. Custom-built pipelines can be developed to automate the processing of hydrochemical data and facilitate comparisons with further measurements taken at same tunnel locations (e.g. microbiological data sampled at the same locations by the Geobiology Group 2020/2021, ETHZ).

4.5 Data Analysis

4.5.1 Data Pre-Treatment

Due to non-uniformity and incompleteness of hydrochemical data sets, a pre-treatment of the data set was essential before executing the hydrochemical analysis. Especially for the multivariate statistical analysis a prior pre-treatment of the data set is crucial (Güler et al. (2002); Templ et al. (2008)). However, also for hydrochemical standard tools (used in the exploratory analysis, section 4.5.2) it is important to have a certain data set pre-treatments.

Figure 11 shows the workflow for the performed data preparation from the raw data base towards a validated hydrochemical data set as input for the Cluster Analysis. Individual preparations steps

[17] https://openbis.ch/, accessed January 2021

also executed for the traditional hydrochemistry tools (as introduced in section 4.5.2) are marked with asterisks.

The first step (step 1) was to edit the data matrix, which includes the removal of parameters with redundant characteristics, highly temporal variability or parameters/ samples with many missing data. The following parameters had been excluded for the cluster analysis: EC (lab), pH(lab), ORP, Lithium (conc.), Magnesium (conc.) and Nitrate (conc.). The first two parameters were excluded due to potential changes occurring during the period of storing the samples until measured in the laboratory, such as degassing/ precipitation processes. The ORP was excluded due to unreliable and highly variable results when conducting repeated measurements (see section 6.3). The above mentioned ions were removed since the measurements showed a high temporal variability, which was understood to reflect a measurement artefact (all mentioned ions show in general low concentrations close to the detection limit, what adds an uncertainty to the measurement as mentioned in section 4.3.2). Apart from the above, step 1 also includes the removal of negative values. Variables containing negative values were added to a constant or multiplied by -1, if all measurements were expressed negatively (e.g. stable isotope). A data set only consisting of positive values is acquired for power transformations (see step 4).

Step 2 covers the statistical imputation of missing values. Some missing values could be estimated using relationships within the data set. If no relationship to another variable is known, the missing values were imputed with the mean of the samples taken at a specific site. Missing values caused by a measurement below the detection limit were replaced by the detection limit.

Step 3 targets the major ions in the data. The measured ionic composition within a sample must be close to electrically neutral. The charge offset between cations and anions was estimated by the charge balance error (CBE) (provided that all major species have been measured). In the context of this thesis, a CBE below 25% is assumed to be acceptable. Samples with a CBE $> 25\%$ were excluded from the data set.[18]

Step 4 is targeting the transformation and standardization of the data. Transformation is important, since the planned multivariate statistical approaches are based on the assumption, that the data is gaussian-like distributed. The distribution of each variable can be estimated by univariate statistics, e.g. by visualizing the data with histograms (figure 27 and figure 28 in the Appendix D). The normality of the data can additionally be check by using variable statistical tests (here the Shapiro-Wilk Test, the D'Agostino's K-squared Test and the Anderson-Darling Test were applied). In this case, a minority of the tests suggested a Gaussian distribution ('soft failure'), what implies a gaussian-like data distribution of the parameters. To increase this trend, a log-transformation was applied to the non-compositional parameters. The compositional data (major ions [ppm]/ stable isotopes [ppt]) had to be log ratio transformed, since the analytical value is expressed relative to remainder (Filzmoser et al., 2009). Here, an isometric log-ratio (ilr) transformation was chosen because this transformation appears to work well in hydrochemical data sets (Templ et al., 2008)

[18] Charge balance error in this order are for hydrochemical studies rather high (Fritz, 1994). The reason for the elevated CBE value is probably due to the low mineralization level (= low ionic strength) of the BULGG groundwater, as discussed in section 6.3.

and, unlike other log-ratio transformations, the ilr-transformed data can be applied to Euclidean space (Filzmoser et al., 2009).

Standardization (centering and scaling of the data) was then applied, since variables differing in several magnitudes from each other and (real!) outliers are included into the data set. The standardization was achieved by using the RobustScaler function by sklearn, which substracts the median (centering) and scales the data using the interquartile range (scaling). This scaler is more consistent when having non-normal distributed variables, since the center estimate is not affected by deviant data points.

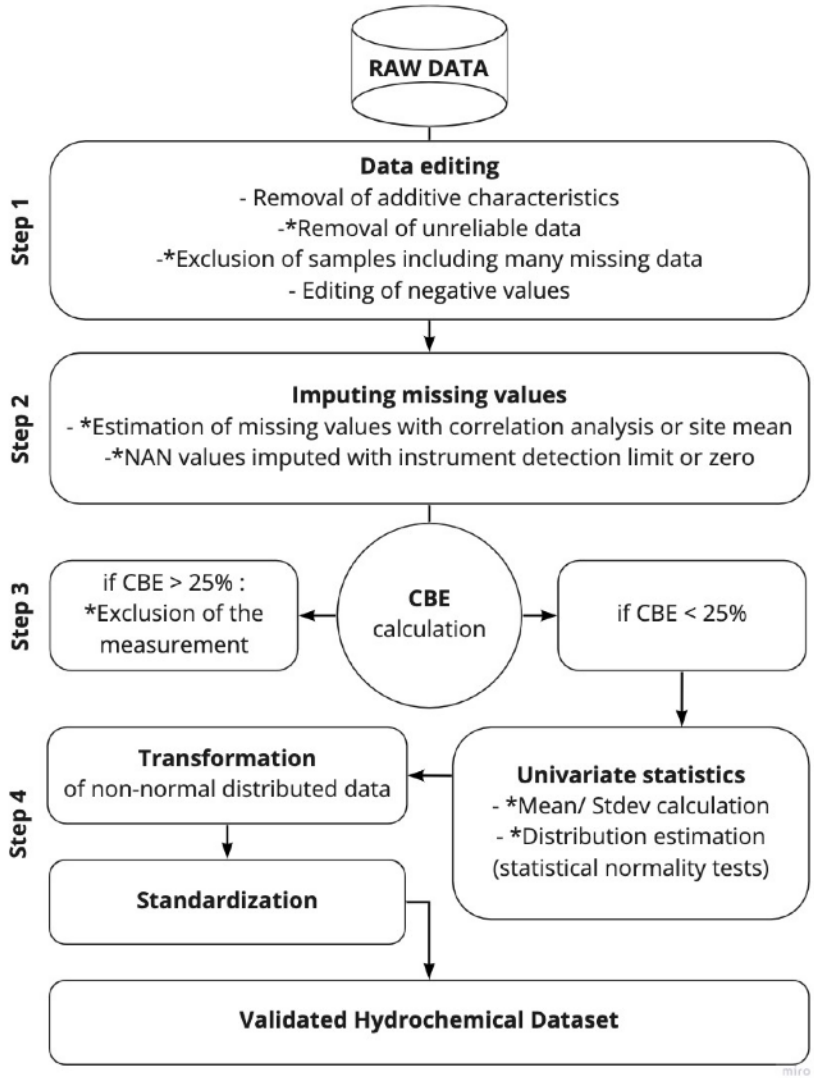

Figure 11: Steps of the data preparation to achieve a validated data set to conduct PCA and clustering approaches. *Steps which were as well done for hydrochemical standard tools.

4.5.2 Exploratory Data Analysis

Hydrochemical data sets tend to be high-dimensional, including a whole suite of physico-chemical parameters. Such data sets are generally 'unlabeled' from a hydrological standpoint, meaning that no a priori knowledge exists on the patterns in the data set. To be able to detect and visualize such underlying temporal or spatial patterns, the following exploratory data analysis tools have been used: Scatter plots, Stack plot, Piper diagram, Stiff diagrams, δ^{18}O-δD diagram.[19]

Standard hydrochemical analysis can provide valuable insights in hydrochemcial patterns, however, the main problem connected to such tools is the difficulty of spatial associations and integrate/ connect all outcomes to specific water types and their spatial boundary. The interpretation of which water belongs to which water type (and thus influenced by which water source and pathway) is thus largely based on subjective judgement, what increases the uncertainty of the outcome. In recent hydrochemical and geological studies, multivariate statistical analysis (MVSA) were used to overcome this limitation.

4.5.3 Multivariate Statistical Analysis

Multivariate statistical analyses are ideally suited to extract underlying basic features, classify and categorize unlabelled data in complex multi-parameter data sets. The widely used technique in hydrochemistry as classify scheme or simple water quality assessments is the cluster analysis (CA) (Davis & Sampson (1986); Templ et al. (2008); Güler et al. (2002)). A very popular method is the k-means clustering approach, (Usman et al. (2014); Singh et al. (2017)). However, the most common method nowadays is the hierarchical cluster analysis (HCA), which has been used for example to investigate arsenic mobilization (Jiang et al., 2015) or trace the infiltration of artificial waters (Moeck et al., 2016), as well as mountain-block recharge and groundwater circulation patterns in the Western Andes, in Central Chile (Taucare et al., 2020).

In this study, both mentioned clustering algorithms (HCA, k-means) were applied to be able to find different clusters (water types) in the data set. To improve the application of cluster analysis in hydrochemistry, it is recommended to do a prior reduction of the matrix dimensionality by a dimension reduction technique, as for example the Principal Component Analysis (PCA) (Marín Celestino et al., 2018).

4.5.3.1 Principal Component Analysis (PCA)

To improve the cluster analysis (CA), a Principal Component Analysis (PCA) was executed on the pre-treated (scaled) data set. PCA attempts to reduce the dimensionality of a data set with lowest possible loss of information stored within the data using interrelations between the variables.

To assess if the data set is suitable to perform a PCA, the Kaiser-Meyer-Olkin and Bartlett's tests were conducted (the outcome can be found in table 12, Appendix F). Both tests indicated that the data set was appropriate to conduct PCA. Herein, PCA was performed with the SVD based PCA-algorithm from the Scikit-Learn library. To obtain a dimension reduced data set, the

[19] All hydrochemical tools were compiled in python.

PC algorithm searches for the best linear fit through all the original data points by maximizing the sum of the squared distance between the projected points and the newly defined origin. The first linear fit through the data points represents the first principal component (PC1) and is the linear combination of the original variables (high dimension) to newly defined principal components (low dimension) having the orientation of the largest spread in the original data set. PC2 is the next best fitting line through the data points (and new origin), which is perpendicular to PC1. The same accounts for PC3, which has to be perpendicular to PC1 and PC2, etc.. The limiting number of PC's calculated by the alogrithm is given by the number of observations or variables, depends on which is smaller. The PC (Z) can be summarized in the following equation 4 (Singh et al., 2017):

$$Z_{ij} = a_{i1}x_{1j} + a_{i1}x_{1j} + ... + a_{im}x_{mj} \tag{4}$$

where a is the component loading, x the variable value, m the variable number, i the corresponding PC, j the sample number.

The number of principle components to extract was estimated with the scree plot (figure 29, Appendix F) and the Kaiser Criterion (Cloutier et al., 2008). The scree plot shows how the variance decreases with increasing number of PC's. The most pronounced change in this relationship represents the best balance between minimizing the PC number and maximizing the variance explained by the PC's. Here, the scree plot suggests 5 principle components to keep. The Kaiser test requests the calculation of the eigenvalues of each principal component (PC), whereas an eigenvalue >1 indicates that a PC explains more than one variable (and is therefore desired). Table 3 shows the eigenvalues (EV) of the first seven principle components, which indicates that at least the PC5 - PC7 should be excluded. Taking into account both approaches, the first four principle components were determined to represent a sufficient proportion of the total variance estimation. The first 4 PC's explain 92.3% of the cumulative variance (table 3) of the original data set variance.

Table 3: The explained variance ratio (EVR), the cumulative explained variance ratio (CEVR) and the eigenvalues (EV) of the first seven components (rounded on two right-of-comma positions). PC = Principle component.

PC	1	2	3	4	5	6	7
EVR	41.4%	23.6%	17.8%	9.5%	3.1%	2.7%	0.6%
CEVR	41.4%	65.0%	82.8%	92.3%	95.4%	98.1%	98.7%
EV	4.5	2.5	1.9	1.0	0.33	0.29	0.07

4.5.3.2 Cluster Analysis (CA)

The cluster analysis was performed with two clustering algorithms, namely the k-means and hierarchical clustering. The clustering analysis was applied to the PCA data set, where the average

values for each sampling site was taken. The cluster analysis approaches were executed with the module *AgglomerativeClustering* (Scikit-learn library) and *hierarchy* from the Scipy library.

The k-means technique (MacQueen et al., 1967) attempts to find a pre-defined amount of clusters (k) within the pre-treated and reduced input data set. To do so, the k-means algorithm starts by initializing cluster center (here the kmeans++ initialisation was chosen (Arthur & Vassilvitskii, 2006)). The algorithm proceeds by i) finding the closest cluster center by computing the squared distance (in Euclidean space) to each input data point and ii) the cluster center is shifted to the mean of all data points assigned to the same cluster. These two steps are iterated until convergence is reached. To determine the number of clusters for k-means clustering, a scree plot was constructed (figure 30, Appendix F). The scree plot shows the number of clusters (k) versus the inertia (sum of the squared distances to the closest cluster center), also called the mean-squared-error (MSE). The MSE cost function (J_{MSE}) is formulated as follows (Žalik, 2008):

$$J_{MSE} = \sum_{i=1}^{k} \sum_{x_t \in C_i} ||x_t - c_i||^2 \tag{5}$$

where, C_i and c_i is the cluster and its centroid, respectively. x_t is a data point, which is an element of cluster C_i.

With each k, the inertia decreases, whereas the most pronounced change in the cost function proposes the number of clusters k. In figure 30, one can see that this approach here in proposed 3 clusters. However, the change is not very distinct, where each cluster number does not increase the performance of the algorithm considerably. To validate the number of cluster, the cluster analysis was repeated with clusters from $k = 2$ to $k = 7$. Based on this sensitivity analysis, $k = 3$ was providing the most relevant outcome where the data can be reasonably explained.[20]

The hierarchical agglomerative clustering technique (Davis & Sampson, 1986) uses a bottom-to-top approach to cluster data points. The algorithm first assigns a separate cluster to each data point. The distance between each cluster pair is then calculated (here in euclidean space), where the closest pair is linked together. The linkage distance indicates the dissimilarities between cluster pairs and is shown on the y-axis of a HC-Dendrogram. This step is then repeated until all initial clusters are linked together, in the order of an increasing cluster dissimilarity. To compute the proximity of two clusters, the 'ward'-algorithm was chosen.

The selection of the metric space and the cluster distance measure method is of high importance in the Hierarchical Clustering Analysis. Therefore, a sensitivity analysis was performed, by varying the these parameters for each run to optimize the HC-clustering performance. The best outcome for all cluster analysis approaches was achieved with Euclidean distance coupled with the 'ward' method. Similar performance were obtained using the 'braycurtis' or the 'cosine' distances combined with the 'weighted' method, however the proportion of sampling sites assigned to miss-matching

[20]Such an approach implies a prior knowledge of the system and is a standard scientific procedure (hypothetico-deductive method).

clusters (judgment based on field observations) was higher compared to the outcome achieved with the Euclidean distance/ward method.

4.5.4 Mixing Analysis

To be able to detect leading hydrochemical characteristics and processes of the obtained clusters, an end-member analysis was executed using the mixing model 'MIX code' (Carrera et al., 2004). Apart from identifying hydrochemcial end-members (EM) and their hydrochemical characteristics, MIX was further used to estimate spatial contribution patterns of the EM's towards each obtained cluster.

MIX has been applied in various hydrogeological and hydrochemcial studies. In groundwater studies, the method has mainly been used to detect mixing ratios of multiple sources (end-members) towards a sampling point (fluid-fluid interaction), based on conservative tracer concentrations (Vázquez-Suñé et al. (2010); Scheiber et al. (2020); Behrouj-Peely et al. (2020)). However, MIX can also be used to detect potential geochemical reactions along flow paths (water-rock interactions) for the parameters behaving non-conservatively (Tubau et al. (2014); Jurado et al. (2015)). The model is, unlike to other traditional mixing models, able to compute contribution ratios with unknown end-members by adding an uncertainty to the end-members concentration. This serves mainly the problem of not being able to sample the 'true' end-member (but only mixture of it). Simple mixing models are based on linear mixing (see equation 9 Appendix O) or least squares computations to estimate mixing ratios in a specific sample (Behrouj-Peely et al., 2020) (for a more detailed description of mixing concepts, see Appendix O).

Carrera et al. (2004) introduces in MIX an algorithm computing the mixing ratio adding a maximum likelihood approach. The likelihood function (L_p), for which a maximum is searched, is formulated as follows (equation 6):

$$L_p = exp\left[-\frac{1}{2}(y_p - F\delta_p)^t A_p^{-1}(y_p - F\delta_p)\right] \tag{6}$$

where y_p is a vector including all species measured in sample p, F is a matrix of all chemical analyses of end-members, δ_p is the vector of mixing ratios and A_p is their covariance matrix.

The MIX model input is based on i) the number of the end-members at the site, each including the concentration + standard deviation of reference samples, ii) the parameters measured and iii) the collected sample concentrations + standard deviations.

The mixing analysis was executed with the site average concentrations, including eight parameters: fluoride, chloride, sulfate, sodium, calcium and the total carbonate concentration, as well as the $\delta^{18}O$ and δD values.[21] The number of end-members was estimated according to the three present water types (CA clusters) at the site (see section 4.5.3.2). The input end-member concentrations were chosen by one reference sample of each CA cluster (the values of the reference samples can be

[21] The selection of parameters was based on the observation that they i) contribute to the ionic and isotopic variability along the Bedretto tunnel and ii) are only marginally influenced by measurement uncertainties.

found in table 5). The assigned standard deviations to the end-member concentrations were set to 100% (to reflect the high uncertainty with respect to the concentrations added to the end-members). The total number of included samples is 30, each representing a natural tunnel inflow sampling site along the tunnel.[22] The concentrations and errors (uncertainties) inserted in the model correspond to the arithmetic mean and standard deviation of each sampling site, respectively.

[22] All sites including missing data were excluded.

5 Results

5.1 Spatial Hydrochemcial Trends

5.1.1 Standard Parameters

The average value and the mean standard deviation (σ_{mean}) of the standard water quality parameters can be found in figure 12 showing the spatial evolution along the Bedretto tunnel. Figure 31 (Appendix G) shows the measurements variability displayed with box-plots at each site.

The mean fluid temperatures of discrete tunnel inflows vary from 5°C to 19.5°C. The standard deviations are within 1.4°C. Temperatures generally increases with distance from the Ronco portal, and mimics the overburden depth. Negative temperature anomalies of several degrees (exceed the standard deviation significantly) are observed at TM 1300, TM 2850 and at TM∼4300.[23] When comparing these locations with the cumulative discharge records per 100 m obtained from a previous study, it is apparent that negative temperature anomalies correspond to zones of high inflows.

The electrical conductivity of fracture fluids in the tunnel ranges from 43.2 to 931.1 μS/cm. The EC standard deviations are varying between 2 and 68 μS/cm (σ_{mean} = 16.6 μS/cm). The sampling locations in the northwestern tunnel section (TM 3750 - TM 5132) showed very consistent EC measurements, which is expressed as generally low standard deviations (not exceeding 11 μS/cm). The spatial EC evolution shows i) a general increase around the Bedretto Lab (TM 2000) followed by a decrease between the laboratory and the Furka Basetunnel, ii) a strong variability in the gneiss part (especially within the Prato-series) and iii) negative anomalies, similar as observed in the temperature trend. The EC evolution in the Rotondo granite mimic the total spacing of fractures, where zones of low fracture spacing correspond to lower EC values.[24] Local negative anomalies again correspond to zones of high inflow (EC depressions at highly conductive inflow zones are not necessary visible in the fracture spacing evolution).

It is interesting to mention that the water quality trends in high inflow zones are characterized by a transition zone, where the water quality changes towards the zone center. Such spatial trends can be traced between about 50 to 150 meters. However, in smaller scales (cm - m scale), this trend can be highly disturbed and more complex. Field observations have shown that within a fault zone the temperatures and the electric conductivity have several local minimum values and can be different when sampling at the same tunnel meter, but on slightly different spots.

The pH (measured in the field) of fluids discharging from discrete fractures across the tunnel averages around 9, whereas 50% of the measurements lie within a pH of 8.7 and 9.2. The pH variations at one site are rather high. The largest standard deviation (>1 pH unit) can be observed at TM 1993. No clear spatial evolution (which would exceed the temporal variability) could be observed along the Bedretto tunnel.

[23] The overburden-temperture relationship does not show any significant correlation, mainly due to such zones of temperature depressions. The relationship can be seen in figure 35 in the Appendix H

[24] Only one site at TM 1798 does not match into this general trend. The fracture spacing in this tunnel section is with almost 40 meters very high, but the EC rather low (∼130 μS/cm).

The Redox potential (ORP) measurements for fracture discharge are all positive and range between +106.7 and +238 mV (σ_{mean} = 33.3mV). There is no general spatial trend visible along the Bedretto tunnel concerning the redox potential of the fluids.

The measured discharge rate from the sampled features show large spatial distribution and generally range from a few milliliters (mL) to several deciliters (dL) per second. The highest inflow is observed at TM 2848 sampling site A (~2.5 L/s).

The standard parameters measured in fully open boreholes are differing from the fracture fluids mainly in its ORP, pH and not surprisingly in the discharge rate.[25] The mean temperature of fully open boreholes are ranging between 16.76°C and 20°C, what falls into the expected range of the borehole surrounding rock temperatures. The pH values are consistently higher than pH measured in fracture inflows and is in between 9 and 10 pH units. The pH measured in boreholes is variable over time in a comparable manner to the variability accounted for fracture inflows. The electric conductivity is ranging from ~200 μS/cm to 400 μS/cm and shows a spatial difference throughout the BULGG laboratory. The EC is in general higher in the southern part of the BULGG laboratory. This trend is nicely visible by the evolution of EC related major ions (section 5.1.2, figure 15). The average ORP values in the deep boreholes are ranging between -4.86 mV to 144.66 mV and are thus significantly lower compared to the highly positive redox potential measured in fracture inflows. The discharge rate is in between 0.1 and 0.2 L/s (excluding measurements taken during stimulation works). An exception of the boreholes regarding the water quality measurements is the horizontally drilled welltec borehole. This borehole shows an average temperature of 15.9°C. The mean EC value is as well lower than measured in deep boreholes and is 112.8 μS/cm. The discharge rate is with 0.02 L/s considerably lower than observed in the deep boreholes and comparable with the discharge rate of some fracture inflows. The pH and the ORP measurements are comparable to the other boreholes implemented in the BULGG laboratory (pH >10, average ORP = 79.87 mV).

[25] The discharge rate measured in fully open boreholes do represent the cumulative discharges from intersected structural features

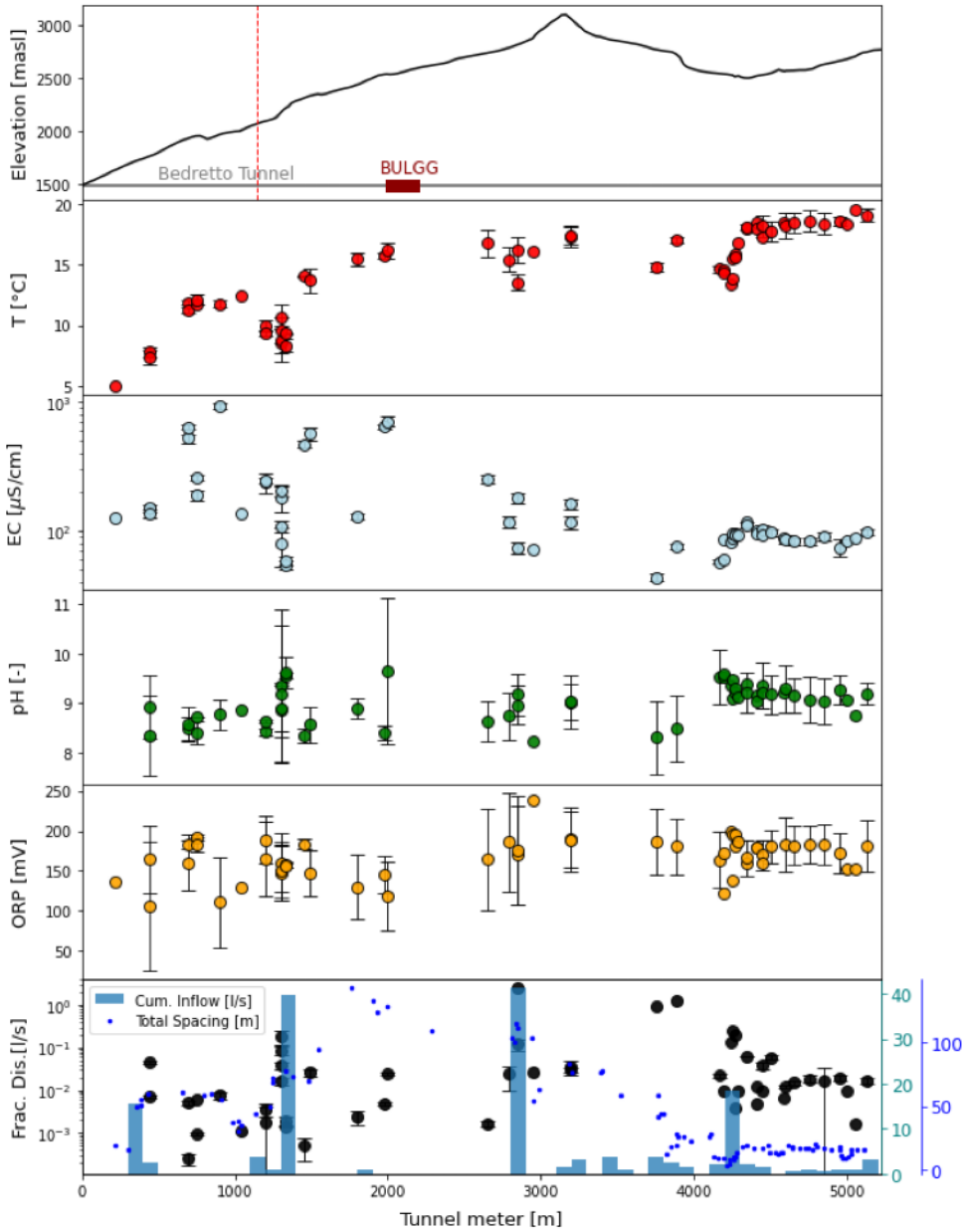

Figure 12: Spatial evolution of the annual mean (+ standard deviation) water quality standard parameter measurements. The measurements include the temperature, the electric conductivity (EC, log scale), the pH, the Redoxpotential (ORP) and the discharge rates of discrete fractures (log scale). Latter is shown versus the cumulative discharge rate per 100 meters compiled by Masset & Loew (2010) and the total fracture spacing summarized in V. H. Lützenkirchen (2002). The red dotted line corresponds to the geological boundary between the Rotondo granite (right, SE) and the prevariscian gneisses (left, NW).

5.1.2 Major Ions

The average value and its standard deviation (σ_{mean}) of the major ions composition can be found in figures 14 showing the spatial evolution along the Bedretto tunnel. Figure 32 and 33 (Appendix G) show the temporal variability of the ions per sampling site with box-plots.

The main ions include sulfate, calcium, sodium, carbonates, fluoride and chloride. Magnesium, potassium, lithium and nitrate tend to have concentrations below 1 ppm for most of the sites. The sulfate, calcium, chloride and sodium concentration of the entire study site correlate significantly with each other (see figure 38, Appendix I). The correlation between sulfate and calcium is very strong (correlation coefficient r-squared of 1). Chloride correlates the strongest with sulfate (r-squared = 0.9). Sodium correlates with sulfate, calcium and chloride with a correlation coefficient of 0.8. sulfate and calcium furthermore significantly correlated with the TDS and EC both with an r-squared-value of 1. EC correlates further significantly with chloride (r-squared-value of 0.9) and sodium (r-squared-value of 0.8). Apart from these relationships, no significant linear correlation has been observed.

Anions are dominated by sulfate, whose concentration varies from 4 to 520 ppm, the standard variations are within 0.3 and 19 ppm. The lowest sulfate concentrations were measured between TM 4166 and TM 4192. The highest sulfate annual mean concentration is linked to the sampling site at TM 901.

The total alkalinity (including all carbonate species) ranges within 8 and 27 mg/L (figure 13).[26] The highest (total) carbonate concentrations (> 25 mg/L) are linked to two sites in the Tremola-series, namely TM 440 / TM 444. In the Rotondo granite, sampling sites characterised by a high mineral content are generally showing a reduced total alkalinity (low carbonate concentrations mainly in the southeastern tunnel part, usually < 10 mg/L). Fluids sampled in the northwestern tunnel section (TM 2647 - TM 5132) show concentrations between ~10 - 20 mg/L (average of 15.6 mg/L). The mean standard deviation is 2.5 ppm.

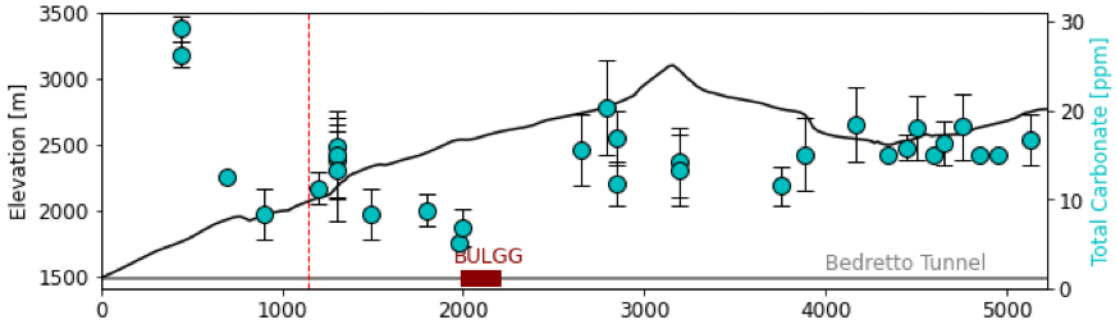

Figure 13: Spatial evolution of the alkalinity (total carbonate concentration) along the Bedretto tunnel (based on acid-titration measurement). The red dotted line corresponds to the geological boundary between the Rotondo granite (right, SE) and the prevariscian gneisses (left, NW).

[26] Note that the carbonate content is based on the pH mainly stable as bicarbonate. The closer the pH is to 10, the higher the HCO_3^-:CO_3^{2-} ratio.

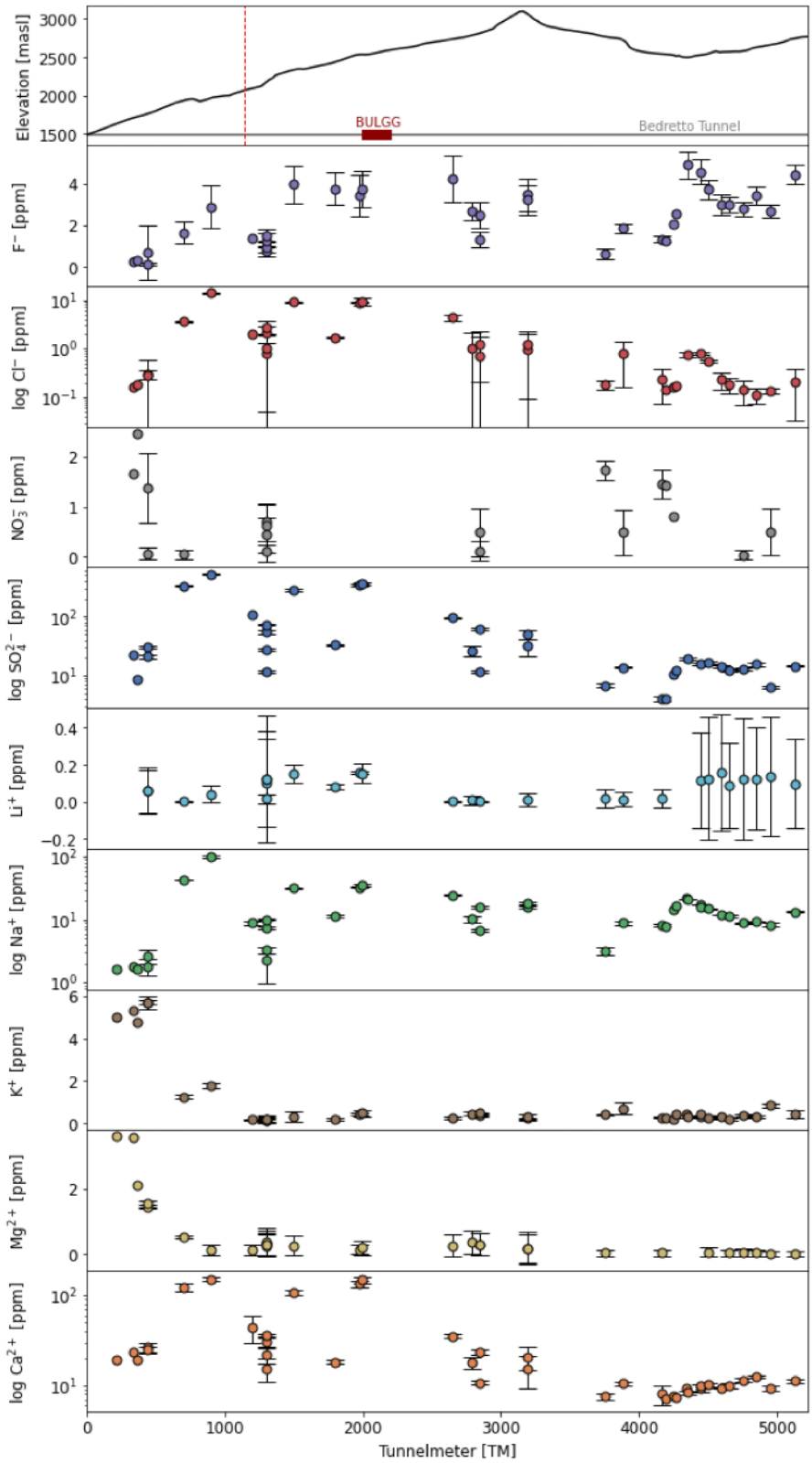

Figure 14: Spatial evolution of the annual mean (+ std) dissolved ions (IC measurements) along the Bedretto tunnel (each data point corresponds to a sampling site). The red dotted line corresponds to the geological boundary between the Rotondo granite (right, SE) and the prevariscian gneisses (left, NW). The color code is consistent with figure 15.

Fracture waters between TM 2794 - TM 5132 and TM 0 - TM 444 are low in chloride (< 1.2 ppm). Elsewhere slightly increased chloride concentrations can be observed. The highest chloride concentration was observed at TM 901 (13.86 ppm). The mean standard deviations range between 0.02 and 1.6 ppm.

The fluoride concentration seems to follow the trend of the measured temperatures. However, no significant correlation could be obtained when comparing the fluoride concentration, mainly due to the clear deviation from the expected evolution in the northwestern tunnel section. Several waters have fluoride concentrations above 1.5 mg/L (i.e., above the World Health Organization (WHO) standard for drinking water quality). The σ_{mean} of fluoride varies between 0.04 and 1.3 ppm.

Increased nitrate concentrations (> 0.5 ppm) can be found at sampling locations close to the Ronco portal, at the major conductive zones at TM 1300, TM 2848, between TM 4100 - 4300, as well as at TM 3750 and TM 3884.

Calcium and sodium constitute the two main cations in most waters, with annual mean concentrations ranging from 7 to 150 ppm and 1.6 to 99 ppm, respectively. The sodium concentration shows generally very low standard deviations (between 0.1 - 5.9 ppm), whereas the standard deviation for the calcium concentrations are up to 14.5 ppm. Generally calcium concentrations exceed sodium concentrations, except in between TM 4166 - TM 5130, where fluids have a relatively high concentration of sodium (Ca^{2+}/Na^{+} ratio < 1). Very high sodium concentrations were furthermore measured in the Prato-series (up to 100 mg/L).

Magnesium and potassium concentrations are low (below 1 ppm), except in the gneiss part of the Bedretto tunnel, where the concentrations for magnesium and potasssium are gradually increasing. Mostly in the tunnel section intersecting the Tremola-series, the magnesium and potassium concentrations are rather high (up to 4 mg/L and 5 mg/L, respectively). The temporal variations of the magnesium concentration in the Rotondo granite is the highest at TM 1300 and TM 2600 - TM 3200 (however, the σ_{mean} is < 1 mg/L). The potassium concentrations in the Rotondo granite are constant through time (σ_{mean} < 0.33 ppm).

The average annual lithium concentration is everywhere < 0.2 ppm and show high standard deviations, especially for the northwestern tunnel section and at TM 1300. For many sites no lithium could be detected.

The ionic composition of the sampled fully open BULGG boreholes with their laboratory position are shown in figure 15 (excluding measurements from discrete intervals). Figure 15 includes three subfigures, subdivided by the proportion of ion concentration (major, intermediate and minor concentrations) of each individual borehole.

The proportion of the ionic composition is similar to what we can be observe in the seeping fractures within the Rotondo granite on tunnel elevation. However, it is interesting to note that the correlation between sulfate and calcium concentration with the EC for borehole fluids is lower than observed for fracture fluids (r^2 is 0.89 and 0.88, respectively). The r^2 of EC versus sodium and chloride decreased below 0.6. The cations in borehole fluids are also predominately defined by the

calcium and sodium concentration. The calcium concentration varies between 10.5 - 66.7 ppm. The sodium concentration is in between 15.1 - 27.3 ppm. The potassium and magnesium concentration is in all boreholes below 2 ppm. The anions are dominated by sulfate (between 19.8 and 185.3 ppm). The mean fluoride concentration is in between 3.9 - 6.6 ppm ($\sigma_{mean}\pm$ 0.32 to $\pm$ 1.34). The mean chloride concentration is between 1.7 and 5 ppm. The nitrate and lithium concentration is for all boreholes very low ($<$ 0.5 ppm).

The BULGG boreholes implemented in the NW side of the laboratory (CB3, CB1, ST2) are showing in general lower concentrations in its dissolved major ions compared with boreholes of similar depths on the SE side of the laboratory (e.g. ST1 versus ST2, CB1/ CB3 versus CB4).[27] The trend is mainly visible in the major ions of highest concentration (top subfigure), namely the sulfate, calcium and sodium concentration. Chloride and fluoride (intermediate concentrations, subfigure in the middle), as well as the minor dissolved constituents (Mg^{2+}, K^+, Li^+ and NO_3^-) do not show this trend.

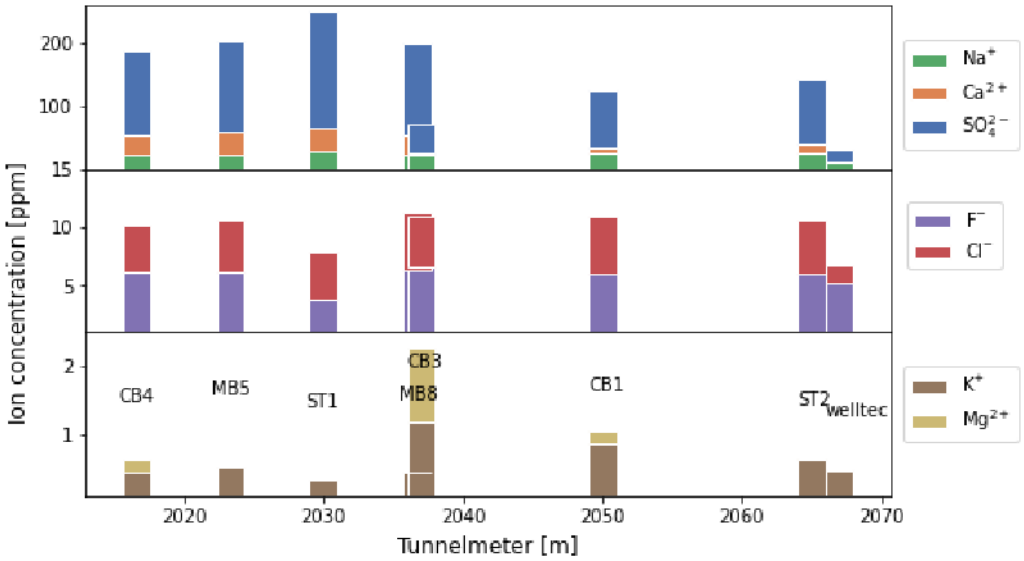

Figure 15: Dissolved ion composition of fully open BULGG boreholes. Top: Ions of high concentration; Intermediate: Ions of intermediate concentration; Bottom: Ions of low concentration. The color code is consistent with figure 14. Note that the displayed boreholes are of different depth. Of comparable depth are the monitoring boreholes (CB /MB) and the stimulation boreholes (ST) to each other. The welltec borehole is drilled horizontally at tunnel level.

[27]Note that MB5 and MB8 are drilled and sampled after the stimulation campaigns in Dec/Nov 2020 and May 2021. The other CB boreholes were mainly sampled before any hydraulic stimulation occurred. Due to this temporal shift in measurements, the comparison between MB5/MB8 to the other CB boreholes must be treated with caution. Furthermore, the welltec borehole is drilled horizontally at tunnel elevation and thus less influenced by deep alpine fluids and can not be compared to the other boreholes.

Repeated hydrochemical measurements in different depths could only be taken from CB2 (see section 4.2.1). The interval fluids of CB2 indicate a general increase in its mineralisation degree with depth (mid depths: interval 7 = 140.14 m below tunnel (m bt), interval 3 = 195 m bt). The mineralisation degree increase is mainly supported by the sulfate and calcium concentration, which increase by the factor of 5.

The piper diagram (figure 16) allows to identify the ion composition of the BULGG groundwater.[28] Fluids from natural seeping fractures depicted in the piper diagram clearly shows a chemical evolution from a Ca-Cl type (Ca-SO_4 waters) towards a mixed type (Na-Ca-HCO_3-SO_4 waters) with increasing distance from the Ronco portal.

The borehole fluids group very close to fracture fluids collected around the laboratory (TM 2000). Some samples deviate from the borehole cluster move towards a sodium-chloride water type (due to a deviation in the cation triangle towards a decreased calcium and increased Na(+K) proportion and a less distinct deviation in the anion triangle towards slightly lower sulfate and higher carbonate proportion). These samples correspond primary to samples from the ST2 and CB2 (interval 7) boreholes.

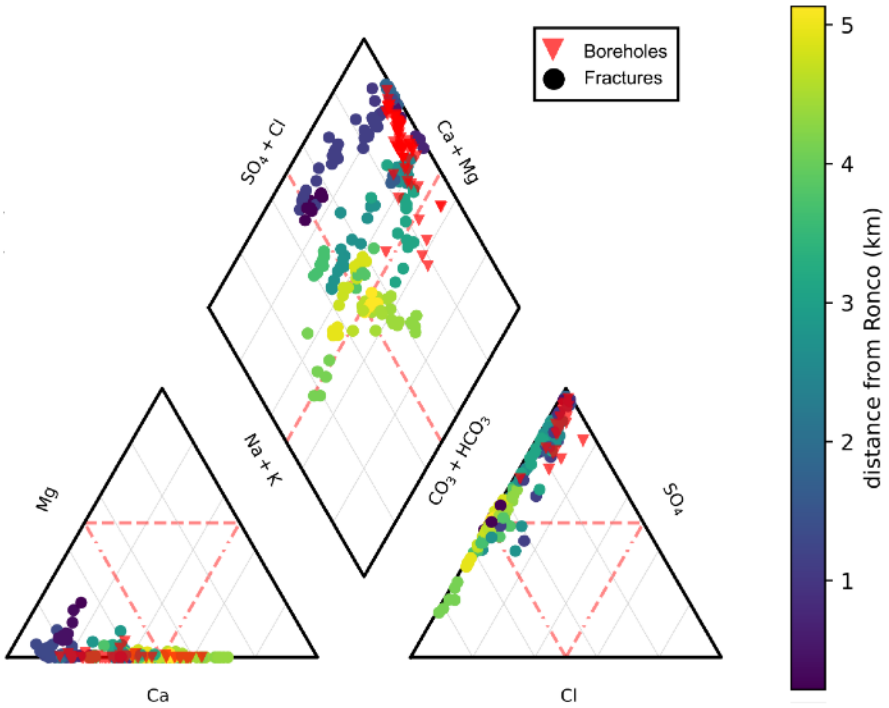

Figure 16: Piper diagram (Piper, 1944) showing the chemical composition of fracture and borehole fluids (derived from major ion concentrations in meq/L). The left triangle shows the relative proportion of the cations. The right triangle displays the relative proportion of the anions. The diamond shows the projection of the data points from both triangles and allows a ionic classification based on the cation and anion information.

[28]The classification scheme for determine the hydrochemical facies based on the piper diagram has been adapted from Back & Hanshaw (1965)

5.1.3 Stable Water Isotopes

The main outcome of the stable isotope analyses are shown in figure 17, 18 and figure 39 (Appendix J). The encountered isotopic variability expressed with box-plots can be found in figure 34 (Appendix G).

Figure 17a shows the topographic profile and the sampling sites in Bedretto tunnel including the number of samples analysed on its isotopic composition per sample.[29] The spatial evolution of the fracture water $\delta^{18}O$[30] and deuterium excess values along the Bedretto tunnel can be found in figure 17b and c, respectively. The general $\delta^{18}O$ trend shows a decrease with increasing tunnel depth. The decrease does not correlate with the overburden, but reveals a general decrease with increasing elevation (see figure 35, Appendix H). Small deviations can be observed at TM 901 (towards more depleted water), as well as below the Rotondo summit between TM 2752 - 3750. The average $\delta^{18}O$-value at BULGG is -14 ‰. The average standard deviation is at 0.077 ‰ and is in between 0.013 ‰ (min) and 0.4 ‰ (max).

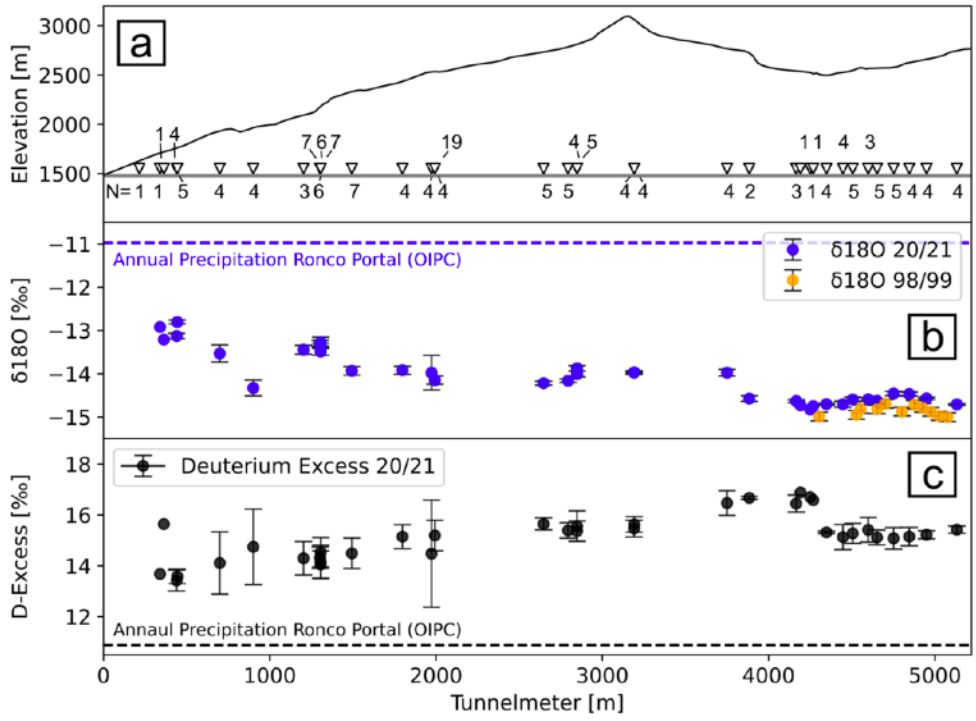

Figure 17: a) Profile of the Bedretto tunnel including the sampling site (triangles) and the corresponding number of samples taken during 2020/2021. b)The blue marker represents the measured $\delta^{18}O$ values of fracture fluids along the Bedretto tunnel in 2020/21. The black bars represent the standard deviation. In orange are the $\delta^{18}O$ values in the back part of the Bedretto tunnel, reported by U. Ofterdinger et al. (2004) and measured during the years 1998/99. The black bars are representing the analytical error. c) Deuterium excess evolution along the Bedretto tunnel including standard deviations (black bars).

[29] The number of samples (N) was included because fewer samples were included compared to the main ion analysis.
[30] Note that the $\delta^{18}O$ and δD correlate with r-value of 0.977

Between the two fault zones at TM 3750 and TM 3884 a significant drop in the δ^{18}O signature can be observed, while the overburden does not change considerably. In the northern most tunnel section (TM 3884 and 5132) the δ^{18}O value is significantly depleted (14.6 $\pm \sim$ 0.15 ‰). The data reported by U. S. Ofterdinger (2001) from 1998 to 1999 (figure 17b), compares relatively well with the trend observed in 2020/2021. The δ^{18}O values reported by U. Ofterdinger et al. (2004) are about 0.26 ‰ lower compared to the average δ^{18}O measured in 2020/2021 (including isotopic data form TM 4348 until TM 5132).

The Bedretto data plots with an average deuterium excess of 15.1 ‰ (σ_{mean}: $\pm$ 0.94 ‰)(figure 17c). It is apparent, that the deuterium excess is varying more strongly (higher standard deviation) in the southern part of the Bedretto tunnel (TM 0 - TM 2000). Further one can see that in the tunnel section between TM 0 and TM$\sim$4300 the deuterium excess anti correlates with the general depletion trend by the δ^{18}O value. In the very northern part of the tunnel (TM 4300 -TM 5132), the deuterium excess deviates from this trend and decreases slightly to an average d-excess of 15.5 ‰.

Figure 18a displays the δD-δ^{18}O diagram including all groundwater fluids, as well as the GMWL, the Ticino and OIPC LMWL.[31] Figure 18b is a zoom in of figure 18a (black rectangle), which displays the isotopic composition of fully open (TB) and discrete intervals (int.) of the BULGG boreholes, as well as the average isotopic composition of the ditch water at TM 2097. The color code of the borehole data in figure 18b is showing the wellhead position in the BULGG laboratory (in kilometers form the Ronco Portal).[32]

In figure 18a it is apparent, that the isotopic composition of the BULGG groundwater gets more depleted as going deeper into the Bedretto tunnel. According to the spatial variability in the isotopic composition, the isotopic data set can be subdivided into three groups. Group 1 (G1) is reflecting the enriched water sampled between TM 0 - TM 1500. Group 1 shows generally a gradual depletion towards the inner of the tunnel, however, not perfectly consistent. Group 2 (G2) is reflecting water inflows occurring from TM 1494 to 3750, also including the BULGG boreholes. Group 2 fluids do not show a clear spatial evolution along the Bedretto tunnel (less than what is observed in group 1), but exhibit a more diffuse pattern.

[31] A Meteoric Water Line (MWL) is a convenient way to display the isotopic composition is the δD-δ^{18}O relationship. This relationship on the global (annually) scale is defined as : $\delta D = 8 * \delta^{18}O + 10$ (Global meteroric water line, or short GMWL). For different reservoirs (localities) there are differences in the vapor sources, the rainout, the re-evaporation, the ice and snow accumulation and the melting, caused by different climates. These differences lead to different relationships between δD and δ^{18}O. The relationship for a specific site is called Local meteoric water line (LMWL). A LMWL to compare groundwater from the Bedretto tunnel to has been produced by U. S. Ofterdinger (2001). This LMWL (hereafter refered to as Ticino LMWL) is based on the best fit of precipitation data from meteoric stations in the close by region (Guttannen, Meiringen, and Grimsel/Hospiz 1970–1999, Gütsch, Andermatt, Oberwald, Binn, and Robiei 1998–1999). The Ticino Local Meteroric water line is defined as the following: $\delta D = (7.65 \pm 0.05)\ \delta^{18}O + (4.7 \pm 0.77)$. The OIPC LMWL has been compiled as described in Appendix K.

[32] The welltec, MB8 and ST2 boreholes includes measurements only from fully open boreholes. The ST1 data is showing only discrete interval data, except the most enriched measurement is a measurement taken when the borehole was fully open.

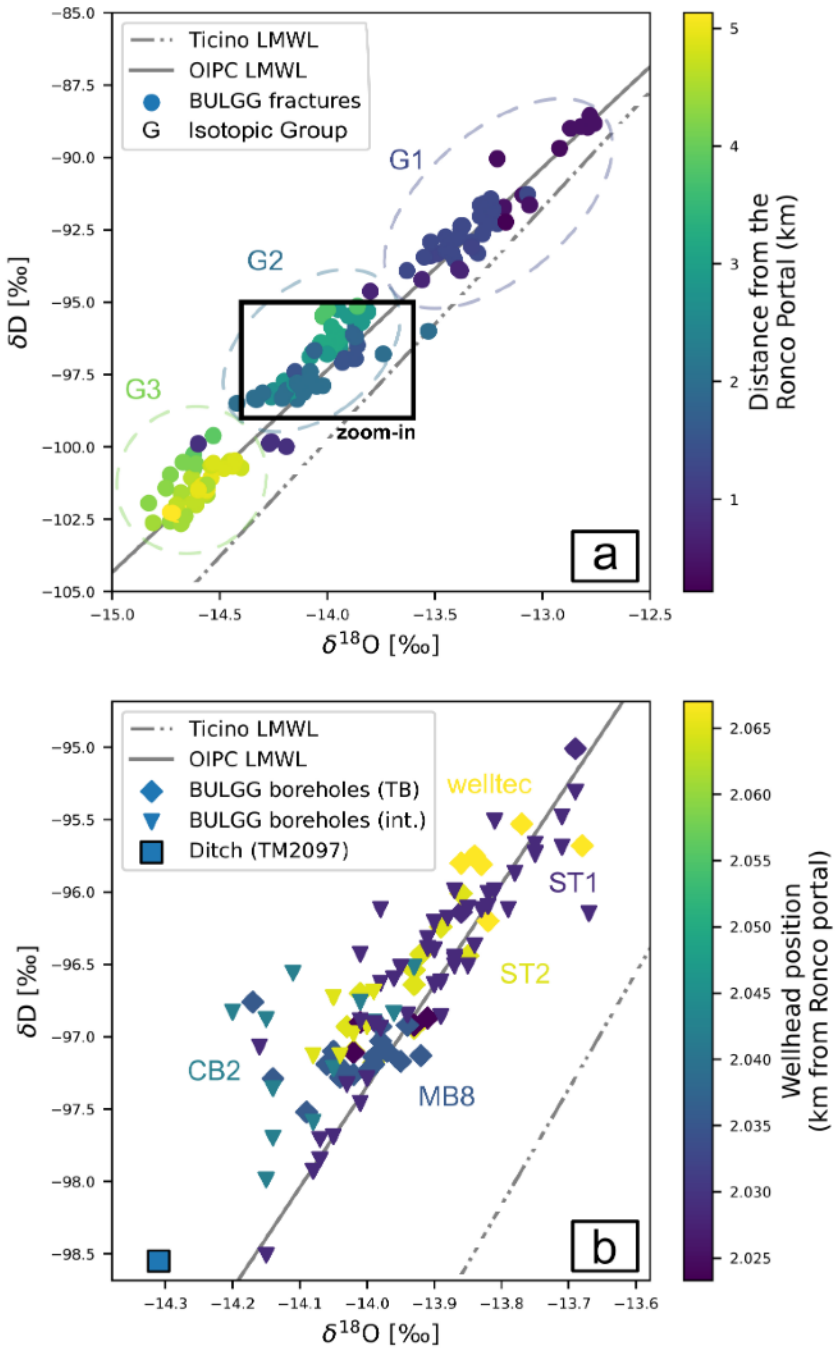

Figure 18: δ^{18}O-δD diagram showing the BULGG groundwater data. Top: Isotopic composition of the fracture fluids (color coded according the distance from the Ronco portal). Bottom: Isotopic composition of the borehole fluids (extension is a zoom-in of the black rectangle of the top subfigure), as well as the mean isotopic signature of the ditch water at TM 2097. The displayed borehole data includes fully open boreholes ('TB', diamond marker), as well as interval measurements ('int.', triangle markers). Frequently measured boreholes are annotated. LMWL = Ticino Meteoric Water Line according to (U. S. Ofterdinger, 2001). OIPC LMWL = Reconstructed Local Meteoric Water Line (see Appendix K).

Group 3 (G3) includes data from the northern part of the tunnel (TM 3750 - TM 5220). Data point corresponding to this group are as well not perfectly in line with the general trend of depletion with increasing TM, but also show a more complex pattern. Outliers in group 3 are data points in dark violet (color indicates proximity of the Ronco Portal), which are clearly not following the general trend and belong to the highly mineralised sampling site in the gneiss at TM 901.

The isotope measurements of the BULGG boreholes are matching well into the general trend observed in the spatial distribution of the observed groundwater data regarding their tunnel position. Most of the borehole data plot onto the fracture data group 2 (fracture fluids collected between TM∼1500 and TM∼3750), revealing generally a closer relation towards fracture fluids collected between TM∼2800 and TM∼3750. Fluids from shallow monitoring boreholes, like the MB8 and CB2 (∼ 200 meters deep), as well as the second stimulation borehole ST2 are ^{18}O enriched. The ST1 intervals show a large distribution in its isotopic compositions, whereas shallower intervals are generally more depleted. The welltec borehole (horizontal borehole on tunnel elevation) is showing highly isotopic enriched waters.

5.1.4 Water Quality Clusters

Both algorithms (*k-means*, *hierarchical agglomerative clustering*) have resulted in the same cluster assignment for the sampling sites. The main result of the cluster analysis is illustrated in figure 19, presented as a HC-dendrogram including Stiff diagrams. The cluster analysis proposes three clusters, each with two subgroups. The chemical characteristics of each subgroup, as well as the corresponding sites can be found in table 4.

In figure 19, it is apparent that the clusters are grouping samplings sites with regard to their spatial position along the tunnel. Cluster 1 (C1) includes samplings sites connected to the big fault zone (TM∼1300, Subgroup 2) and sampling sites very close to the Ronco portal (Subgroup 1), namely the very close fracture fluids from TM 440 and 444. The water in this cluster is generally cold (7 - 10 °C) and shows a relatively enriched isotopic composition, as well as an elevated carbonate and potassium concentration.

Cluster 2 (C2) comprises mainly sampling sites in the northwestern part of the tunnel (TM 2647 - TM 5132), including one 'outlier' from a fracture at TM 1798. The fluids are low mineralized of slightly different chemical composition compared to C1 and C3, what is nicely visualised by the Stiff diagrams in figure 19. C2 is further characterized by elevated fluoride concentration with regard to the EC. Subgroup 3 (S3) is defined by two big fault zones located at TM 2848A (high inflow sampling site) and TM 3750 (both steal supported fault zones not revealing major tunnel inflow though). The Subgroup 3 has an increased nitrate concentration of >1 ppm (trace element in the BULGG groundwaters). The other sampling sites in C2 are grouped in subgroup 4 (S4). The subgroup 4 (S4) waters are highly depleted and proportionally increased sodium concentration.

Table 4: Hydrochemical characteristics of the six subclusters (including the standard water quality parameters, the major ions, stable isotopes) and ratios of the most represented major ions in the BULGG groundwater. TA = Total alkalinity (incl. all carbonate species) The ratios are obtained from the [mEq/L] ion concentrations of the specific subgroup. Parameters marked with an asterisk (*) were originally excluded from the analysis and did not influence the HC outcome. The sampling sites included into the different clusters/ subclusters are listed in figure 19

	C1		C2		C3	
	S1	S2	S3	S4	S5	S6
Standard parameter						
T [°C]	7.57	9.50	14.16	17.38	18.12	13.73
Ph (field) [n.a.]	8.63	8.95	8.74	9.07	10.27	8.80
EC (field) [μS/cm]	142.18	161.73	58.44	112.54	359.10	699.12
TDS [ppm]	100.67	111.57	40.07	79.91	255.84	494.99
*ORP [mV]	135.65	154.56	178.21	175.33	37.76	136.54
Q [l/s]	0.03	0.06	1.72	0.10	0.55	0.01
Major Ions [ppm]						
F^-	0.40	1.17	0.97	3.26	6.11	3.11
Cl^-	0.29	1.74	0.45	0.85	5.00	8.93
*NO_3^-	0.72	0.38	1.11	0.15	0.03	0.01
SO_4^{2-}	25.82	55.16	9.17	25.98	144.55	365.49
TA	27.71	13.98	14.20	15.41	13.92	8.21
*Li^+	0.05	0.08	0.00	0.07	0.06	0.10
Na^+	2.18	6.40	4.83	13.48	27.59	48.36
K^+	5.70	0.16	0.38	0.35	0.53	0.84
*Mg^{2+}	1.48	0.29	0.19	0.10	0.08	0.28
Ca^{2+}	25.55	29.56	8.96	14.14	58.29	131.82
Ratio (obtained from conc. in [mEq/L])						
SO_4^{2-}/Ca^{2+}	0.42	0.78	0.43	0.76	1.03	1.16
SO_4^{2-}/F^-	25.57	18.67	3.82	3.14	9.35	46.34
Ca^{2+}/Na^+	13.12	5.3	2.13	1.21	2.43	3.13
Ca^{2+}/Cl^-	156.08	30.1	35.2	29.52	20.63	26.15
Stable Isotopes [ppt]						
δD	-90.22	-92.71	-95.39	-99.78	-96.75	-97.27
δ^{18}O	-12.97	-13.37	-13.92	-14.40	-13.97	-13.98

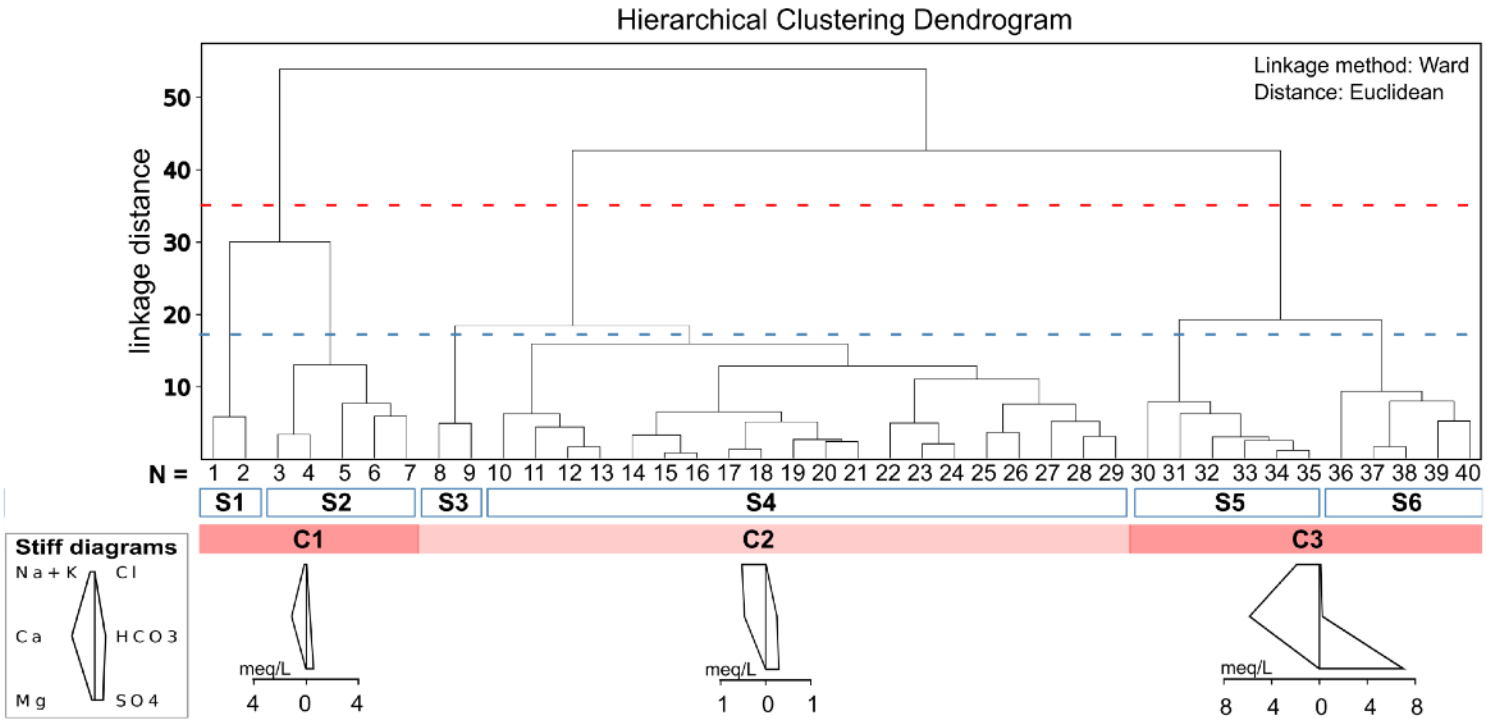

Figure 19: Dendrogram showing the outcome of the hierarchical clustering analysis. The second level clusters are indicated by C1, C2 and C3 (where C1 = Cluster 1). The Stiff diagrams show the chemical constitution of each cluster. Each bottom line (N) represents a sampling location (fractures and boreholes) at BULGG, where: 1) TM440, 2) TM444, 3) TM1306B, 4) TM1306C, 5) TM1303 ,6) TM1203A, 7) TM1306A, 8) TM2848A, 9) TM3750, 10) TM2647, 11) TM1798, 12) TM3191, 13) TM3192, 14) TM5132, 15) TM4348, 16) TM4447, 17) TM4752, 18) TM4846, 19) TM4652, 20) TM4506, 21) TM4599, 22) TM4250, 23) TM4166, 24) TM4192, 25) TM3884, 26) TM4950 , 27) TM2848B, 28) TM2794, 29) TM4268A, 30) Welltec, 31) ST1, 32) CB2 , 33) MB8, 34) MB5, 35) ST2, 36) TM901, 37) TM1973, 38) TM1993, 39) TM699B, 40) TM1494.

Cluster 3 (C3) includes the sampled borehole waters (S5) and waters from the southeastern part of the tunnel until the laboratory (TM 669 - TM 1993, S6). The C3 is characterized by highly mineralised waters, where the EC of S6 is twice as high as for S5 (BULGG borehole fluids). S5 has a relatively low redox potential and high pH.

The proximity of the clusters (indicated by the linkage distance in the HC-dendrogram in figure 19) suggest a closer relation between C2 and C3 with regard to C1. S1 and S2 are thus less similar to the other clusters.

5.1.5 Water Quality End-Members

The obtained end-members and their computed concentrations of the input parameters, as well as their reference samples (each representing one cluster) can be found in table 5 and is visualized in figure 20 (calibration plots). The end-member contributions evolution to the sampling sites along the Bedretto tunnel can be found in figure 21. The raw model outputs can be found in Appendix L (table 13 and figure 41).

In table 5 and figure 20, it is apparent that computed End-member 1 (which was calibrated with a representative sample of C3) is mainly characterized by an increased carbonate concentration (23.3 ppm) and rather enriched stable water isotopes ($\delta^{18}O$ = -12.95 ‰). EM2 (EM calibrated with a reference sample of C2) is unique due to its generally low mineralisation degree, but high fluoride (4.6 ppm) and proportionally slightly elevated sodium concentrations. EM2 further shows a depleted isotopic composition ($\delta^{18}O$ = -14.7 ‰). EM 3 (EM calibrated with a ref. sample of C3) on the other hand is defined by a high mineralisation degree, revealed by a high sulfate (519.7 ppm), calcium (151.5 ppm), sodium (100.8 ppm) and chloride (13.9 ppm) concentration (note however that the computed sodium concentration of EM3 is significantly off the 1:1 relationship) . Furthermore, EM3 has a relatively depleted carbonate content (8.3 ppm).

Note that a 1:1 relationship between measured and computed concentrations of samples + end-members in figure 20 indicates conservative behaviour of these species, and their chemical composition can be explained by mixing or processes leading to comparable patterns (observed for: sulfate, calcium, chloride). An non-conservative behaviour is observed for fluoride and carbonate, which deviate from a clear 1:1 relationship and are thus indicating water-rock interactions (geochemcial reactions) (Scheiber et al., 2020). Sodium seems to exhibit both, a linear relationship between EM1 and EM2 and strong deviations with regard to EM3.

The end-member contributions towards the sampling sites show an evolution along the Bedertto tunnel (see figure 21). The dominant contribution towards the sampling site of the EM's are generally consistent with its cluster assignment (EM1 mainly influence C1, EM2 contributes the most to C2 and EM3 influences mostly sites from C3). However, the EM 1 is surprisingly high in the intermediate and northern most tunnel section (belonging to C2). The EM1 contribution increases in conductive sections from C2. Vice verse is EM2 also contributing in conductive zones in C1. EM3 mainly contributes to the fluids in the southeastern part of the tunnel belonging to C3, where its contributions to C1 and C2 are small.

Table 5: End-Member concentrations calculated by MIX. EM = Calculated End-Member, Ref. = Reference Sites based on HC clusters. Ref1 = TM 1306A, Ref2 = TM 4447, Ref3 = TM 901. Species: 1 = Fluoride [ppm], 2 = Chloride [ppm], 3 = Sulfate [ppm], 4 = Total Alkalinity [ppm], 5 = Sodium [ppm], 6 = Calcium [ppm], 7 = δD [ppt], 8 = δ^{18}O [ppt].

	Species Concentration							
	1	**2**	**3**	**4**	**5**	**6**	**7**	**8**
Ref1	0.95	1.04	27.04	16	3.32	21.94	-13.28	-92.05
Ref2	4.55	0.79	15.76	15.83	17.41	9.4	-14.71	-102.51
Ref3	2.87	13.86	519.73	8.33	100.83	151.48	-14.33	-99.9
EM1	0	0.99	31.39	23.32	0	20.68	-12.95	-89.24
EM2	4.55	0.79	15.76	15.83	17.41	9.40	-14.71	-102.51
EM3	2.87	13.86	519.73	8.33	100.83	151.48	-14.33	-99.90

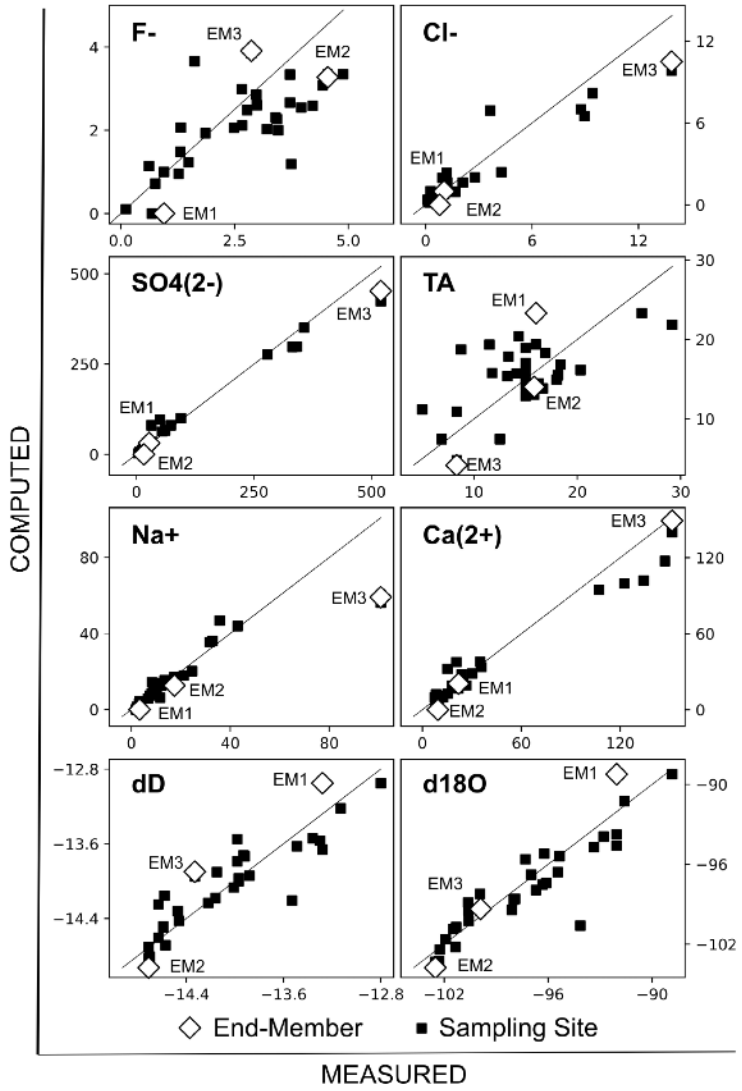

Figure 20: Computed versus measured concentrations (ppm) of the species included in the MIX analysis of all sampling sites and end-members.

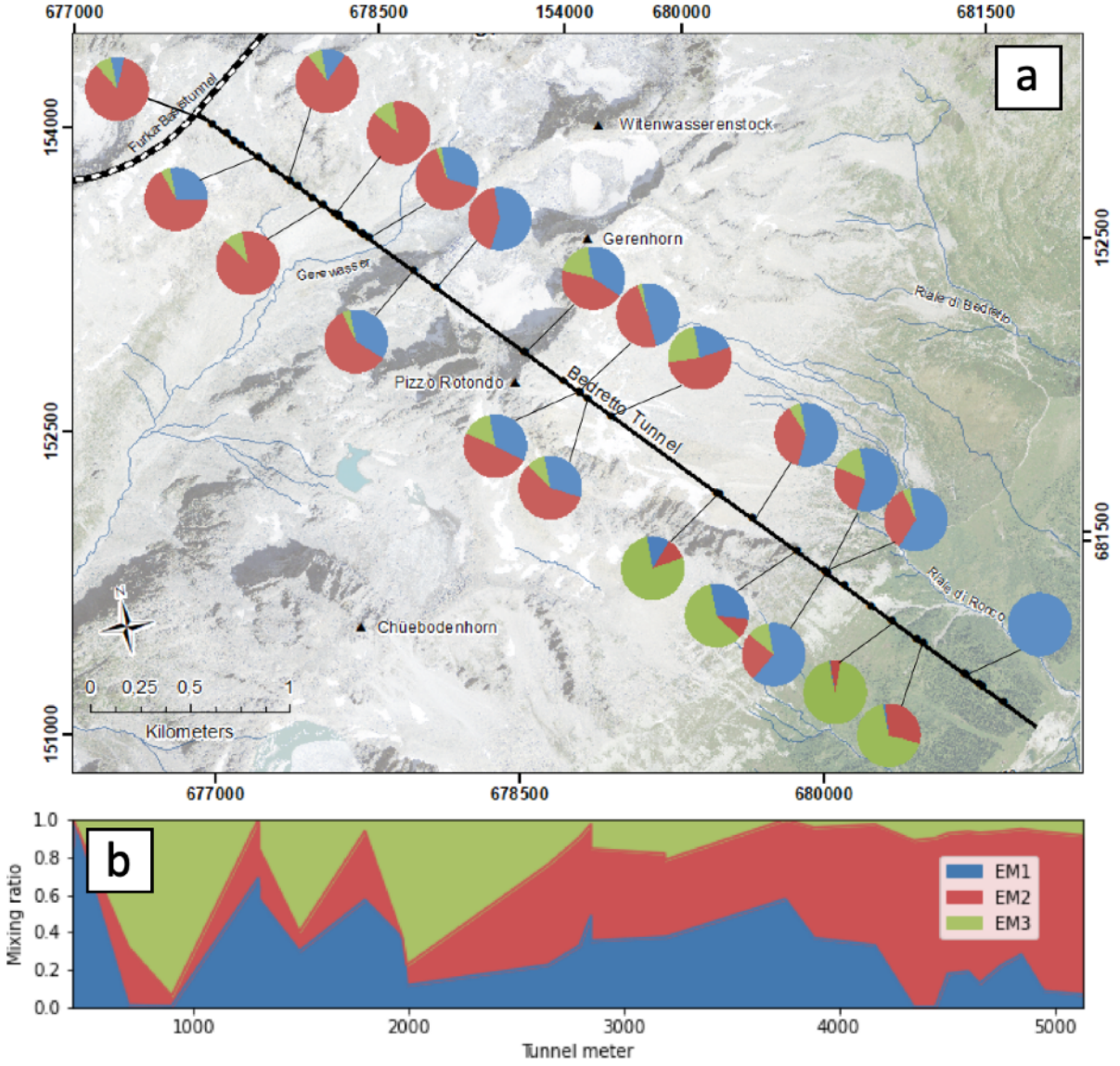

Figure 21: Spatial mixing ratio evolution along the Bedretto tunnel. (a) Pie chart visualization (b) Stack-plot visualization.

5.2 Temporal Hydrochemical Trends

The temporal variability of the parameters expressed as mean coefficient variations (CV_{mean}) can be found in table 6. Figure 42, 43 and 44 in the Appendix M depicts the temporal evolution (time series) of the standard water quality parameters, as well as the anion and cation concentrations through out the sampling year of the fracture fluids.

The CV_{mean} for the major ions vary between 6.7% and 48.1%, except for following ions: nitrate, lithium and magnesium. These ions showed very high CV_{mean}, exceeding 100%. The CV_{mean} for the standard parameters are below 22.1%. The lowest CV_{mean} could be observed in the stable isotopes, where the CV_{mean} is below one.

In the timeserie-figures, one can see that many parameters (certain ions and the EC/TDS) show a drastic decrease between August 2020 (sampling start) and November 2021 (see figures 42 - 44). However, these decreases are understood to be caused by instrument issues, such as i) readjustments of the IC standards during that time period (concerning the ions) and ii) change of the field meter (concerning the standard parameters).

The only parameter where a possible seasonal pattern could be suspected during the sampling period is temperature. The temperature indicates a slight decrease during winter 21 for sites of lower temperatures (thus site locations mainly linked to the southeastern most tunnel section, close to the Ronco portal).

Table 6: Mean coefficient variations (CV_{mean}) of the hydrochemcial parameters. TA = Total alkalinity.

Parameter	F^-	Cl^-	NO_3^-	SO_4^{2-}	TA	Li^+	Na^+	K^+	Mg^{2+}	Ca^{2+}
$\mathbf{CV}_{mean}$	27.3	48.1	104.6	6.7	18.1	200.7	7.9	28.1	152.6	11.4
Parameter	T	pH (field)	pH (lab)	EC (field)	EC (lab)	TDS	ORP	Q	$\delta^{18}O$	δD
$\mathbf{CV}_{mean}$	4.6	5.0	4.6	8.7	8.5	8.5	21.3	25.5	0.6	0.3

5.3 Surface Water Composition

The spatial distribution of the EC, pH and $\delta^{18}O$ results of the surface water bodies can be found in figure 45 (Appendix N). Figure 39b (Appendix J) shows the $\delta^{18}O$/ δD diagram including BULGG groundwater data compared to the samples collected from surface water bodies.

The electrical conductivity of the surface water present above the study area is generally very low. The glacier lake measurements do not exceed 10 μS/cm. The mean electric conductivity of all measured streams in vicinity to Ronco portal is 21 μS/cm. The EC of the precipitation samples taken at the Ronco Portal is $\sim$18 μS/cm.

The pH of surface waters generally is close to neutral to slightly alkaline (most measurements were between 7 and 8). The highest pH (9.3) was measured in rain water.[33]
The ionic composition of the surface water vary in composition. The precipitation water includes calcium, sodium, chloride, potassium and magnesium with decreasing concentration. Among the

[33]Note that the pH results of low mineralised water have to be treated with caution, as discussed in section 6.3

ionic constituents, the calcium concentration contribution is with 1.3 ppm the very highest. All other ions are between 0.1 - 1 ppm. Fluoride and nitrate could be detected in very low concentration (< 0.1 ppm). The stream and spring waters are defined by sulfate, calcium, nitrate sodium (> 1 ppm). Below 1 ppm the stream waters contain potassium, fluoride, magnesium, and chloride. The ion of highest concentration is sulfate (in average ∼13 ppm), as observed for the groundwater but not detected in precipitation.[34] Of higher mineralisation degree is only the Ticino river (EC > 400 μS/cm). The dissolved ions in the Ticino river are mainly characterized by sulfate (∼219 ppm) and calcium (about 86 ppm). Other constituents (magnesium, potassium, sodium, chloride) are below 2 ppm. The ionic concentrations are generally between 1.05 x (sodium) - 16 x (sulfate) higher compared to what was observed in the streams. Exceptions are the fluoride and nitrate ions, which are less concentrated in the Ticino river water.

The isotopic composition measured in precipitation showed large seasonal variations. The precipitation data (including rain and snow samples at the Ronco portal), representing samples between March 2020 and May 2021, show an average δ-value of -8.64‰/ -57.57‰ (δ^{18}O/ δD). The rain water is with a δ^{18}O/ δD of about -5.5‰/ -30‰ more enriched compared to the snow in March (-12.44‰/ -89.88‰), as well as the snow in April (-11.20‰/ -79.91‰). The isotopic composition for the measured stream waters (most of the samples were collected on the 27.06.21) seems to depend on their emergence height. The average measured value is -13.94‰ (σ_{mean} = 0.58‰) and -97.15‰(σ_{mean} = 3.69‰) for the δ^{18}O and δD, respectively. All stream measurements can be found in figure 45 (Appendix N).

In figure 39b (Appendix J) it is apparent that most surface samples plot onto or very close to the BULGG groundwater isotope samples, except the precipitation data. The snow samples are plotting on the global meteoric water line (GMWL), whereas the rain water samples plot on the Ticino meteoric water line (LMWL).

5.4 Hydrochemical Monitoring During Hydraulic Stimulation

5.4.1 Long-term Monitoring: CB2 Borehole Intervals

As suitable conservative tracer to perform long-term monitoring in the CB2 borehole, stable isotopes were chosen (see Appendix P for a detailed description of tracer selection).

Figure 22 displays the isotopic composition of interval samples taken between the 21.12.20 and the 24.05.21. In the subfigure 22a one can see the CB2 isotope measurements in relation to the estimated baseline of the injection fluid.[35] In the subfigures 22c to 22f, one can see the temporal evolution of the isotopic composition in different CB2 depths (intervals).[36] Table 7 reveals the changes between the first and last measurement in each interval. Notable is the increasing depletion in the δ^{18}O trend along the borehole towards the interval 3 (deepest interval). The δ^{18}O does not

[34] Note that the ion concentration determination in such low mineralised fluids is connected to uncertainties, as discussed in section 6.3

[35] For further information about the baseline estimation, see Appendix Q.

[36] The intervals correspond to the following borehole depth ranges (where 0m = wellhead) : Interval p3: 177.24 - 195.24m, Interval p4: 166.73 - 175.73m, Interval p5: 156.19 - 165.19m, Interval p7: 125.14 - 140.14m.

show a clear trend with depth. The intervals p3 and p7 decreased, whereas p5 even got enriched in the heavy ^{18}O between December 20 and March 21.

The measured isotopic shifts are exceeding the instrument precision (δD : < 0.1‰, $\delta^{18}O$: < 0.025‰.). The shifts are furthermore below the mean isotopic variability encountered in BULGG groundwaters during the sampling period ($\delta^{18}O$ σ_{mean} = 0.077‰ / δD σ_{mean} = 0.26‰). However, the maximum variability of the $\delta^{18}O$ and δD measured at BULGG ($\delta^{18}O$ σ_{max} = 0.4‰ / δD σ_{max} = 1.12‰) exceeds the isotopic shift observed in all intervals.

Table 7: Isotopic changes between first and last measurement of different intervals (depths) in the monitoring borehole CB2.

Interval	δD [‰]	$\delta^{18}O$ [‰]
p3	-1.23	-0.14
p4	-0.82	+0.01
p5	-0.76	+0.12
p7	-0.28	-0.18

5.4.2 Long-term Monitoring: TM 1993 Fracture

As suitable conservative tracer to perform long-term monitoring in the TM 1993 fracture, stable isotopes were chosen (see Appendix P for a detailed description of tracer selection).

Figure 23 displays the temporal evolution of the flow rate, EC, temperature and the conservative tracers (stable isotopes) measurements taken during the sampling period in the fracture TM 1993.

The temporal evolution of the conservative tracers ($\delta^{18}O$ / δD) do not show any clear signal after the stimulation works. The isotopic variability encountered at fracture TM 1993 expressed as standard deviation is for $\delta^{18}O$ σ_{mean} = 0.067‰/ δD σ_{mean} = 0.26‰ what is comparable to the natural temporal variability (expressed as mean standard deviation) of $\delta^{18}O$ σ_{mean} = 0.077‰ / δD σ_{mean} = 0.26‰ in BULGG groundwater.

Very interesting to note is temporal EC evolution in the fracture at TM 1993. The EC curve shows two depressions, both possibly related to the hydraulic stimulation (dilution signal starting few weeks after the stimulation and lasted over few months) and a recovery in between towards the TM 1993 baseline. The EC decrease after the 2020 stimulation shows a maximum (measured) dilution mid January. The signal is 98 μS/cm below the expected baseline at 706 μS/cm, which would imply a contribution of injection water of 16%. The signal after the 2021 stimulation has its peak beginning of July, 33 μS/cm below the estimated baseline, what would correspond to a mixing ratio of 6% injection water. Both EC peaks exceed the mean standard deviation of 16.6 μS/cm obtained for the BULGG groundwater significantly. The EC trend is not related to the temperature or the flow rate.

However, the EC was excluded as a suitable tracer for the TM 1993 fracture because the ions did not exhibit conservative behavior under the prevailing environmental conditions (see Appendix P). Furthermore, the EC evolution could not be reconstructed by any other ion (which could be expected from sulfate and calcium, since these ions are closely related to the EC, see section 5.1.2).

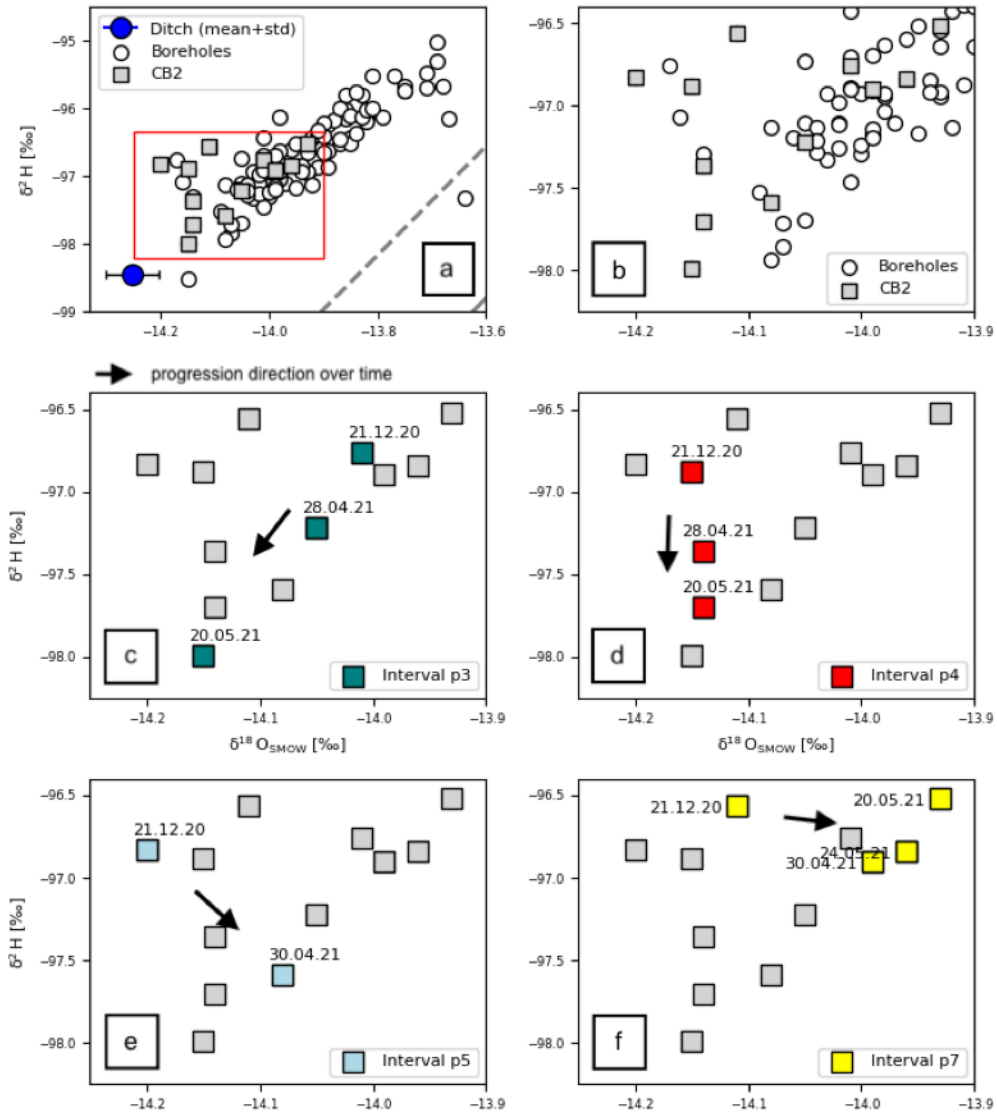

Figure 22: Long-term monitoring: Isotopic composition displayed in δ^{18}O-δD diagrams of four CB2 intervals during the sampling period. (a) All borehole measurements (circles), including the CB2 measurements (squares), as well as the estimated baseline of the injection (ditch) water. The grey line is showing the Ticino LMWL, (b) Zoom-in of the red square in subfigure a), (c) Interval 3 measurements labeled with the sampling date, (d) Interval 4 measurements labeled with the sampling date, (e) Interval 5 measurements labeled with the sampling date, (f) Interval 7 measurements labeled with the sampling date.

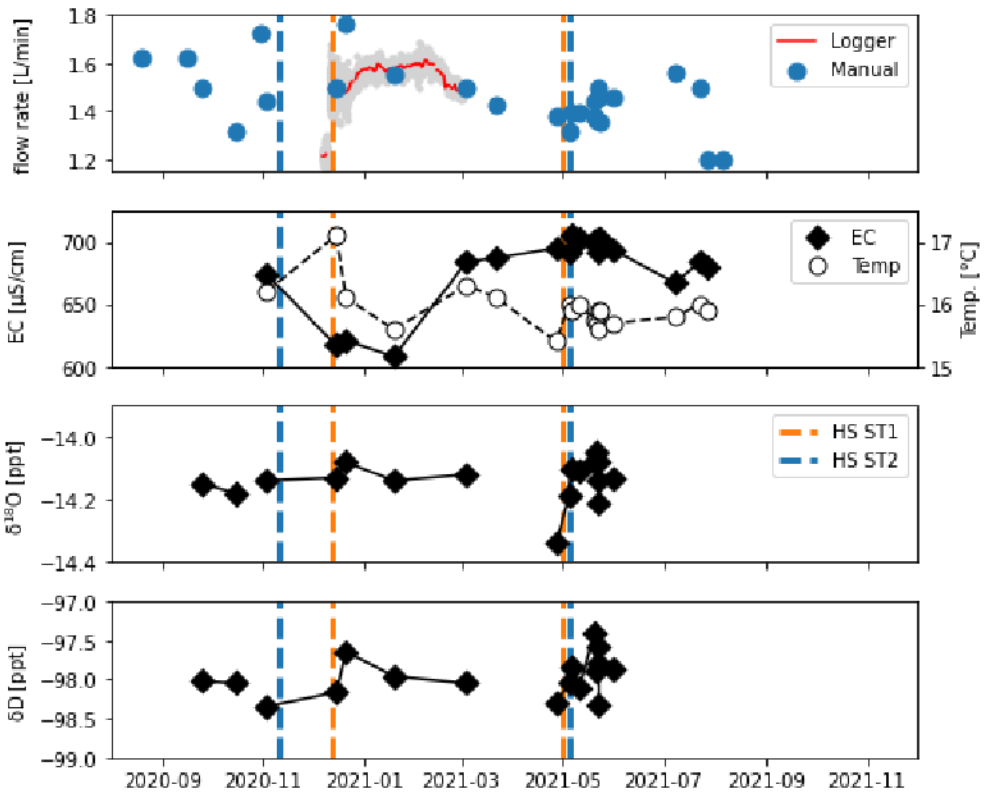

Figure 23: Temporal EC, T, Q and conservative tracer (δ^{18}O/ δD) evolution of the TM 1993 fracture fluid.

5.4.3 Short-term Monitoring: ST1 int1+2

For the short-term monitoring of ST1, the EC, the stable isotopes and the calcium and sulfate concentrations were estimated as suitable tracers (See Appendix P for a detailed description of tracer selection). The subfigures 24a - c depict the temporal EC, calcium concentration and δ^{18}O evolution during the monitoring experiment described in section 4.2.3. Note that the other suitable tracers (δD and sulfate) were not included into the figure, since they similarly develop like δ^{18}O value and calcium concentration, respectively. The continuous EC data in subfigure 24a is collected by a EC-logger (LG), where the point measurements (triangles) correspond to an EC measurement with the field meter (FM).[37] Both, the EC (subfigure 24a) and calcium (subfigure 24b) measurements show the same temporal patterns. First one can observe an increase in the EC/ calcium concentration.[38]

[37]The logger and the field meter showed an EC offset of few 10's of μS/cm, which had to be adjusted as described in Appendix R. However, note that the baseline estimation deviates even after the data adjustments, as indicated in figure 24

[38]The increasing EC prior to the dilution signal corresponds to the last stage of the recovery phase. The EC at interval opening was at 320 μS/cm, increasing steadily towards the baseline within about one day. The recovery curve has been cut to obtain a better resolution of the dilution signal. The entire evolution of the curve can be found in figure 46, Appendix R).

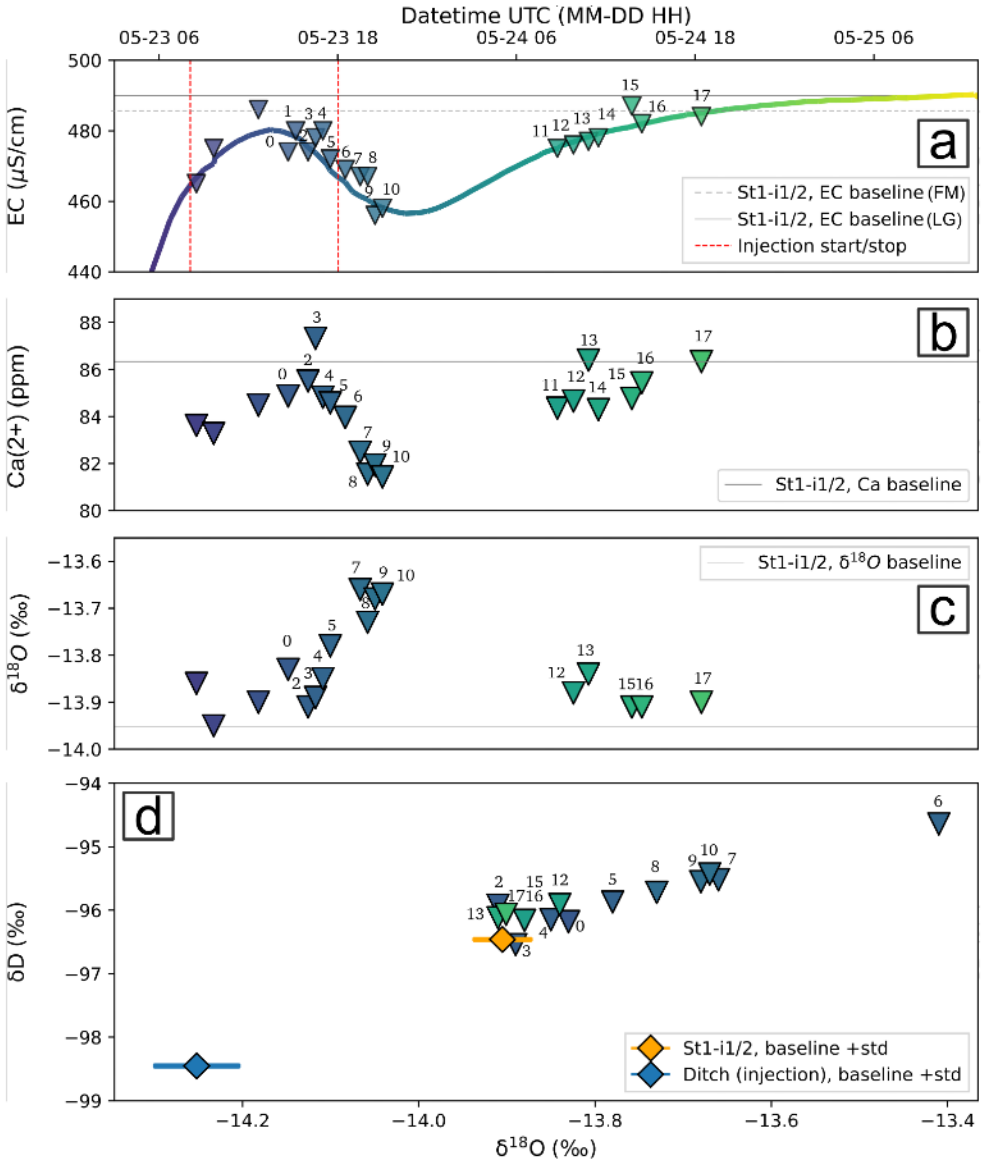

Figure 24: Short-term monitoring: EC, calcium and the stable water isotopes evolution of the ST1 interval 1+2 outflow before, during and after the ST2 injection. (a) Continuous EC logging and timepoint EC measurements (+ fluid sampling), (b) the calcium concentration, (c) the δ^{18}O value and (d) the isotopic composition (δ^{18}O versus δD) of the probes taken prior, during and after the injection. The color code is according to the datetime. Note that sample 6 had been excluded for the stable isotope evolution, since it was detected as outlier.

Shortly before reaching the baseline values (which was estimated at 490 μS/cm for the logger and 486 μS/cm for the field meter, see Appendix Q), a dilution signal starts after 5.5 hours of injecting in ST2. The signal peak (maximal dilution) occurred 14.5 hours after starting the injection and would correspond to maximum mixing ratio of 8.3% injection water mixed with 91.7% formation

water. The manually measured EC would imply a maximal mixing ratio of 7% injection water (note that maximum peak was during night time and thus missed in all manual measurements/ probes). The calcium and sulfate concentrations suggest a maximum mixing ratio of 6.6% and 7% injection water, respectively. After the signal has reached its maximum, the EC and calcium value recovered and asymptotically approached the baseline value (which was reached about two days after the onset of the signal).

Subfigure 24c shows the $\delta^{18}O$ concentration of corresponding probes taken during the EC-dilution signal. The signal pattern is comparable to that observed with EC and calcium concentration. However, instead of moving towards the baseline of the depleted injection fluid, the stable isotopes indicate a mixing with a more isotopic enriched source. Subfigure 24d shows this phenomena in a $\delta^{18}O$ - δD diagram, where the measured isotopic composition of the probes taken during the dilution signal are displayed with respect to the baselines of the formation water (ST1 interval 1+2, in orange) and the injection water (ditch, in blue). In Figure 25, the mixing signal was placed in the context of all measured borehole and fracture fluids at BULGG to be able to find an approximation of the mixing signal to a known groundwater (assuming a binary mixing problem). Figure 25 provides two observations: i) none of the measured isotopic compositions of BULGG groundwater (in reasonable distance to the reservoir) could potentially act as a second component in a binary mixing process and ii) the estimated binary mixing line slope deviates from the linear relationship of the BULGG groundwater isotopic composition.

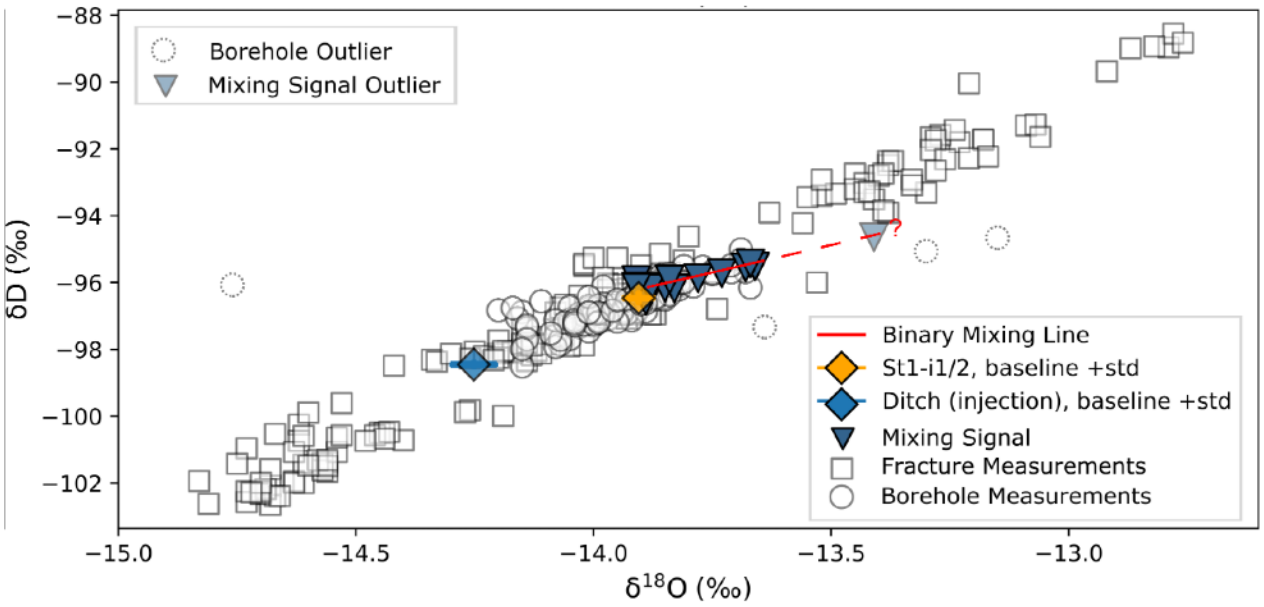

Figure 25: Reconstruction of the indicated mixing line, based on the isotopic signal evolution during the short-term monitoring experiment of ST1 int1+2.

When comparing these results with the in figure 47 (Appendix S) depicted evolution of the downhole (injection) pressure of the stimulated part in ST2 (PS in figure 47), the downhole pressure of the ST1 interval 2, as well as the flow rate of the ST1 outflow, it is apparent that the flow rate, the down hole pressure in ST1 and the hydrochemistry are behaving very comparable. The EC (dilution) signal started simultaneously to the flow rate and pressure increase in ST1 and almost simultaneously to the third stimulation stage (increase to a ST2 down hole pressure of > 25 MPa). However, the hydrochemcial signal peak arrives about four hours later compared to the flow rate and pressure signal (slight delay of the hydrochemcial signal).

6 Discussion

The first section of this discussion, it is aimed to relate the accounted spatial and temporal hydrochemical variability to differences in the water origin, sources, path ways and geological conditions. In the second section, the potential hydrochemical shifts observed during hydraulic stimulation campaigns (within the reservoir during a cross-borehole monitoring experiment and in the close vicinity of the stimulated reservoir) will be discussed with regard to potential mixing processes. The remaining sections deal with the measurement uncertainties as well as a comparison with the mixing analyses performed in the Grimsel ISC experiment and suggestions for improving the BULGG data set.

6.1 Hydrochemical Characterization

6.1.1 Water Origin

To estimate water origin, studies use the approach of stable water isotopes and its relationship to the Local Meteoric Water Line (LMWL) (Gat, 1971). Isotopes are understood to behave conservative (non-reactive), where the isotopic composition of infiltrated meteoric water can still be observed in the deep underground (Jasechko, 2019). However, this approach does not account for old groundwaters. Studies made in deep (∼1 km below surface) crystalline basement brines (old strongly mineralised groundwater) reported shifts in the $\delta^{18}O$ value, where many authors expect water-rock interactions (fractionation between chemical species) or isotope exchange processes as driving forces (aging effect). Such processes then can be observed in a shift away from the meteoric water line (e.g. ^{18}O enrichment or depletion, depending on the temperature (Kloppmann et al. (2002); Gat (1971)). The fact that the BULGG stable water isotope data is plotting very closely to the OIPC-LMWL (the reconstruction procedure of the OIPC-LMWL can be found in figure 40, Appendix K), thus suggests a meteoric origin under present-day climatic conditions. The meteoric origin is supported by the fluid temperatures measured in the Bedretto tunnel, where (except the negative anomalies) the overburden depth and temperatures are correlating. Negative thermal anomalies along preferential pathways as well support meteoric origin, rather than upwelling deep hydrothermal fluids (which could be assumed to cause positive temperature anomalies).

The deuterium excess (d-excess) can provide information about the moisture source of meteoric water.[39] According to Bershaw (2018), a high d-excess (∼15 ‰ as in average observed in the Bedretto tunnel) suggests a source in the modern Mediterranean, possibly enhanced by i) a reduced subcloud evaporation effect due to lower evaporation at high altitudes (lower temperatures and shorter path way of the rain drops) or ii) a large contribution of winter precipitation towards the

[39] Where $\delta^{18}O$ and δD at middle-to-high latitudes mainly depend on the temperature (which in mountainous regions is primarily controlled by the altitude), the deuterium excess is related to the oceanic source of precipitation. The higher the kinetic fractionation is during evaporation, the higher the d-excess. The kinetic fractionation depends on how much diffusion occurs during evaporation and is primarily dependant on the relative humidity at the vapor's evaporative source. This causes generally lower d-excess in the summer vapor and higher d-excess in winter vapor (Bershaw, 2018).

groundwater (larger deuterium fractionation due to a low relative humidity over the ocean). The presence of such effects is also emphasized locally by the observed d-excess increase in the BULGG groundwater (the farther one is from the Ronco portal), where i) the topography forces clouds up to higher elevations and thus to a reduced evaporation in the subclouds and/or ii) an increased contribution of winter precipitation in higher altitudes can be assumed (longer winter season). The water collected in the northernmost tunnel part again shows a diminished deuterium excess. The decreased d-excess signal might reflect the isotopic composition of the glaciers on the surface above this tunnel section, providing a sub-modern isotopic record Bershaw (2018). Such a glacier signal can include winter precipitation in the order of the last 10 to 1000 years and thus indicate spatio-temporal changes in vapor source over a long time period (Bershaw (2018); Jansson et al. (2003)).

6.1.2 Recharge Elevations and Water Sources

Apart from the water and moisture origin, the isotopic composition can also be used to reconstruct potential precipitation elevations of the groundwater (as performed by U. S. Ofterdinger (2001)) and helps to detect contributions of (additional) water sources.

Here, the precipitation elevation was obtained by the OIPC (note that the calculator only accounts for location and altitude) and was compared to the isotopes of the BULGG groundwater. This comparison allows a good estimation of the precipitation elevation of the BULGG groundwaters, when assuming the high isotopic variability of the groundwater in the study region is primarily reflecting the large topographical differences (about 1.5km) and the corresponding temperature dependent altitude effect.

A convenient way to assign precipitation altitudes to the BULGG groundwater data is to use subgroups of isotopic similar waters. As mentioned in section 5.1.3, one can distinct three groups with similar isotopic fingerprints (compare figure 18). The first group belong to Bedretto tunnel inflows in the southern part (TM 0 - TM 1500), the second group to the intermediate part around the Bedretto laboratory (TM 1500 -TM 3750) and the third group to the northern most part (TM 3750 – TM 5132). When comparing the isotopic signal of these groups to the estimated precipitation elevation, it is apparent that waters collected in group 1 would show isotopic compositions related to precipitation elevations between 2000 – 2400 m asl. The second group would correspond to precipitation elevations between 2500 – 2700 m asl, whereas the group 3 would indicate an isotopic composition precipitated between 2800 – 2900 m asl.

However, as mentioned above, the precipitation elevation estimation by the OIPC is only taking into account the local altitude effect, whereas the estimated precipitation altitudes might however also reflect further important (fractionation) processes which could change the isotopic composition of the groundwater, such as e.g. i) major geographic displacement of precipitation towards lower-elevated infiltration areas, ii) mixing with non-meteoric water bodies, iii) seasonal differences in the recharge contribution, iv) surface water bodies strongly influenced by evaporation or v) paleo-water contribution of different isotopic composition in glaciers (Gat, 1971). Therefore, the OIPC

precipitation elevation outcome was further compared to areas of high recharge rates (modeled by U. S. Ofterdinger (2001), see section 2.4.2), which are assumed to contribute the highest amount of water towards the isotopic groups in the tunnel. This comparison allows a rough estimation of the above mentioned potential interference of the isotopic composition, which would be indicated by a miss-match of the estimated precipitation elevation and the elevation of modeled areas of dominant recharge.

The comparison revealed deviations between the modeled dominant recharge area (which is the mid- and down-slope of the northern Bedretto valley flank between up to ∼2250 m asl) and the estimated precipitation elevations of the isotopic group 1. Group 1 shows a slightly more depleted isotopic composition (corresponding to precipitation altitudes between 2000-2400 m asl), than what would be expected from the isotopic composition of the annual precipitate directly recharging in the recharge area (not exceeding 2250 m asl). Assuming the modeled recharge area is correct, this indicates a miss-match between the recharge area elevation and the precipitation elevation estimation. A reasonable explanation therefore could be a contribution of more elevated (thus more depleted) surface source, deported to lower elevations by surface run-off or subsurface flow patterns. The present streams (which geographically emerge at ∼ 2000 - 2600 m asl on the upper-slope section of the northern Bedretto valley flank and are more depleted) could represent to such a potential source.[40] Another explanation could be an increased contribution of depleted winter precipitation, however, this effect would be expected to be seen in all the isotopic groundwater data at BULGG (and to a higher extent in the isotopic group two and three).

However, apart from these smaller deviations between the estimated precipitation elevation and the modeled recharge areas in the isotopic group 1, the obtained precipitation elevation data (of group 2 and 3) matches well to the modeled dominant recharge areas of the isotopic groups 2 and 3. The second isotopic group shows isotopic signatures indicating precipitation elevations of 2500 – 2700 m asl (matching to direct infiltration of precipitation at the recharge areas in the vicinity of Rotondo summit and shows a comparable isotopic composition to the Riale di Ronco stream water, which is sourcing close to the Pizzo Rotondo). The third group exhibits precipitation elevations of about 2800 - 2900 m asl, which fits well with the altitudes of the glaciated areas (∼ 2700 - 3000m asl) of very high recharge rates. It is surprising that no overestimation of the precipitation elevation was obtained for the isotopic group 3, what could have been assumed due to an expected high contribution of depleted glacier melt water towards this isotopic group (already indicated by the d-excess, see section 6.1.1). However, this technique of comparing modeled recharge altitudes with calculated precipitation elevations is linked to many uncertainties (like the model performance/ uncertainties or measurement uncertainties) and simplification, what allows only a very rough estimation, which is thus not very sensitive to smaller isotopic deviations, as e.g. detecting a d-excess.

[40]Interesting to mention is especially the similarity of the isotopic composition of the Riale di Gallinoso (SW of the tunnel) towards the isotopic group 1 (see figure 39b in Appendix J). However, it must be noted that the stream water isotopic composition might change considerably throughout the year, due to seasonal variations in snow and glacier water contribution. The samples were collected during the end of snow melting (and at the peak of glacier melting) in June. The surface samples in June are expected to strongly be influenced by the depleted winter melt water and thus might act only as a temporal end-member of the southern BULGG groundwater.

The fact that estimated precipitation altitudes generally match to dominant recharge areas, as well as that the signal can be tracer down to the tunnel elevation supports the importance of direct precipitation (sub-)vertical flow paths. This trend is supported in even greater depths below tunnel elevation, by the isotopic composition of the BULGG boreholes. The isotopes fit very well with the general trend along the Bedretto tunnel and relate to precipitation elevations present when projecting their tunnel location onto the surface.

6.1.3 Fluid-Fluid Interactions

The encountered spatial variability and large hydrochemical changes along the Bedretto tunnel indicates a rather reduced lateral fluid mixing (which would homogenise the fluids), what supports (sub-)vertical fluid flow along preferential pathways with reduced interconnections. An exception might be the northern most tunnel section, where rather similar waters can be observed with respect to the dissolved ions, the stable isotopes and waterquality parameters (compare sections 5.1.1, 5.1.2 and 5.1.3). This either indicates i) very similar source conditions and overprints in the subsurface or ii) a better interconnection between the fluid pathways and thus enhanced lateral fluid-fluid interactions. Latter is supported by the fact of having a very densely fractured rock mass in this section (compare fracture spacing data in figure 12) and thus likely a better interconnected fracture network. This is less the case in the first 3000 tunnelmeters, where the fractures spacing is generally high and tunnel inflows are dominated by isolated and condensed inflows.

The temporal evolution of the parameters indicate no clear seasonal pattern and are most likely connected to random temporal variability and measurement uncertainties. The minimal seasonal effect observed at BULGG implicates to have a storage groundwater body where seasonal patterns diminish in the subground, likely through vertical fluid-fluid interactions (hence homogenisation occurs). However, some evidence exists that seasonal dependent changes occur in very conductive zones in the southern tunnel section close to the Ronco portal (as suspected in the temperature evolution), what would imply slight preservation of seasonal patterns in such zones due to rapid fluid propagation and thus slightly reduced vertical mixing.

6.1.4 Water-Rock Interactions

Since the surface sources show consistently a very low ion content and no major anthropogenic contamination is expected, it is assumed that the ionic imprints are to a great extent caused by reactions taking place in the underground. The fact that the measured dissolved ion compositions are very nicely fitting to the geochemistry of igneous rocks (Freeze & Cherry, 1979) (especially to granitic and gneissic rocks of the Central Alps (Bucher & Stober (2010); Wanner et al. (2020)), supports that the hydrochemical imprints are mainly reflecting geochemical water-rock interactions (WRI) along the taken pathways.

The encountered ionic composition of the Rotondo granite groundwater is mainly defined by sulfate, carbonate, chloride, fluoride, calcium and sodium. A geochemical source of calcium in granites and gneisses are generally understood to origin from plagioclase dissolution (anorthit, Ca-

end-member) (Bucher & Stober, 2010), which is highly abundant in granite (see section 2.3.1). The sulfate content in granitic rocks is believed to be due to oxidation processes of sulfides (Bucher & Stober, 2010). In the Rotondo granite primary and secondary (present in structural features) pyrite would ensure such a source (see section 2.3.1). Sodium is typically released from the dissolution of Na-feldspars (albit). Albite is very abundant in the Rotondo granite and increases with distance to the intrusion margin. The sources of chloride in granites and gneisses is understood to be incorporated old pore water, since in such host-rocks no Cl-donating minerals are present (Bucher & Stober, 2010). This is why chloride is understood to show a conservative (non-reactive) behaviour and continuously increase in granitic/gneissic rocks with longer residence times.[41] The geochemical source for the fluoride is generally expected from minerals like apatite, fluorite, biotite and/or hornblende (Brindha & Elango, 2011). In the Rotondo granite, a geochemical source for fluoride might thus be biotite (5 - 10%) and/or apatite (< 1%). A carbonate source in fractured crystalline rocks in the Central Alps is understood to be from dissolution of secondary and fissure calcite and related carbonates (observed in the Gotthard Rail Base Tunnel) (Bucher & Stober, 2010). A remarkable amount of secondary carbonate is present in the Bedretto tunnel in the structural features (V. H. Lützenkirchen, 2002).

The geochemical sources in the precariscian gneisses are very comparable. The main geochemical differences of the Rotondo granite towards the geniss units are defined by higher content in sodium (PS), magnesium (TS), potassium (TS) and the carbonate (TS/ PS) concentration. The carbonate content is high in most of the lithologies of the Tremola- and Proto-series (up to 15 - 20% in the Hbl gneisses and schists), what explains the increased carbonate concentrations measured in the TS and PS. The waters sampled in the Prato-series show further very high sodium concentrations in proportion. The elevated Na content in the PS is most likely due to the abundant mica gneisses (consist of 75 % felspar with an albite content between 75% to 100%). It is further apparent that the ion composition within the Prato- and Tremola-series is more variable, what is in line with the meter-scale changes of the mineralogy in this first 1.4 tunnel kilometers reported by Hafner (1958).

It is expected that there are two main types of water-rock interactions at BULGG: i) water-rock interactions that have site-wide constant 'productive' geochemical sources, and ii) water-rock interactions that are based on local variations of the geochemical source productivity. The site-wide 'constantly productive' water-rock interactions are believed to cause the contribution of major ions which exhibit a significant linear correlation to each other and the EC (means that the groundwater ionic overprint is for all these species increasing in the same way). This concerns the following ions: SO_4^{2-}, Ca^{2+}, Cl^- and Na^+. It is expected that these species can be used as a rough qualitative indicator of residence times in the subground. On the one hand, this expectation is based on the fact that chloride is considered conservative (see above). The correlation between chloride and sulfate, sodium, calcium indicates that these species are behaving also kind of 'conservative' with respect to their continuous accumulation with increasing WRI time (supported by a site-wide constant

[41] Chloride uptake is thus technically not a water-rock interaction, but a fluid-fluid interaction (mixing with indigenous pore water).

productive geochemical source) and thus residence times. On the other hand, the expectation is based on the fact that these species (SO_4^{2-}, Ca^{2+}, Cl^-, Na^+) accurately mimic the fracture network interconnection degree (see section 5.1.1, section 5.1.2) and thus qualitatively indicate conductive zones at BULGG, where fast fluid propagation/ low residence times can be expected. Note that the exact residence times can not be estimated with these species, since there are several processes which can interfere with the non-conservative ion concentration (SO_4^{2-}, Ca^{2+}, Na^+). Two examples are: 1) reduced WRI in preferential pathways with large apertures where much of the water is not in direct contact with the rock face (which could lead to an underestimation of residence time) or 2) changing precipitation-dissolution equilibrium with changing hydrochemcial conditions (like fracture aperture, depths, temperature, redox potential, etc.) can considerably change a species behaviour. Ions which do not show such a site-wide behaviour (no inter-correlation), are expected to have a more local geochemical source (varies along the Bedretto tunnel in its productivity). Such local phenomena at BULGG mainly concerns the fluoride and carbonate concentrations. As mentioned above, geochemcial carbonate sources in the Bedretto tunnel are present i) in a primary form in the gneiss unit and ii) in a secondary form in structural features. This might explain an increased carbonate content in the TS, however, not the exceeding dissolved carbonate content in major conductive zones. Feng et al. (2019) found that carbonate dissolution/precipitation strongly depends on the physical properties of structural features. According to Feng et al. (2019), the better the fracture interconnection (in direct relation with the fracture frequency/spacing/density) or the larger the aperture, the higher the degree of carbonate dissolution. This would indicate increased carbonate precipitation in loosely fractured rock (carbonate sink) and increased carbonate dissolution in densely fractured rock (carbonate source).[42] However, it further has to be noted that the effect also could be connected to an 'initial' high carbonate content in the surface water, which is better preserved in low developed groundwater and diminished in mature groundwater. The fluoride source productivity seems to be higher in the northwestern tunnel part (elevated fluoride concentrations measured), where the exact source or process connected to the fluoride concentration is unknown. The variation in the fluoride source productivity might lie in a changing biotite or apatite occurrence (however, this was not reported by Hafner (1958)).

6.1.5 Water Types and End-Member Identification

The obtained End-members of each cluster are differing from each other mainly due to their i) surface source, ii) mineralisation degree and iii) local geochemical overprints.

The first end-member specific characteristic concerns the isotopic composition, what refers to end-member specific surface sources. The isotopic composition of EM1 suggests a highly isotopic enriched surface source, such as expected on the low-elevated down-slopes of the northern Bedertto Valley flank. EM2 on the other hand reflects an other extreme of high-elevated depleted surface source, such as estimated for waters infiltrating at glaciated areas above the northern tunnel (in-

[42]Note that since the alkalinity was not measured for surface waters 'initial' carbonate imprints are not known, what adds an uncertainty to the interpretation of the carbonate evolution along the tunnel.

fluenced by glacier melt water contributions). EM3 defines as well rather depleted surface water source, influenced by high-altitude precipitation (similar to the expected isotopic composition near the northern Rotondo summit flank).

The second property of the different end-members concerns the mineralisation degree, supported by the conservative species SO_4^{2-}, Ca^{2+}, Cl^- and to a lower extent Na^+ (linear relationship between computed and measured EM1 and EM2 concentrations). The mineralisation degree mainly decouples EM3 (highly mineralised) from EM1 and EM2 (low mineralised). Making the link between the mineralisation degree and residence times (as discussed in section 6.1.4), it is believed that EM3 is a source of more mature and older water exhibiting a high residence time, whereas EM1 and EM2 are contributing groundwater of lower residence times to the sampling sites. SO_4^{2-}, Ca^{2+} and Na^+ thus are not exhibiting a mixing process (like suggested by Scheiber et al. (2020), see section 5.1.5), but a site wide constant productive WRI's, as discussed in section 6.1.4.

Local geochemical reactions is the third process observed to largely influence the individual end-members. EM1 and EM2 overprints the fluids with an increased carbonate content by i) secondary carbonate dissolution in highly conductive zones and ii) primary carbonate sources in the Tremola-series (see section 2.3.1). EM 3 on the other hand is understood as carbonate sink, as it supports precipitation in low-aperture fractures (section 6.1.4). EM2 furthermore contributes a higher fluoride content in the groundwater, possibly by an increased mineralogical occurrence of biotite or apatite present in EM2 (section 6.1.4). The slightly proportionally increased sodium content provided by EM2 is likely due to an increase in albite content from the margin of the granite body (section 2.3.1). The sodium excess obtained for EM3 indicates that EM3 is influenced by an additional sodium source, which is rather locally constrained. Such a source the Na-rich mica gneisses abundant in the Prato-series.

The mixing ratio evolution showed that EM1 and EM2 both are present in C1 and C2, where EM1 is the dominant part in C1 and EM2 is the dominant part in C2. This observation is likely caused by the fact that EM1 and EM2 share some important characteristics (low mineralisation degree and carbonate source), which are contributing both to C1 and C2. The deviation in EM1 and EM2 evolution pattern thus are caused by the different fluoride and sodium release into the groundwater.

6.2 Mixing during Hydraulic Stimulation

Long-term shifts towards a more depleted isotopic composition are indicated in the lower part of the monitoring borehole CB2, what could indicate mixing between these two end-members. However, there is a high degree of uncertainty regarding these results: i) the data base of the CB2 monitoring is with two to four isotopic measurements weak (what complicates outlier detection), ii) the conservative tracer performance is questionable, since the contrast between the expected end-members is low (see Appendix Q), iii) the isotopic mixing ratio would indicate an implausibly high ($> 50\%$) contribution of the injection fluid to the CB2 formation water. It is thus likely that i) there was no signal and the shifts are due to (random) temporal variability in the data, what is

supported by the fact that the observed shifts (max. encountered shift for $\delta^{18}O = 0.14‰$ and for δD: 1.23‰) are comparable to the maximum observed (random) temporal variability (expressed by the standard deviation) in the BULGG groundwater ($\delta^{18}O$: $\sigma_{max} = 0.4‰$/ $\sigma_{max} = 1.12‰$) or ii) there was a signal, but the tracer contrast between the mixed compounds was too minor and thus were diminished by the (random) temporal variability.

In the TM 1993 fracture the conservative tracers ($\delta^{18}O/\delta D$) did not show any clear trend during the sampling year. At this location are the same uncertainties connected as observed in CB2, of having a very low contrast tracer, where (random) temporal variability would possibly exceed the signal. However, a clear dilution signal was indicated by the EC during few months after both stimulation campaigns, including a recovery in between towards the EC-baseline of the TM 1993 fracture. The EC however was excluded as suitable tracer, since the major ions generally do not behave conservatively at BULGG conditions (except chloride). This adds an uncertainty to the outcome, especially to the reliability of the calculated mixing ratios.

During the short-term monitoring of the ST1 (interval 1 and 2), while low mineralised water was injected in ST2, a clear dilution signal of all tracer species could be obtained. Together with the observed flow rate and down hole pressure increase, the (slightly delayed) hydrochemical signal is suggesting mixing of formation with injection water in the monitored borehole ST1. Assuming a binary mixing process between the injection and ST1 formation water, the corresponding obtained maximum mixing ratios would be between 6.6% and 8.3% (indicated by the calcium, sulfate and EC evolution). The mixing ratios obtained by the sulfate and calcium measurements correspond to a timepoint shortly before the mixing peak (measured by the EC logger) and thus would likely underestimate the injection fluid contribution. Note that using the non-conservative EC and ions as tracer is even in short-term monitoring experiments link to an uncertainty. Minor interactions (of biological or chemical nature) could alter the ion composition or concentration, what especially adds an uncertainty to the calculated mixing ratios.

The stable isotopes also show a clear signal during the obtained EC dilution curve. However, the conservative stable water isotope tracer sampled during the dilution signal would clearly be towards an unknown source providing an enriched isotopic composition and not towards the isotopic depleted injection water as expected. This results could imply either that: i) the second end-member was assumed incorrectly, ii) additional end-members were involved exhibiting a more complex mixing process, or ii) the isotopes behave not conservative. The fact that the mixing line deviates in its slope with respect to the LMWL (and thus all groundwater samples collected), could indicate the influence of water-rock interactions and thus a non-conservative behaviour of the stable isotopes. However, such a non-conservative behaviour of the stable water isotopes has only be observed in very old groundwater (section 6.1.1), which would not be expected in the rather young BULGG groundwater (section 2.4.3).

6.3 Measurement Uncertainties

Measurement uncertainties related to the data set compiled in the context of this thesis are mainly connected to i) inconsistencies between laboratory and field measurements, ii) unreliable results of the instruments used, iii) the low ionic BULGG groundwater and iv) laboratory activities during the sampling year.

i) The comparison of EC and pH measurements conducted in the field and the laboratory showed large inconsistencies.
The EC measurements conducted in the field and lab show a linear relationship (figure 49, Appendix T), however the laboratory measurements are consistently lower than the field measurements. Such a effect could be caused by degassing/precipitation or bacterial interference during the storage time. Acidifying samples could reduce such effects, however, samples of low pH (<2 when acidified) can not be analysed by the IC instrument used.
The lab and field pH measurements show substantial differences (figure 48, Appendix T). Appelo & Postma (2004) report similar observations in the field/lab pH differences. Appelo & Postma (2004) consider that this change in pH could be caused by a readjustment of pH due to the absence of the hydrostatic pressure and the anoxic condition as the water has experienced in the underground. In addition, changes in water chemistry (degassing/precipitation) can be expected to cause a pH shift within a short period of time (Tikhomirov, 2016).

ii) Uncertainties connected to the instruments used were mainly observed with regard to the multi-parameter EXTECH (pH, T, EC, TDS) and the Volcraft (ORP) field probe, as well as the Picarro L2130-I (stable isotopes).

Inconsistencies in the pH measurements were observed when the pH sensor calibration function of the EXTECH field probe broke in March 2021. This circumstance resulted in very high pH readings of up to 13 pH units, which led to the exclusion of these pH measurements from the analysis.

The pH (EXTECH-probe) and ORP (Volcraft) probe showed in general inconsistencies between repeated measuremets.

Another inconsistency has been observed in the stable water isotopes measurements of samples taken during the hydraulic stimulation conducted in March 2021 from ST1 int 1+2. A rerun of the entire batch has been done, since the first measurement did not show any meaningful results. For the second run the injection volume was increased in the instrument setting, what lead to more consistent results. Occasionally analysed control duplicates of samples showed always very consistent results.

iii) A high uncertainty is connected hydrochemical measurements taken for very low mineralised BULGG groundwater/surface water. Such water has in general very low ionic strength, what complicated especially the determination of ionic concentrations and pH.

The uncertainties in ion concentrations of very low mineralized water are related to the fact that IC accuracy decreases when measuring low concentrations because concentrations near the detection limit are misdetected (section 4.3.2). This is evident when comparing the charge balance error (CBE) with the estimated EC in the BULGG groundwaters. This comparison showed an exponential shift of CBE away from 0% (anion-cation balance) the lower the corresponding EC values.

The uncertainty of the pH measurements in low ionic waters possibly is associated to the liquid junction of the reference electrode, where this potential gets larger in waters of low ionic strength (large difference in ionic strength between the electrode electrolyte and the low mineralised groundwater) as described by (Davison & Woof (1985); Liu et al. (2020)).

iv) The uncertainties linked to laboratory activities have mainly been observed in borehole samples and potentially at fractures close to the laboratory (e.g. at TM 1993). Hydrochemical baseline estimations of borehole fluids and close by fracture fluids must therefore be treated with caution, as activities at the BULGG laboratory (even prior hydraulic stimulation works) during the sampling period could have affected various hydrochemical parameters of individual samples. One example are the samples from ST1 interval 1+2 taken during the hydraulic stimulation work (begin of May 21), where a heat test increased the measured temperatures by some degrees (1-2 °C). Another example is the grouting of monitoring boreholes during the sampling year, which could especially interfere with the pH, the calcium and carbonate concentrations.

It was further observed that initial borehole samples immediately collected after opening a borehole (closed over few weeks) showed completely different chemical fingerprints. Such an observation was made at the ST2 borehole (closed in Dec 20), which was sampled in January 2021 and in ST1 interval 1+2 in the beginning of March 21 (which was closed for a few weeks). The initial water sample were both significantly lower mineralised as expected from the borehole waters (about 4 times lower) and recovered within several hours towards the expected formation water baseline (recovery phase). Such a behaviour might be connected to some laboratory activities. A further water quality shift was observed in CB2 (permanent packed monitoring borehole), where initial fluid samples from the CB2 intervals smelled intensely of sulfur accompanied by a low pH (~6), what indicates microbial activities in the packer tubes. This effect diminished within about an hour before stabilizing at the formation water composition.

6.4 Outlook

The findings of this study showed that natural hydrochemical variability in an Alpine massif can be used as tool to assess injection-induced mixing mechanisms within cross-hole distances in stimulated reservoirs in underground rock laboratories. Comparing the results with the findings from the Grimsel ISC experiment, it can be seen that the observed mixed signals strongly depend on the

experimental conditions. In a series of shallow (0.5 km depth) hydraulic fracturing campaigns (creating mode I fractures), coseismic spikes in helium and argon concentrations measured in a nearby tunnel matched the onset of strain responses, suggesting either mixing with old pore water or radiogenic helium and argon release accumulated between the mineral grains (Roques et al., 2020). Another study at Grimsel presented in Stillings et al. (2020) found that seismic events correlate with a short-lived decrease in groundwater pH between 1 - 3.5 units due to production of surface silanols and silica radicals from rock surfaces after hydraulic fracturing. However, these observed 'hydromechanical' mechanisms are rather complex and these studies could not validate pure 'hydraulic injection-induced' mixing in such reservoirs. The study presented here however showed that mixing is most likely the dominant process to explain water quality changes during hydraulic injection in greater depths and larger monitoring scales (>60m cross-hole distance). The observed mixing mechanisms (based on various water quality parameters) between large distant production wells in comparable EGS depth thus provide a better insight on injection-induced mixing in such reservoirs.

However, certain additional information and measurements would substantially increase the knowledge of the fluids hydrochemistry (and related fluid source, pathways and subground WRI reactions), as well as mixing processes in such systems.

One essential example to better connect the BULGG groundwater to surface water sources would be a more comprehensive and repeated surface water surveys. Especially interesting would be the isotopic composition of the glaciers present above the northwestern tunnel section, including primarily the melt water of the Geren and Wittenwasseren glaciers to be able to better define this surface end-member. Apart from glacier samples, a high resolution of the isotopic composition of the precipitation could ease the evaluation of direct groundwater recharge and validate the OIPC estimation. A weather station and precipitation collectors thus could improve the monitoring. A further crucial measurement would tackle the age of the groundwater. The relative ages (residences times) could be roughly estimated, however, based on the data collected in the context of this thesis, it is not possible to infer water ages. To quantify the residence times, the waters must be dated. In the context of groundwater encountered in the Rotondo granite, an age dating method detecting rather young groundwater is suggested, like $^{3}H/^{3}He$ dating. $^{3}H/^{3}He$ age dating is based on high-resolution noble gas measurements, and is a common method to determine the age of waters younger than 50 years (Schlosser et al. (1988);Kipfer et al. (2002)).[43] To be able to better define the geochemical sources, trace elements or stable isotopes (e.g. S-Isotopes) could further reveal mineral origins, reactions or indicate biochemical processes potentially interfering with the hydrochemistry at BULGG.

Mixing processes exceeding the (random) natural variability at BULGG could be better detected with an increased sampling frequency. Continues measurements of tracer species would further ensure a more accurate detection of mixing signals. Additional artificial tracers also could be added to the injection fluid to compare the outcomes with the natural tracers and thus estimate the potential water-rock interactions occurring.

[43] It must however be noted that the northwestern tunnel section (close to the Furka Basetunnel) is likely considerably influenced by glaicer melt water, what could interfere with the actual age of entering the confined aquifer.

7 Conclusion

The tunnel inflow fluids in the 5 kilometer long Bedretto tunnel in the Gotthard Massif shows high spatial variability in its hydrochemistry. The results have shown, that especially the temperature (T), the electric conductivity (EC), EC-correlating dissolved ions (sulfate, calcium, chloride and sodium), carbonate and fluoride concentration, as well as the stable water isotopes contribute to hydrochemical variations and thus different water types in the BULGG groundwaters.

Stable water isotopes revealed generally a meteoric origin under present-day climatic conditions of the natural tunnel inflows encountered along the Bedretto tunnel, supported by a temperature and electric conductivity depression along very conductive zones (preferential path ways along brittle-ductile fault zones). The D-excess revealed a Mediterranean vapor source, possibly enhanced by a reduced subcloud evaporation due to high elevations, as well as potentially higher winter vapor contribution towards the groundwater body. D-excess deviations could be observed in northwestern part of the tunnel, likely caused by a sub-modern vapor source stored in present glaciers above this tunnel section.

The driving force causing a spatial isotopic variability in the BULGG groundwater is understood to be caused by an altitude-effect, preserved in the underground by very local recharge patterns, (sub-)vertical pathways and reduced lateral mixing along the tunnel. Apart from isotopic deviations by glacier melt waters indicated by the d-excess, further anomalies (deviations from pure direct precipitation influence) could be encountered in the southeastern tunnel section. This section is (apart from the altitude-effect) likely influenced by streams, deporting more depleted water from higher elevations towards the groundwater body.

Fluid-fluid interactions (FFI) like mixing is, as mentioned above, not expected parallel to the tunnel. However, enhanced vertical fluid homogenisation is expected, as seasonal trends are almost completely diminished. Thermal indications of seasonal patterns are suspected in very conductive features with small overburden.

Water-rock interactions (WRI) are believed to cause the highest ionic variability at BULGG. This is also supported by a very low 'initial' mineralisation degree of the surface water bodies. The mineralisation degree (expressed in the EC) in the Rotondo granite is mainly defined by sulfate, calcium, sodium, chloride, carbonate and fluoride. It is suspected that sulfate, calcium, sodium and chloride are sourcing from a water-rock interactions with site-wide constantly productive geochemical sources, as these species significantly correlate with each other. Taking into account that chloride exhibits (most likely) a conservative (non-reactive) behaviour, it can further be assumed that these ions qualitatively indicate the relative residence times of the groundwater to a great extent. This assumption is supported by the clear relationship between the concentration of ions and the fracture network interconnection degree of tunnel sections (indicated by cumulative tunnel inflow measurements and fracture spacing). Mainly fluoride and carbonate are believed to originate from more locally productive geochemical sources. The carbonate concentration is believed to be linked to structural properties in the taken pathways, where aperture and fracture network

interconnections influence its dissolution/precipitation behaviour. The reason for different fluoride contributions along the tunnel is unclear. It might indicate mineralogical differences in the Rotondo granite, regarding potential F-sources like biotite or apatite.

Addressing water types at BULGG and their differences due to the contrasting spatial influence of hydrochemical end-members is based on the Cluster (HCA, k-means) and EM analysis (MIX code). Cluster analysis proposes three main water types along the Bedretto tunnel, spatially differentiating between waters in the southeastern tunnel part from i) the highly conductive structural feature and locations close to the Ronco portal (C1) and ii) low-conductive zones /BULGG boreholes (C3), as well as iii) waters originating from the densely fractured wet northern tunnel section (C2). Hydrochemical end-members (each dominant in a different water type (cluster)), were identified to be mainly influenced by the following characteristics:

- EM1 : Elevated carbonate concentration, depleted mineralisation, isotopic enriched (EM influencing mainly C1),
- EM2 : Elevated fluoride, sodium and carbonate concentration and low mineralisation degree + a depleted isotopic composition (EM influencing mainly C2)
- EM3 : High mineralisation degree, low carbonate concentration (EM influencing mostly C3)

These characteristics were interpreted as follows:

- EM1 : Low-elevation surface source of young age and local geochemical carbonate source.
- EM2 : Glacier-influenced, high-elevation surface source of young age and local geochemical source for fluoride, cabronate and sodium.
- EM3 : High-elevation surface source of more elevated age and local geochemical sink for carbonate.

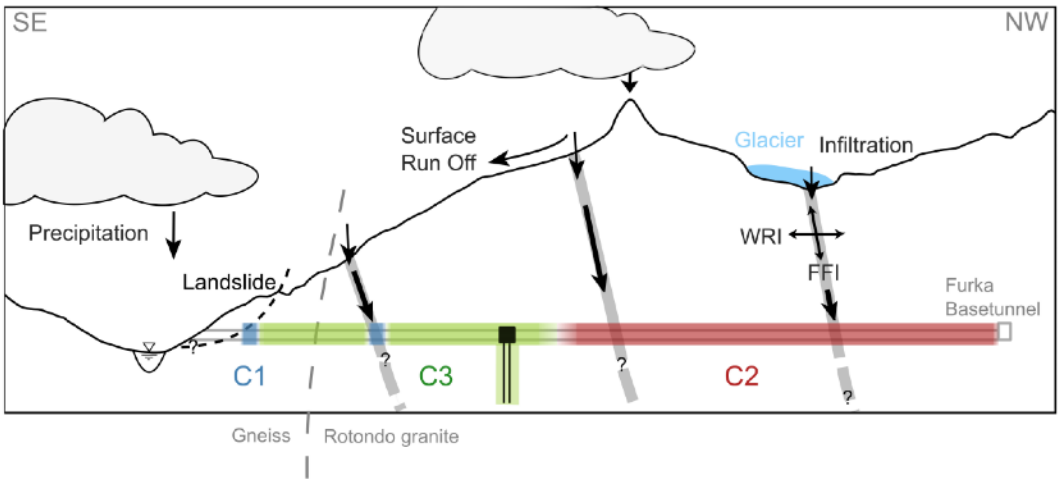

Figure 26: Three water types along the Bedretto tunnel, as well as the interpreted water sources, preferential pathways and leading processes. WRI = Water-Rock Interactions. FFI = Fluid-Fluid Interactions.

No clear result could be obtained validating long-term mixing processes in the immediate vicinity of the stimulated reservoir by a conservative tracer caused by the hydraulic stimulation campaigns at BULGG. However, the analysis was connected to significant uncertainties, likely mainly linked to an insufficient tracer performance concerning a lack of contrast between the mixed end-members. A signal would thus be diminished by the natural (random) variability. It is concluded that long-term mixing processes could not be adequately monitored. A short-term cross-borehole monitoring experiment during hydraulic stimulation injections showed a distinct mixing signal (66 meter cross-hole distance between the injection and the monitored borehole). The signal was indicated by a depression in the ion content and an enrichment of the isotopic composition. The latter contradicts the hydrochemical properties of the depleted injection water, which was expected as the second compound in a binary mixing process. A meaningful potential second isotopic end-member in the system (assuming binary mixing) could not be found, leading to the assumption that the observed mixing process is more complex and potentially even multiple end-members got involved.

8 Acknowledgements

I would first like to thank Dr. Bernard Brixel for his supervision and dedicated support. Further thanks go to my co-supervisor, Prof. Dr. Cara Magnabosco, who organized crucial administrative procedures and contributed invaluable feedbacks. I would also like to thank Andrew Acciardo of the Geobiology Group for his inputs and harmonious collaboration in the field.
In addition, I would like to acknowledge the Engineering Geology Group and the Biogeoscience Group, whose labs I could use and who shared data with me. Special thanks go to Dr. Fanny Leuenberger and Daniel Montluçon, who introduced me to the laboratory workflow and relevant literature. Additionally, I would like to thank the BULGG team, for letting me use the facilities and for the support in my field works. Ultimately, I also want to thank the Geo-energy Swiss team, for sharing data and collecting samples.

9 References

Appelo, C. A. J., & Postma, D. (2004). *Geochemistry, groundwater and pollution.* CRC press.

Arthur, D., & Vassilvitskii, S. (2006). *k-means++: The advantages of careful seeding* (Tech. Rep.). Stanford.

Back, W., & Hanshaw, B. B. (1965). Chemical geohydrology. In *Advances in hydroscience* (Vol. 2, pp. 49–109). Elsevier.

Barton, C. A., Zoback, M. D., & Moos, D. (1995). Fluid flow along potentially active faults in crystalline rock. *Geology*, *23*(8), 683–686.

Basu, A. (2008, January). *Alkalinity (as of caco3 to as of hco3-): Practical guide on unit conversion.* Retrieved January 2021, from `coalgeology.com/alkalinity-as-of-caco3-to-as-of-hco3-practical-guide-on-unit-conversion`

Behrouj-Peely, A., Mohammadi, Z., Scheiber, L., & Vázquez-Suñé, E. (2020). An integrated approach to estimate the mixing ratios in a karst system under different hydrogeological conditions. *Journal of Hydrology: Regional Studies*, *30*, 100693.

Bershaw, J. (2018). Controls on deuterium excess across asia. *Geosciences*, *8*(7), 257.

Borgonie, G., Magnabosco, C., Garcia-Moyano, A., Linage-Alvarez, B., Ojo, A. O., Freese, L. B., ... others (2019). New ecosystems in the deep subsurface follow the flow of water driven by geological activity. *Scientific reports*, *9*(1), 1–16.

Brace, W. F. (1980). Permeability of crystalline and argillaceous rocks. In *International journal of rock mechanics and mining sciences & geomechanics abstracts* (Vol. 17, pp. 241–251).

Brindha, K., & Elango, L. (2011). Fluoride in groundwater: causes, implications and mitigation measures. *Fluoride properties, applications and environmental management*, *1*, 111–136.

Bucher, K., & Stober, I. (2010). Fluids in the upper continental crust. *Geofluids*, *10*(1-2), 241–253.

Bucher, K., Stober, I., & Seelig, U. (2012). Water deep inside the mountains: unique water samples from the gotthard rail base tunnel, switzerland. *Chemical Geology*, *334*, 240–253.

Caine, J. S., & Forster, C. B. (1999). Fault zone architecture and fluid flow: Insights from field data and numerical modeling. *Geophysical Monograph-American Geophysical Union*, *113*, 101–128.

Carrera, J., Vázquez-Suñé, E., Castillo, O., & Sánchez-Vila, X. (2004). A methodology to compute mixing ratios with uncertain end-members. *Water resources research*, *40*(12).

Choi, B.-Y., Yun, S.-T., Yu, S.-Y., Lee, P.-K., Park, S.-S., Chae, G.-T., & Mayer, B. (2005). Hydrochemistry of urban groundwater in seoul, south korea: effects of land-use and pollutant recharge. *Environmental Geology*, *48*(8), 979–990.

Christophersen, N., & Hooper, R. P. (1992). Multivariate analysis of stream water chemical data: The use of principal components analysis for the end-member mixing problem. *Water Resources Research*, *28*(1), 99–107.

Christophersen, N., Neal, C., Hooper, R. P., Vogt, R. D., & Andersen, S. (1990). Modelling streamwater chemistry as a mixture of soilwater end-members—a step towards second-generation acidification models. *Journal of Hydrology*, *116*(1-4), 307–320.

Cloutier, V., Lefebvre, R., Therrien, R., & Savard, M. M. (2008). Multivariate statistical analysis of geochemical data as indicative of the hydrogeochemical evolution of groundwater in a sedimentary rock aquifer system. *Journal of Hydrology*, *353*(3-4), 294–313.

Davis, J. C., & Sampson, R. J. (1986). *Statistics and data analysis in geology* (Vol. 646). Wiley New York.

Davison, W., & Woof, C. (1985). Performance tests for the measurement of ph with glass electrodes in low ionic strength solutions including natural waters. *Analytical Chemistry*, *57*(13), 2567–2570.

Feng, J., Zhang, X., Luo, P., Li, X., & Du, H. (2019). Mineral filling pattern in complex fracture system of carbonate reservoirs: implications from geochemical modeling of water-rock interaction. *Geofluids*, *2019*.

Filzmoser, P., Hron, K., & Reimann, C. (2009). Univariate statistical analysis of environmental (compositional) data: problems and possibilities. *Science of the Total Environment*, *407*(23), 6100–6108.

Freeze, R. A., & Cherry, J. A. (1979). *Groundwater* (Tech. Rep.).

Fritz, S. J. (1994). A survey of charge-balance errors on published analyses of potable ground and surface waters. *Groundwater*, *32*(4), 539–546.

Gat, J. R. (1971). Comments on the stable isotope method in regional groundwater investigations. *Water resources research*, *7*(4), 980–993.

Güler, C., Thyne, G. D., McCray, J. E., & Turner, K. A. (2002). Evaluation of graphical and multivariate statistical methods for classification of water chemistry data. *Hydrogeology journal*, *10*(4), 455–474.

Gurtz, J., Schwarze, R., Peschke, G., & Griinewald, U. (1990). Estimation of the surface, subsurface and groundwater runoff components in mountainous areas. *Hydrology of Mountainous Areas*, 263–280.

Hafner, S. (1958). *Petrographie des südwestlichen gotthardmassivs zwischen st. gotthardpass und nufenenpass* (Unpublished doctoral dissertation). ETH Zurich.

Hooper, R. P. (2003). Diagnostic tools for mixing models of stream water chemistry. *Water Resources Research*, *39*(3).

H. Schassmann, W. K. A. P., W. Balderer. (1984). Beschaffenheit der Tiefengrundwässer in der zentralen Nordschweiz und angrezenden Gebieten. *Technischer (Nagra) Bericht 84-21*.

Jansson, P., Hock, R., & Schneider, T. (2003). The concept of glacier storage: a review. *Journal of Hydrology*, *282*(1-4), 116–129.

Jasechko, S. (2019). Global isotope hydrogeology—review. *Reviews of Geophysics*, *57*(3), 835–965.

Jiang, Y., Guo, H., Jia, Y., Cao, Y., & Hu, C. (2015). Principal component analysis and hierarchical cluster analyses of arsenic groundwater geochemistry in the hetao basin, inner mongolia. *Geochemistry*, *75*(2), 197–205.

Jordan, D. (2019). *Geological characterization of the bedretto underground laboratory for geoenergies* (Unpublished master's thesis). ETH Zurich, Geological Institute.

Jurado, A., Vázquez-Suñé, E., Carrera, J., Tubau, I., & Pujades, E. (2015). Quantifying chemical reactions by using mixing analysis. *Science of The Total Environment*, *502*, 448–456.

Keller, F., & Schneider, T. (1982). Geologie und geotechnik. *Der Furka-Basistunnel: Zur Eröffnung am*, *25*, 512–520.

Kipfer, R., Aeschbach-Hertig, W., Peeters, F., & Stute, M. (2002). Noble gases in lakes and ground waters. *Reviews in mineralogy and geochemistry*, *47*(1), 615–700.

Kloppmann, W., Girard, J.-P., & Négrel, P. (2002). Exotic stable isotope compositions of saline waters and brines from the crystalline basement. *Chemical Geology*, *184*(1-2), 49–70.

Laaksoharju, M., Gascoyne, M., & Gurban, I. (2008). Understanding groundwater chemistry using mixing models. *Applied Geochemistry*, *23*(7), 1921–1940.

Liu, S., Butman, D. E., & Raymond, P. A. (2020). Evaluating co2 calculation error from organic alkalinity and ph measurement error in low ionic strength freshwaters. *Limnology and Oceanography: Methods*, *18*(10), 606–622.

Lützenkirchen, V., & Loew, S. (2011). Late alpine brittle faulting in the rotondo granite (switzerland): deformation mechanisms and fault evolution. *Swiss Journal of Geosciences*, *104*(1), 31–54.

Lützenkirchen, V. H. (2002). *Structural geology and hydrogeology of brittle fault zones in the central and eastern gotthard massif, switzerland* (Unpublished doctoral dissertation). ETH Zurich.

MacQueen, J., et al. (1967). Some methods for classification and analysis of multivariate observations. In *Proceedings of the fifth berkeley symposium on mathematical statistics and probability* (Vol. 1, pp. 281–297).

Manga, M., Beresnev, I., Brodsky, E. E., Elkhoury, J. E., Elsworth, D., Ingebritsen, S. E., ... Wang, C.-Y. (2012). Changes in permeability caused by transient stresses: Field observations, experiments, and mechanisms. *Reviews of Geophysics*, *50*(2).

Maréchal, J.-C., & Etcheverry, D. (2003). The use of 3h and 18o tracers to characterize water inflows in alpine tunnels. *Applied Geochemistry*, *18*(3), 339–351.

Marín Celestino, A. E., Martínez Cruz, D. A., Otazo Sánchez, E. M., Gavi Reyes, F., & Vásquez Soto, D. (2018). Groundwater quality assessment: An improved approach to k-means clustering, principal component analysis and spatial analysis: A case study. *Water*, *10*(4), 437.

Masset, O., & Loew, S. (2010). Hydraulic conductivity distribution in crystalline rocks, derived from inflows to tunnels and galleries in the central alps, switzerland. *Hydrogeology Journal*, *18*(4), 863–891.

Moeck, C., Radny, D., Borer, P., Rothardt, J., Auckenthaler, A., Berg, M., & Schirmer, M. (2016). Multicomponent statistical analysis to identify flow and transport processes in a highly-complex environment. *Journal of Hydrology*, *542*, 437–449.

Moon, J., & Fernandez, G. (2010). Effect of excavation-induced groundwater level drawdown on tunnel inflow in a jointed rock mass. *Engineering Geology*, *110*(3-4), 33–42.

Oberhänsli, R. (1986). Geochemistry of meta-lamprophyres from the central swiss alps. *Schweizerische Mineralogische und Petrographische Mitteilungen*, *66*(3), 315–342.

Ofterdinger, U., Balderer, W., Loew, S., & Renard, P. (2004). Environmental isotopes as indicators for ground water recharge to fractured granite. *Ground water*, *42*(6), 868–879.

Ofterdinger, U., Renard, P., & Loew, S. (2014). Hydraulic subsurface measurements and hydrodynamic modelling as indicators for groundwater flow systems in the rotondo granite, central alps (switzerland). *Hydrological Processes*, *28*(2), 255–278.

Ofterdinger, U. S. (2001). *Ground water flow systems in the rotondo granite, central alps (switzerland)* (Unpublished doctoral dissertation). ETH Zurich.

Pastorelli, S., Marini, L., & Hunziker, J. (2001). Chemistry, isotope values (δd, δ18o, δ34sso4) and temperatures of the water inflows in two gotthard tunnels, swiss alps. *Applied Geochemistry*, *16*(6), 633–649.

Pelizardi, F., Bea, S. A., Carrera, J., & Vives, L. (2017). Identifying geochemical processes using end member mixing analysis to decouple chemical components for mixing ratio calculations. *Journal of Hydrology*, *550*, 144–156.

Picarro. (2012, July). User's manual: Operation, data analysis, maintenance, troubleshooting, l2130-i or l2120-i analyzer and its peripherals [Computer software manual].

Piper, A. M. (1944). *A graphic procedure in the geochemical interpretation of water-analyses.* American Geophysical Union.

Priest, S. D. (1993). The collection and analysis of discontinuity orientation data for engineering design, with examples. In *Rock testing and site characterization* (pp. 167–192). Elsevier.

Roques, C., Weber, U. W., Brixel, B., Krietsch, H., Dutler, N., Brennwald, M. S., ... others (2020). In situ observation of helium and argon release during fluid-pressure-triggered rock deformation. *Scientific reports*, *10*(1), 1–9.

Scheiber, L., Cendón, D., Iverach, C., Hankin, S., Vázquez-Suñé, E., & Kelly, B. (2020). Hydrochemical apportioning of irrigation groundwater sources in an alluvial aquifer. *Science of the Total Environment*, *744*, 140506.

Schlosser, P., Stute, M., Dörr, H., Sonntag, C., & Münnich, K. O. (1988). Tritium/3he dating of shallow groundwater. *Earth and Planetary Science Letters*, *89*(3-4), 353–362.

Schneeberger, R., Mäder, U. K., & Waber, H. N. (2017). Hydrochemical and isotopic (δ2h, δ18o, 3h) characterization of fracture water in crystalline rock (grimsel, switzerland). *Procedia earth and planetary science*, *17*, 738–741.

Schneider, T. (1985). Basistunnel furka—geologische aufnahme des fensters bedretto. *Brig, Furka-Oberalp-Bahn AG*.

Schürch, M., Kozel, R., Schotterer, U., & Tripet, J.-P. (2003). Observation of isotopes in the water cycle—the swiss national network (nisot). *Environmental Geology*, *45*(1), 1–11.

Sergeev, S. A., Meier, M., & Steiger, R. H. (1995). Improving the resolution of single-grain u/pb dating by use of zircon extracted from feldspar: application to the variscan magmatic cycle in the central alps. *Earth and Planetary Science Letters*, *134*(1-2), 37–51.

Singh, H., Singh, D., Singh, S. K., & Shukla, D. (2017). Assessment of river water quality and ecological diversity through multivariate statistical techniques, and earth observation dataset of rivers ghaghara and gandak, india. *International Journal of River Basin Management*, *15*(3), 347–360.

Skelton, A., Liljedahl-Claesson, L., Wästeby, N., Andrén, M., Stockmann, G., Sturkell, E., ... others (2019). Hydrochemical changes before and after earthquakes based on long-term measurements of multiple parameters at two sites in northern iceland—a review. *Journal of Geophysical Research: Solid Earth*, *124*(3), 2702–2720.

Slaymaker, H. O. (1974). Alpine hydrology. *Arctic and alpine environments*, 133–158.

Steck, A., et al. (1976). Albit-oligoklas-mineralgesellschaften der peristeritluecke aus alpinmetamorphen granitgneisen der gotthardmassivs.

Stillings, M., Lunn, R., Pytharouli, S., Shipton, Z., Kinali, M., Lord, R., & Thompson, S. (2020). Microseismic events cause significant ph drops in groundwater. *Geophysical Research Letters*, e2020GL089885.

Taucare, M., Daniele, L., Viguier, B., Vallejos, A., & Arancibia, G. (2020). Groundwater resources and recharge processes in the Western Andean front of Central Chile. *Science of the Total Environment*, *722*, 137824.

Templ, M., Filzmoser, P., & Reimann, C. (2008). Cluster analysis applied to regional geochemical data: problems and possibilities. *Applied Geochemistry*, *23*(8), 2198–2213.

Tikhomirov, V. V. (2016). *Hydrogeochemistry fundamentals and advances, mass transfer and mass transport* (Vol. 2). John Wiley & Sons.

Tomonaga, Y., Marzocchi, R., Pera, S., Pfeifer, H.-R., Kipfer, R., Decrouy, L., & Vennemann, T. (2017). Using noble-gas and stable-isotope data to determine groundwater origin and flow regimes: Application to the ceneri base tunnel (switzerland). *Journal of hydrology*, *545*, 395–409.

Tubau, I., Vàzquez-Suñé, E., Jurado, A., & Carrera, J. (2014). Using emma and mix analysis to assess mixing ratios and to identify hydrochemical reactions in groundwater. *Science of the total environment*, *470*, 1120–1131.

Usman, U. N., Toriman, M. E., Juahir, H., Abdullahi, M. G., Rabiu, A. A., & Isiyaka, H. (2014). Assessment of groundwater quality using multivariate statistical techniques in terengganu. *Science and Technology*, *4*(3), 42–49.

Vázquez-Suñé, E., Carrera, J., Tubau, I., Sánchez-Vila, X., & Soler, A. (2010). An approach to identify urban groundwater recharge. *Hydrology and Earth System Sciences*, *14*(10), 2085–2097.

Vlasek, A. (2018). *Deep structures of large toppling slopes at the bedretto adir (ticino, switzerland).* (Unpublished doctoral dissertation).

Wanner, C., Waber, H. N., & Bucher, K. (2020). Geochemical evidence for regional and long-term topography-driven groundwater flow in an orogenic crystalline basement (aar massif, switzerland). *Journal of hydrology*, *581*, 124374.

Žalik, K. R. (2008). An efficient k-means clustering algorithm. *Pattern Recognition Letters*, *29*(9), 1385–1391.

Zangerl, C., Loew, S., & Eberhardt, E. (2006). Structure, geometry and formation of brittle discontinuities in anisotropic crystalline rocks of the central gotthard massif, switzerland. *Eclogae Geologicae Helvetiae*, *99*(2), 271–290. Retrieved from `https://doi.org/10.1007/s00015-006-1190-0` doi: doi:10.1007/s00015-006-1190-0

Appendices

A - Mineralogical Composition of the Lithologies

Unit	Lithology	Mineralogical composition [%]									
		Qtz	Kfs	Pl (An%)	Msc	Bt	Ep	Carb	Gt	Hbl	Cl
Rg	Granite	25-35	20-40	20-35 (2-7)		5-10					
PS	Mica gneiss	15-90	0-35	3-75 (0-15)	0-45	2-25	0-10	0-10	0-4		
	Biotite schist	10-20		2-5 (20-25)		50-65	10-20	5-10			
	Amphibolite	0-30		0-30 (20-40)		0-40	0-45	0-5	0-25	40-80	
TS	Hbl gneisses	15-50		15-40 (18-27)	0-15	0-15	0-25	0-15		10-40	0-30
	Amphibolites	5-20		18-30 (15-38)		0-5	0-20	0-10		40-70	0-5
	Hbl schist	0-20		0-10		0-5	5-20	0-20	*	40-90	0-5

Table 8: Mineralogical composition of the study area present lithologies according to Hafner (1958) (excl. accessories). Rg = Rotondo granite, PS = Prato series, TS = Tremola series. Qtz = Quartz, Kfs = K-felspar, Pl = Plagioclase, An% = Anorthite proportion, Msc = Muscovite, Bt = Biotite, Ep = Epidote, Carb = Carbonate, Gt = Garnet, Hbl = Hornblende, Cl = Chlorite.
*Strongly variable.

B - Borehole Informations

Table 9: Key data of sampled boreholes at the Bedretto Underground Laboratory. Interval depth = 0 corresponds to the Wellhead (WH). BB = Borehole bottom. TB = Total borehole. All boreholes are drilled inclined, except the horizontal welltec borehole. *Packer installation during hydraulic stimulation in 2020. **Packer installation during hydraulic stimulation in 2021.

Borehole Fluids		
Sample ID	Interval	Interval depth [m]
BdWcb1	TB	0 - 300
BdWcb2-p3	int3	177.24 - 195.24
BdWcb2-p4	int4	166.73 - 175.73
BdWcb2-p5	int5	156.19 - 165.19
BdWcb2-p7	int7	123.94 - 124.94
BdWcb3	TB	0 - 192
BdWmb4	TB	0 - 250
BdWmb5	TB	nan
BdWmb8	TB	nan
BdWsb2.3-p2	int2	31.3 - 33.4
BdWsb2.3-p3/4	int3 and 4	22.5 - 29.8
BdWst1	TB	0 - 399
BdWst1 0-265	WH-int10	0 - 265
BdWst1 265-400	int10-BB	265 - 399
BdWst1-int11*	int11	278 - 288
BdWst1-int14*	int14	311 - 321
BdWst1-int15*	int15	322 - 332
BdWst1-int17*	int17	345 - 355
BdWst1-int1-2**	int1-2	366 - 388
BdWst1-int1-3**	int1-3	347 - 388
BdWst1-int1-6**	int1-6	307 - 388
BdWst1-int4**	int4	337-345
BdWst2	TB	0 - 349
BdWst2 0-200	WH-200	0 - 200
BdWst2 0-344	WH-344	0 - 344
BdWwelltec	TB	nan

C - General Standard Operation (SOP)

The purpose of this SOP is to provide clear guidelines related to the sampling, preservation, transport and storage of fluid samples collected at the Bedretto Underground Lab. This SOP applies to the following parameters:

1. Field parameters (pH, temperature, EC, TDS, ORP)
2. Major ions [Fluoride, Chloride, Nitrite, Bromide, Nitrate, Phosphate, Sulfate, Lithium, Sodium, Ammonium, Potassium, Magnesium, Calcium, Strontium]
3. Stable isotopes [d18O, d2H]

Site Background and Terminology

The sampled area covers the entire tunnel, including Bedretto's underground laboratory (BULGG). The sampled fluid inflow in the tunnel is limited to water-bearing discrete fractures / fault zones and fracture zones.
In the laboratory, water samples are taken from the implemented boreholes, if the boreholes are accessible (no water coverage) and open.

The unique sample ID is structured as follows:

Sample Location	→	"BdT" = Bedretto tunnel; "BdW" = Bedretto well
Sampled Object	→	"frac" = fracture; "ditch" = ditch; "st1" = borehole name
Sample Localization	→	tunnel meter (eg. meter "1993"); borehole interval ("intX")
Sampling Date	→	.yyyymmdd

Example 1: A sample collected on the 20th of August 2020 in the well (W) ST1 in interval 2 would correspond to BdWst1-int2.20200820.
Example 2: A sample collected on the 20th of August 2020 from a naturally seeping fracture intersecting the tunnel (T) at tunnel meter 1993 would correspond to BdTfrac1993.20200820.

Health and Safety Plan

Identify potential risks related:

- Chemicals
- Environment (unstable rock on the tunnel face, radon concentration, slippery conditions, etc)
- Boreholes (high fluid pressure), drilling operations (air compressor)

Sampling Equipment and Materials

Any equipment and materials used to collect, transport and store fluid samples should be cleaned with Milli-Q water.
Basic materials include:

- Calibrated pH/temperature field meter (1x)
- Calibrated EC/TDS/temperature field meter (1x)
- Calibrated ORP field meter (1x)
- Spare batteries for field meters
- 2L, large-diameter bucket (graduated) (1x)
- 100mL measuring cup (3x)
- 100mL sampling bottles (30x)
- Seals for 100mL bottles (35x)
- Caps for 100mL bottles (35x)
- Plastic bags to store samples, e.g. Ziploc bags (about 2L)
- Nitril gloves
- Permanent marker (2x)
- Timer (1x)

Sampling Workflow

The recommended workflow for sampling tunnel inflows is as follows:

1. Identify sampling site
2. Prepare materials and ID of the sampling bottle following the correct terminology
3. Take a photo, including the sampleID
4. Use and disinfect Nitril gloves
5. Rinse bottle, caps and seals with indigenous fluid
6. Fill bottle, ensure to the extent possible that no air is in the bottle once it is sealed and capped.
7. Measure the flow rate.
8. Measure field parameters (pH, temperature, EC, TDS, ORP) and note the time.

Preservation, Transport and Storage

No acid preservation. Store on site only if fridge is available (optimal temperature of 4°C).

D - IC Standards

Cation	Standards	1	2	3	4	5	6
Li^+	[ppm]	0.1	0.3	0.5	1	3	
Na^+	[ppm]	5	10	20	30	40	60
NH_4^+	[ppm]	0.5	1	2	3	5	
K^+	[ppm]	0.1	0.5	2	3	5	
Mg^{2+}	[ppm]	0.5	1	3	4	5	
Ca^{2+}	[ppm]	10	20	40	60	80	120

Table 10: Standards 1 to 6 used for the cation analysis (IC analysis).

Anion	Standards	1	2	3	4	5	6
F^-	[ppm]	1	2	4	6	8	10
Cl^-	[ppm]	2	4	8	10	15	20
NO_2^-	[ppm]	0.5	1	2	3	5	
Br^-	[ppm]	0.5	1	2	3	5	
NO_3-	[ppm]	0.5	1	2	3	5	
PO_4^{3-}	[ppm]	0.5	1	2	3	5	
SO_4^{2-}	[ppm]	10	20	40	80	100	120

Table 11: Standards 1 to 6 used for the anion analysis (IC analysis).

E - Data Distribution of each Parameter

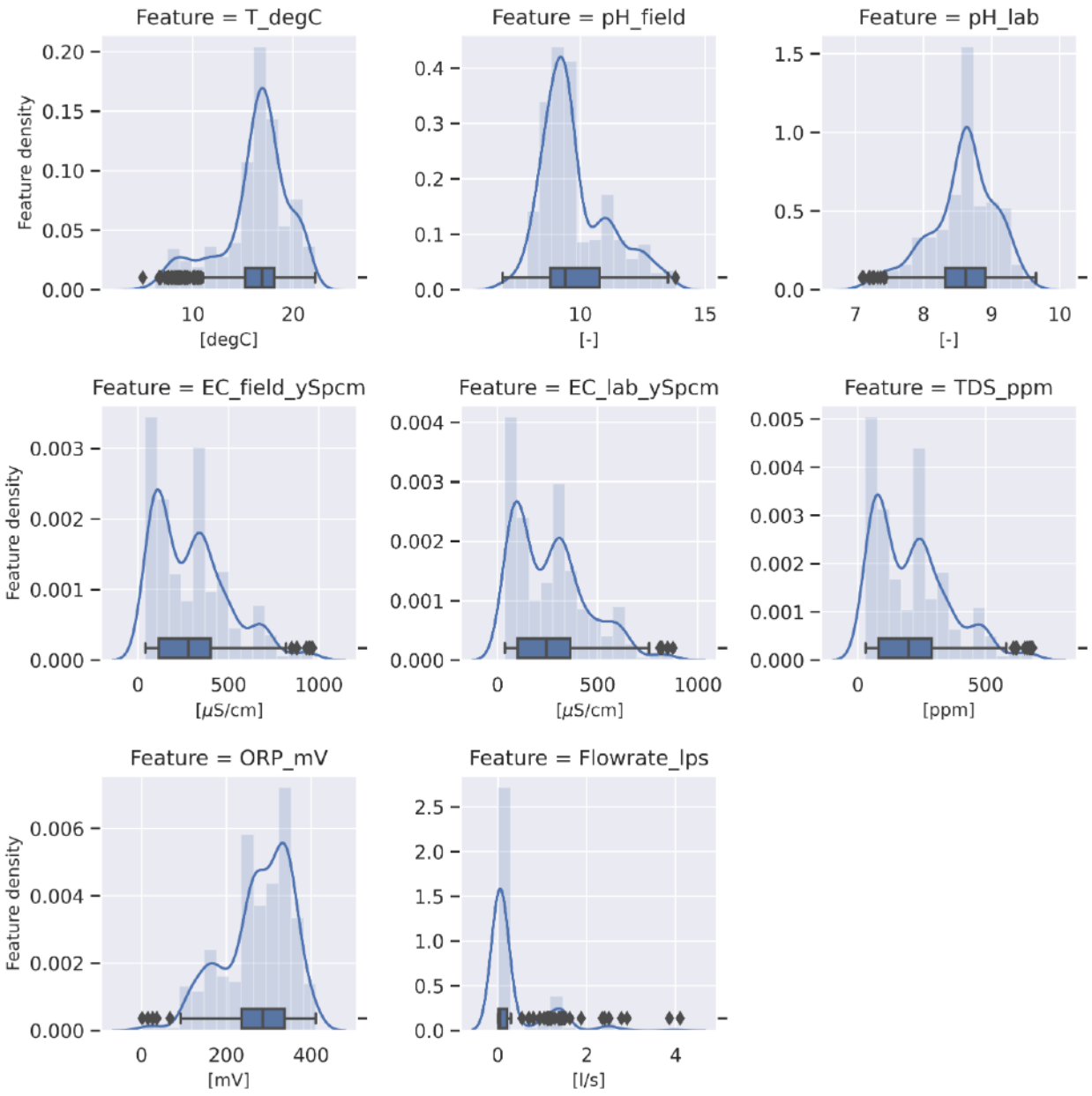

Figure 27: Histograms and box-plots showing the data distribution of standard parameters (including only fracture fluid data).

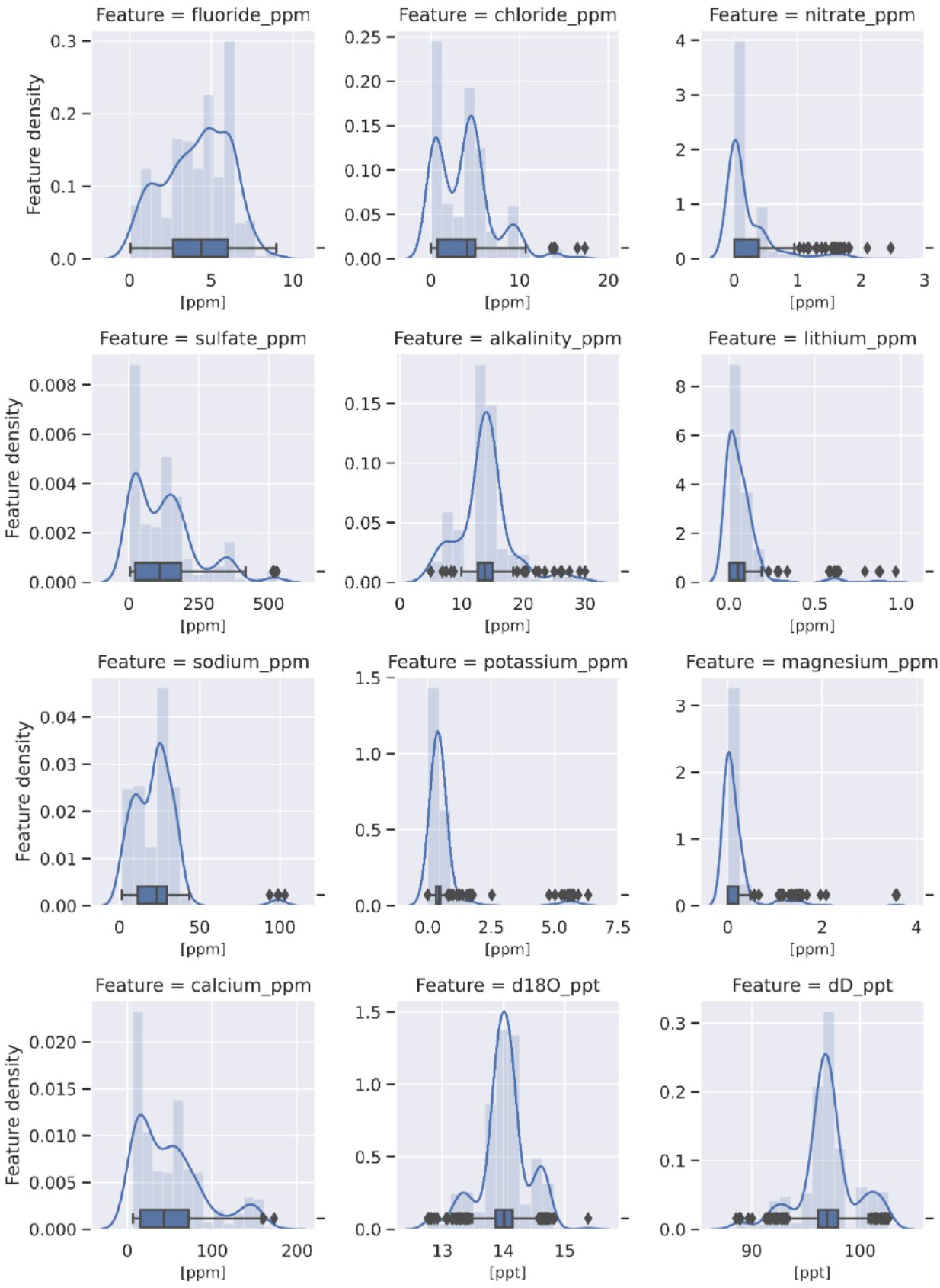

Figure 28: Histograms and box-plots showing the data distribution of the major ions and the stable isotopes (including only fracture fluid data).

F - Principal Component / Cluster Analysis

Table 12: Two statistical tests (Kaiser-Meyer-Olkin (kmo) test/ Bartlett's test of Sphericity) to estimate the suitability to perform PCA on the data set. Both test suggest that the data set is suitable to perform PCA, since the KMO value is higher than 0.6 (thus, the proportion of common variance is small) and the alpha value of the Barlett's test of sphericity is 0, what implies that the correlation matrix is significantly differing from the identity matrix.

KMO and Barlett's Test		
Kaiser-Meyer-Olkin measure of sampling adequacy		0.82
Barlett's test of sphericity	Chi-square	8585.37
	alpha	0.0

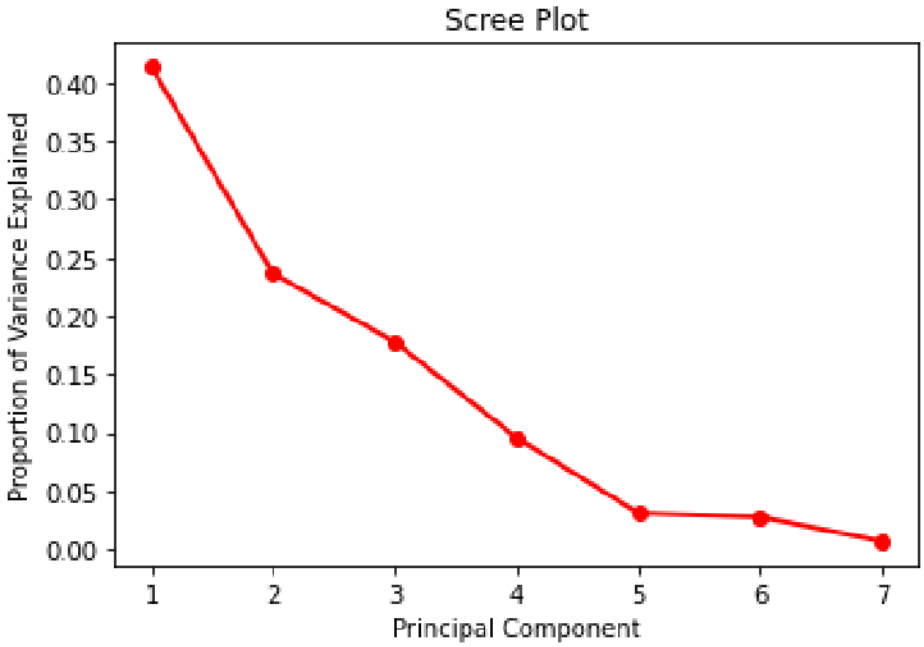

Figure 29: Scree plot showing the inertia with increasing principle component numbers.

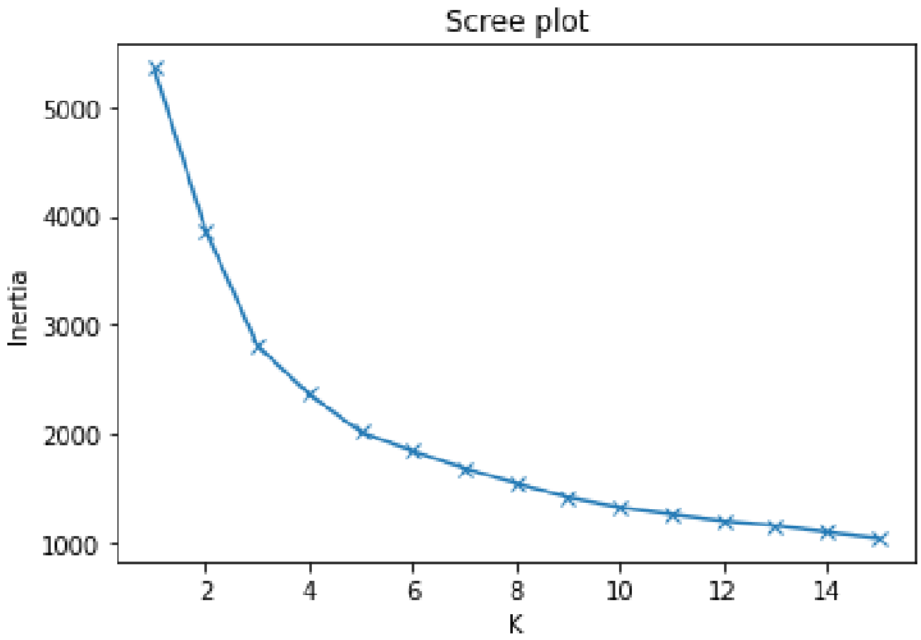

Figure 30: Scree plot showing the inertia with increasing cluster numbers (k).

G - Hydrochemcial Variability per Site

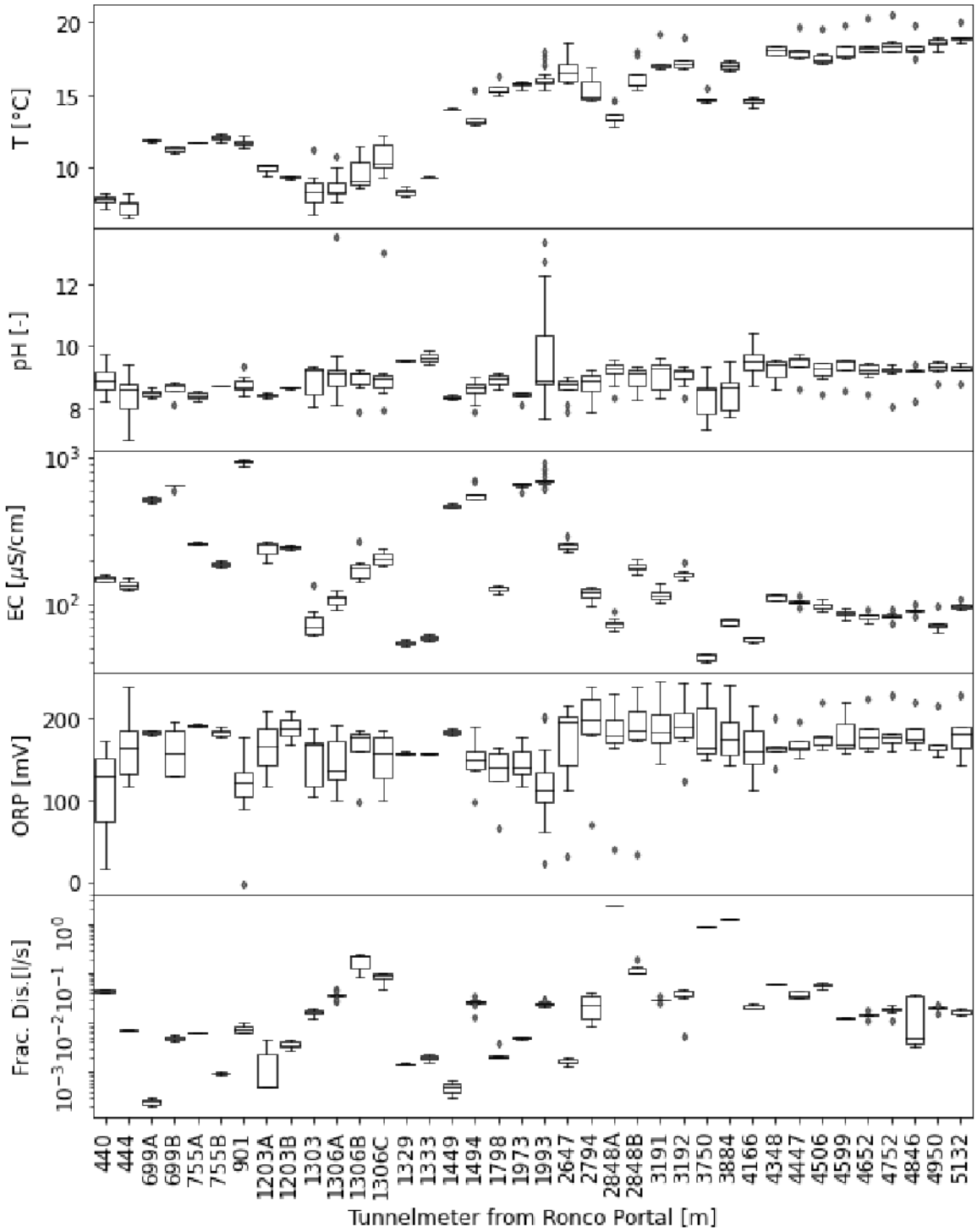

Figure 31: Box-plots of the standard water quality parameters per site, where at least two measurements were taken. The box boundaries represent the 25^{th} (lower line) and 75^{th} (upper line) percentiles. The lower and upper error lines display the 10^{th} and 90^{th} percentiles, respectively. The diamond shaped markers correspond to data points falling outside 10^{th} and 90^{th} percentiles. The line inside the box marks the median.

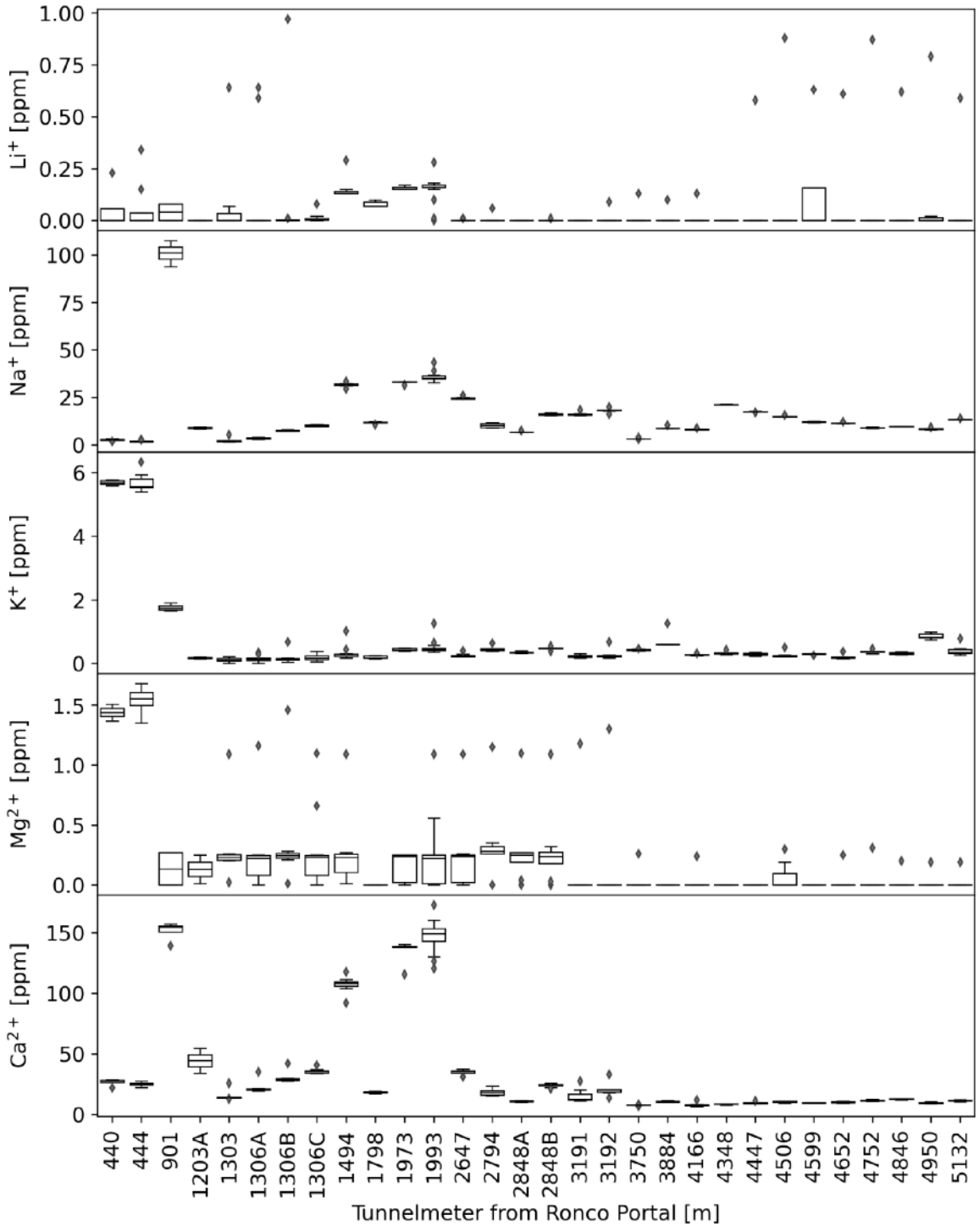

Figure 32: Box-plots of the cation concentrations per site, where at least two measurements were taken. The box boundaries represent the 25^{th} (lower line) and 75^{th} (upper line) percentiles. The lower and upper error lines display the 10^{th} and 90^{th} percentiles, respectively. The diamond shaped markers correspond to data points falling outside 10^{th} and 90^{th} percentiles. The line inside the box marks the median.

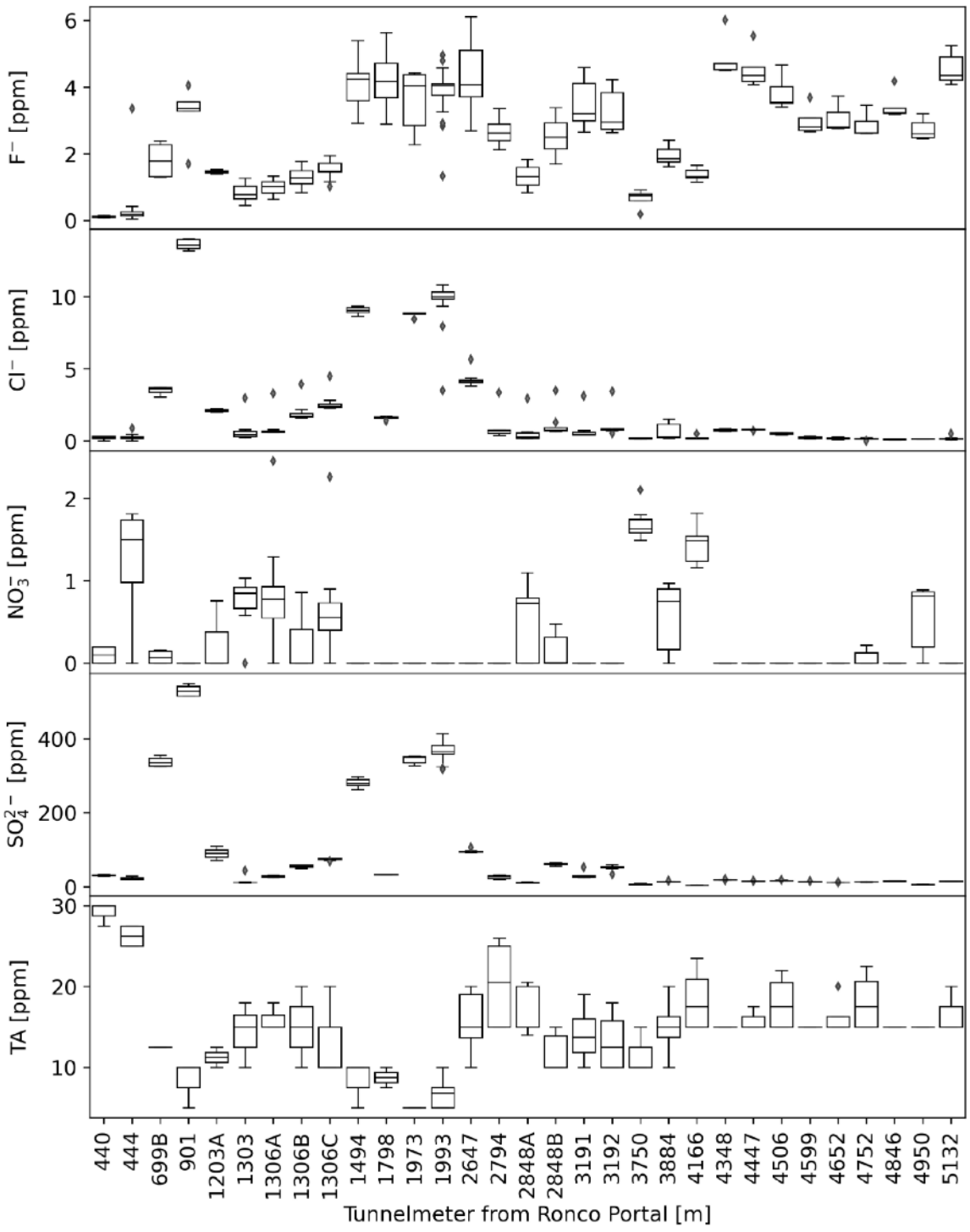

Figure 33: Box-plots of the anion concentrations per site, where at least two measurements were taken. The box boundaries represent the 25^{th} (lower line) and 75^{th} (upper line) percentiles. The lower and upper error lines display the 10^{th} and 90^{th} percentiles, respectively. The diamond shaped markers correspond to data points falling outside 10^{th} and 90^{th} percentiles. The line inside the box marks the median.

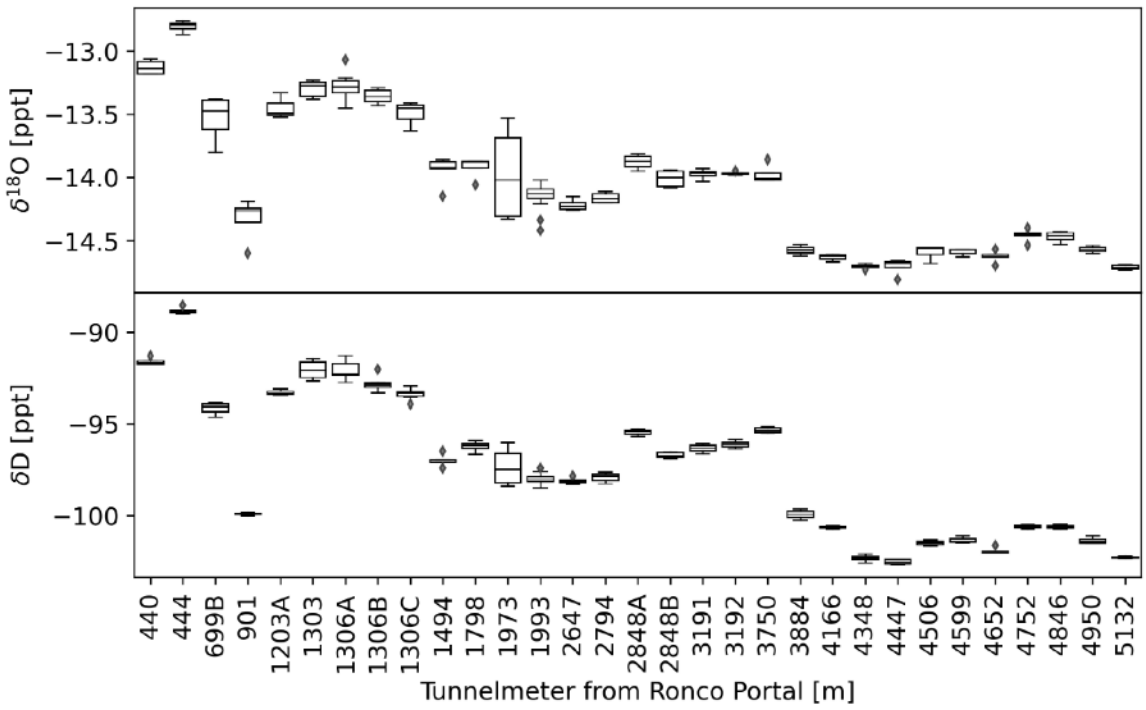

Figure 34: Box-plots of the stable isotopes per site, where at least two measurements were taken. The box boundaries represent the 25^{th} (lower line) and 75^{th} (upper line) percentiles. The lower and upper error lines display the 10^{th} and 90^{th} percentiles, respectively. The diamond shaped markers correspond to data points falling outside 10^{th} and 90^{th} percentiles. The line inside the box marks the median.

H - Pairwise Relationships

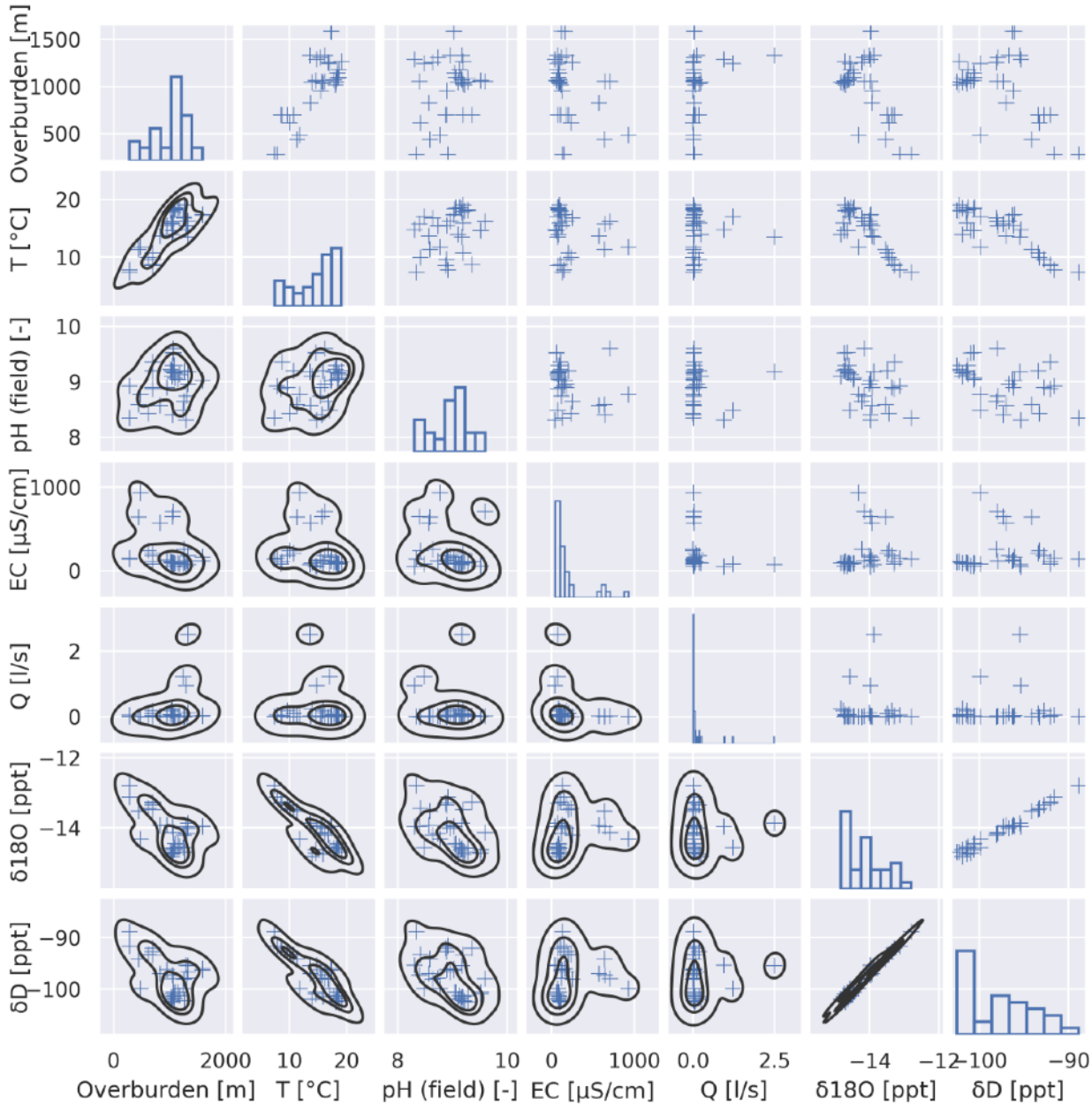

Figure 35: Scatter plots showing the pairwise relationships of the standard water quality parameters and stable water isotopes. The diagonal plots show the univariate distribution of each parameter visualised with a histogram. The black curves show the kernel density estimate.

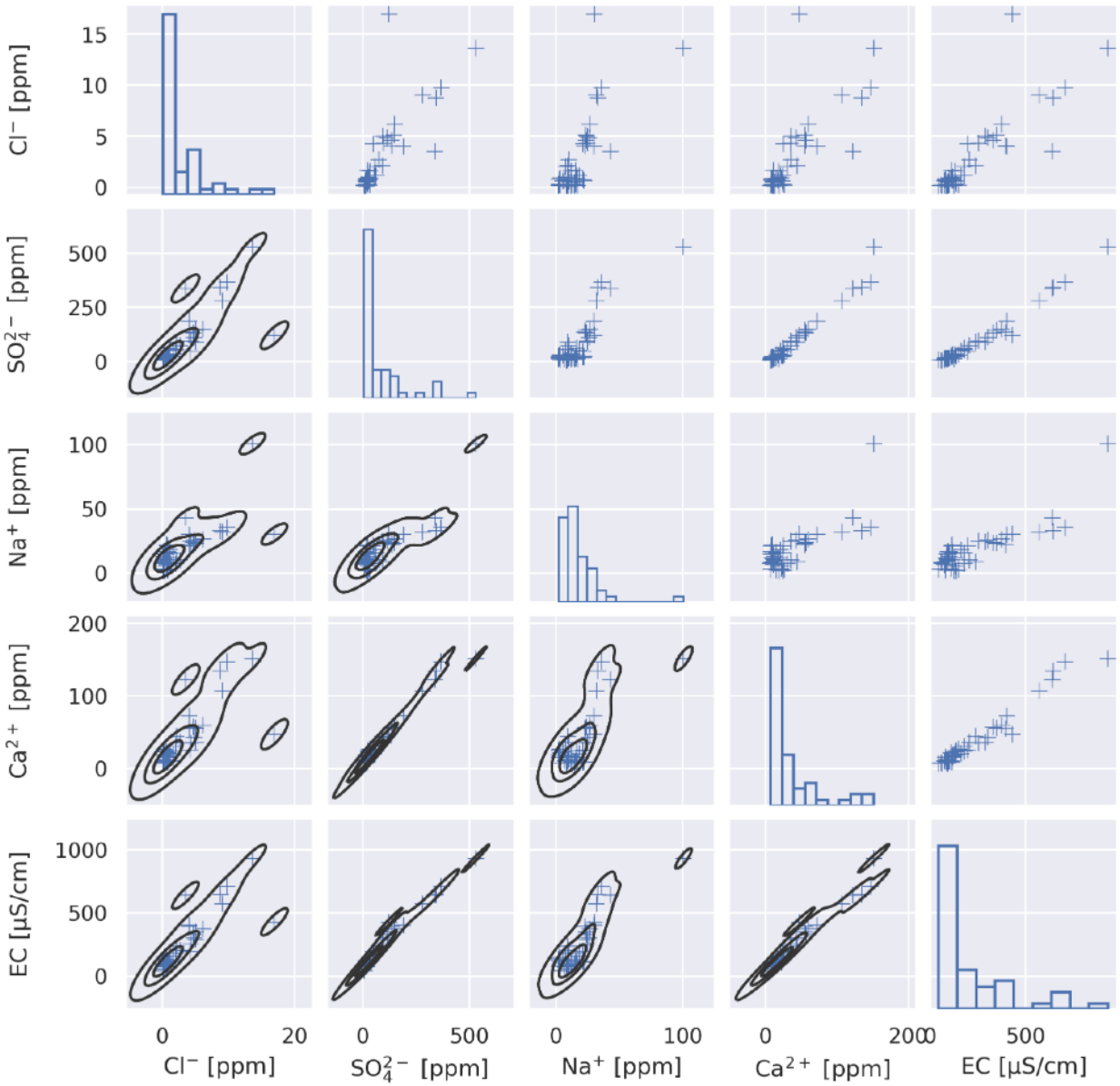

Figure 36: Scatter plots showing the pairwise relationships of EC related ions. The diagonal plots show the univariate distribution of each parameter visualised with a histogram. The black curves show the kernel density estimate.

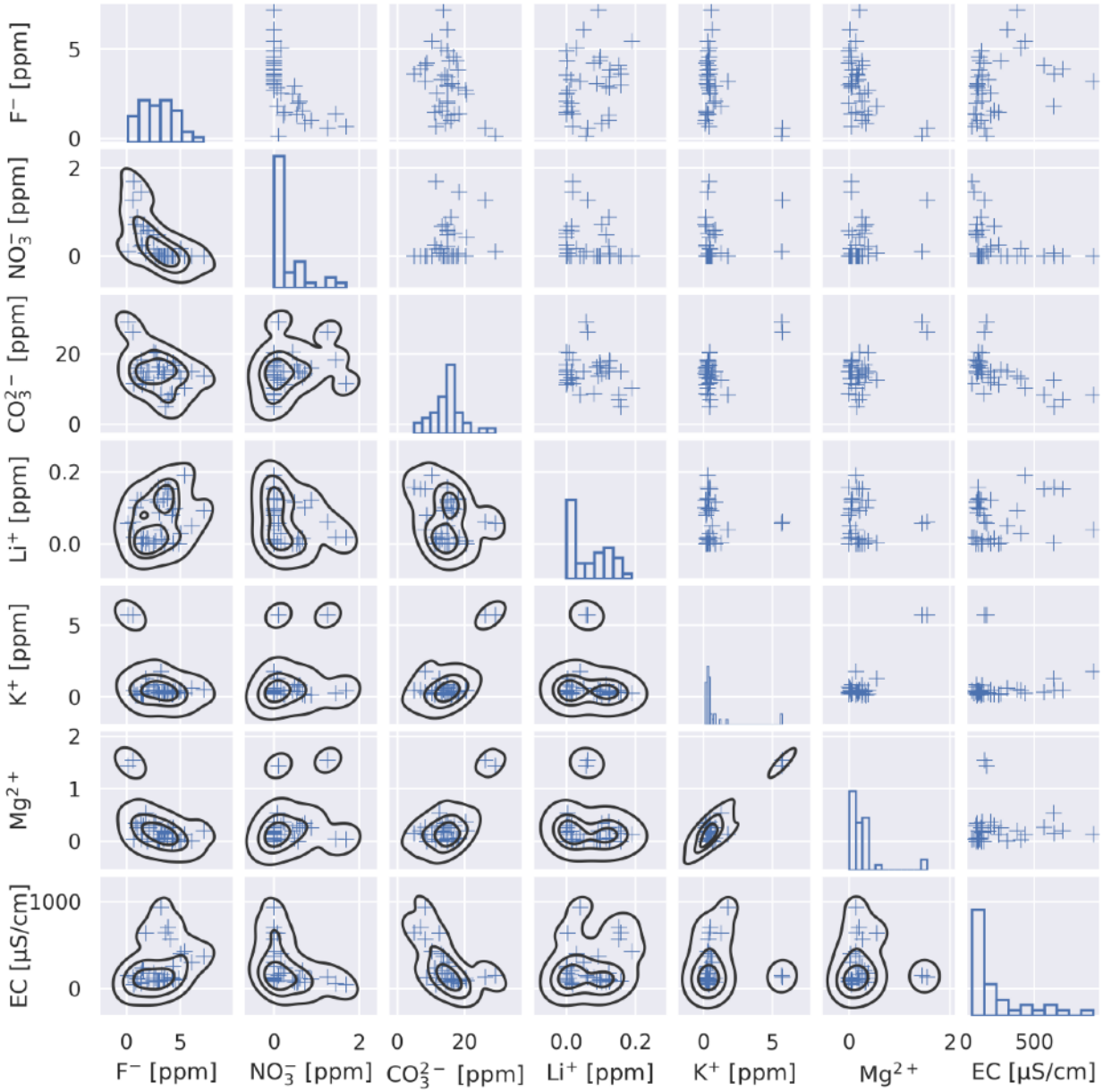

Figure 37: Scatter plots showing the pairwise relationships of the ions which ar not EC related. The diagonal plots show the univariate distribution of each parameter visualised with a histogram. The black curves show the kernel density estimate. A significant linear relationship can be observed between i) the stable water isotopes, ii) the temperature and overburden, iii), the temperature and the stable water isotopes.

I - Correlation of Chemical Parameters

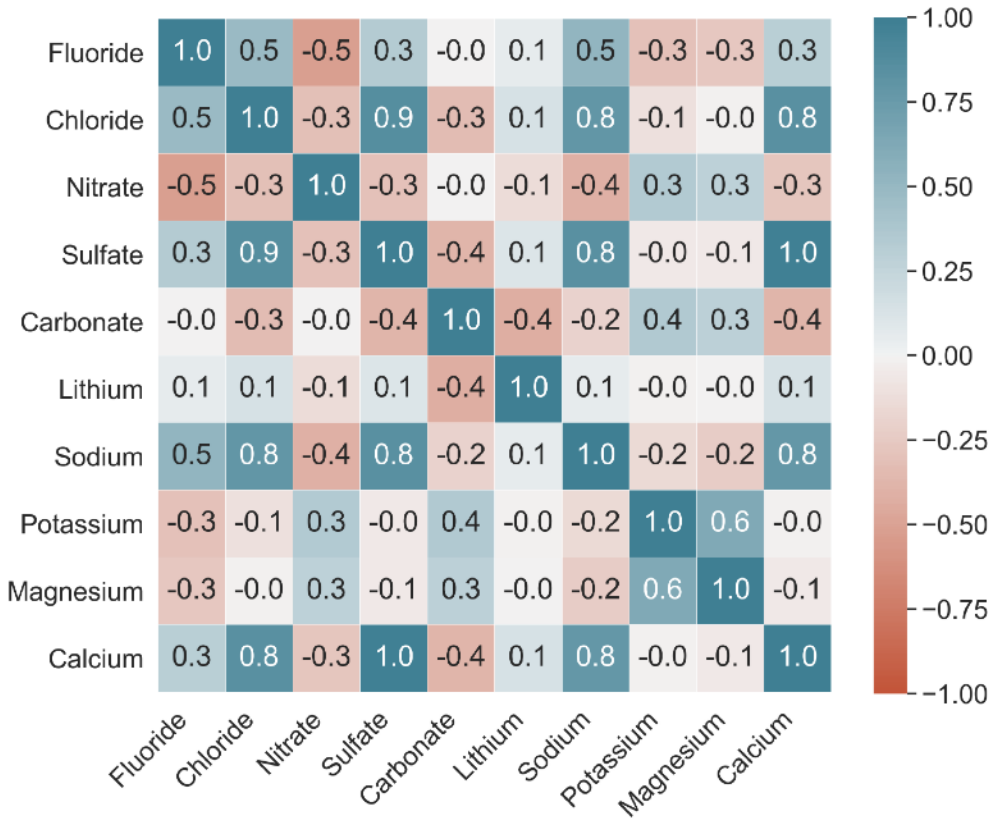

Figure 38: Heatmap showing the correlation between the major ions measured from BULGG groundwaters (including the borehole and fracture data).

J - Isotopic Composition of the BULGG/ GTS Grondwater and Surface Water

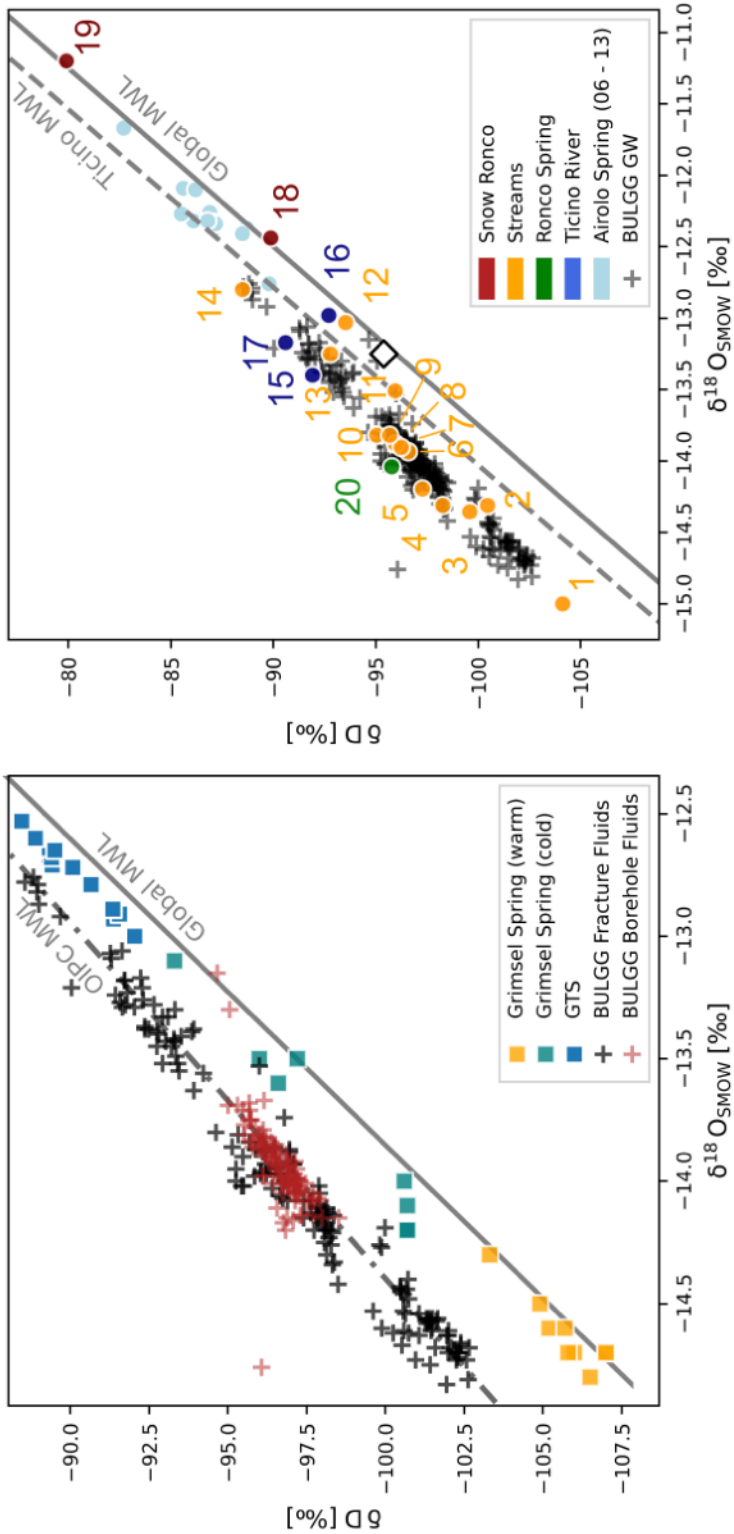

Figure 39: Left: δD versus δ^{18}O values of BULGG, warm and cold spring fluids collected at Grimsel (Source: Wanner et al. (2020))/ Grimsel groundwater fluids (Source: Schneeberger et al. (2017)), as well as the meteoric water lines (GMWL/ Ticino MWL). Right: BULGG groundwater fluids and the isotopic composition of surface waters and the average precipitation value at the Grimsel precipitation station (Source: Schürch et al. (2003)). 1) Riale di Ronco Stream II (27.06.21), 2) Riale di Ronco mouth (27.04.21), 3) Riale di Gallinoso Stream II (27.06.21), 4) Riale di All'Acqua Stream I (27.06.21), 5) Riale di All'Acqua mouth, 6) Riale di Ronco Stream I (27.06.21), 7) Riale di Ronco Stream IV (27.06.21), 8) Riale di Ronco Stream III (27.06.21), 9) Riale di Ronco mouth, 10) Riale di Bedretto Stream I (27.06.21), 11) Riale di Gallinoso Stream II (27.06.21), 12) Riale di Gallinoso mouth (27.04.21), 13) Riale di Gallinoso mouth, 14) Riale di Gallinoso Stream IV (27.06.21), 15) Ticino River (27.06.21), 16) Ticino River (27.04.21), 17) Ticino River (15.04.21), 18) Precipitation (snow, 04.03.21), 19) Precipitation (snow, 15.04.21), 20) Ronco spring (27.06.21). Not on this plot included are two precipitation samples (rain, both 21.05.21), with the isotopic composition (δ^{18}O/δD) of -5.24‰/-28.25‰ and -5.69‰/-32.24‰.

K - Local Meteoric Water Line Reconstruction

To create the local meteoric water line (LMWL) for the study region, an online isotope precipitation calculator (OIPC) [44] was used. This quantitative approach to reconstruct the isotopic composition of precipitation is based on the location and precipitation altitude. The OIPC allows an estimation of the modern mean annual or monthly deuterium and oxygen isotope composition of precipitation at a specified location. Figure X shows the outcome of the δ^{18}O-δD relationship from a chosen location in the study region at different elevations [45], as well as the BULGG groundwater data. The δ^{18}O-δD ratio was calculated for every 100 m between an altitudes range of 1500 - 3000 m asl and is representing the annual mean. The regression of the OIPC data (gradient: -0.22 ‰ / 100 m) is described in the equation 7.

$$\delta D = 6.988 * \delta 18O + 0.489 \tag{7}$$

The linear regression through the Bedretto data is displayed in the equation 8.

$$\delta D = 6.817 * \delta^{18}O - 1.573 \tag{8}$$

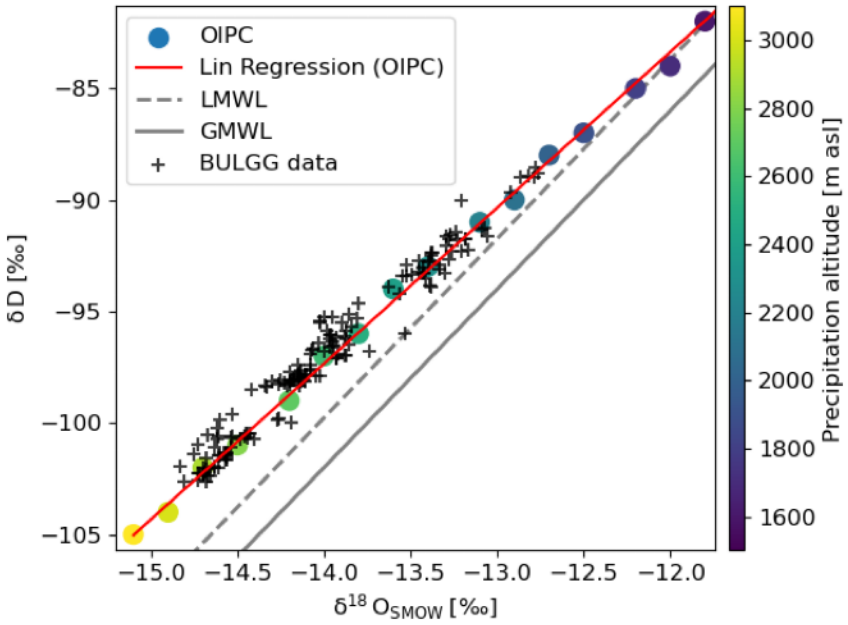

Figure 40: Isotopic diagram showing the calculated OIPC data and its linear regression (dD = 6.988 d18O + 0.489) in relation to the GMWL, LMWL and the Bedretto data.

[44] Bowen, G. J. (2017) The Online Isotopes in Precipitation Calculator, OIPC3.1: `http://www.waterisotopes.org` (accessed in June 2021). The data used by the OIPC are derived from the International Atomic Energy Association/World Meteorological Organization Global Network for Isotopes in Precipitation IAEA/WMO (2015), Global Network of Isotopes in Precipitation, The GNIP Database, Accessible at: `https://nucleus.iaea.org/wiser`.

[45] A sensitivity analysis varying the location in the study region has shown, that the location only causes neglectable changes in the δ^{18}O-δD composition. The reference location for the study region is at 46.527602519N / 8.45550533E, which is the surface projection of the subsurface sampling location at TM 4506.

L - Hydrochemical End-Member Analysis

Table 13: Contribution of each end-member (mixing ratio) to the in the analysis included sampling sites.

Site	**EM1** [%]	**EM2** [%]	**EM3** [%]
TM 440	85.6	12.99	1.5
TM 444	100	0	0
TM 699	1.2	31	67.8
TM 901	0.6	5.4	94
TM 1303	68.8	31.2	0
TM 1306A	61.9	34.1	3.9
TM 1306B	64.4	24.5	11.1
TM 1306C	57.7	26.8	15.5
TM 1494	29.9	10.4	59.7
TM 1798	57.2	36.7	6.1
TM 1973	36.7	0	63.3
TM 1993	11.6	10.9	77.5
TM 2647	22.5	53.4	24.1
TM 2794	32.7	57.8	9.5
TM 2848A	48.7	48.9	2.4
TM 2848B	35.4	49.1	15.5
TM 3191	37.4	44.5	18.1
TM 3192	37.2	41.3	21.5
TM 3750	57.6	42.4	0
TM 3884	36.9	58.9	4.1
TM 4166	33	64.5	2.6
TM 4348	0	88.8	11.2
TM 4447	0	90.2	9.8
TM 4506	17.8	74.9	7.3
TM 4599	19.1	74.6	6.3
TM 4652	12.6	80.3	7.2
TM 4752	22.2	71.6	6.1
TM 4846	28	67	5
TM 4950	8.7	84.8	6.5
TM 5132	6.7	84.8	8.5

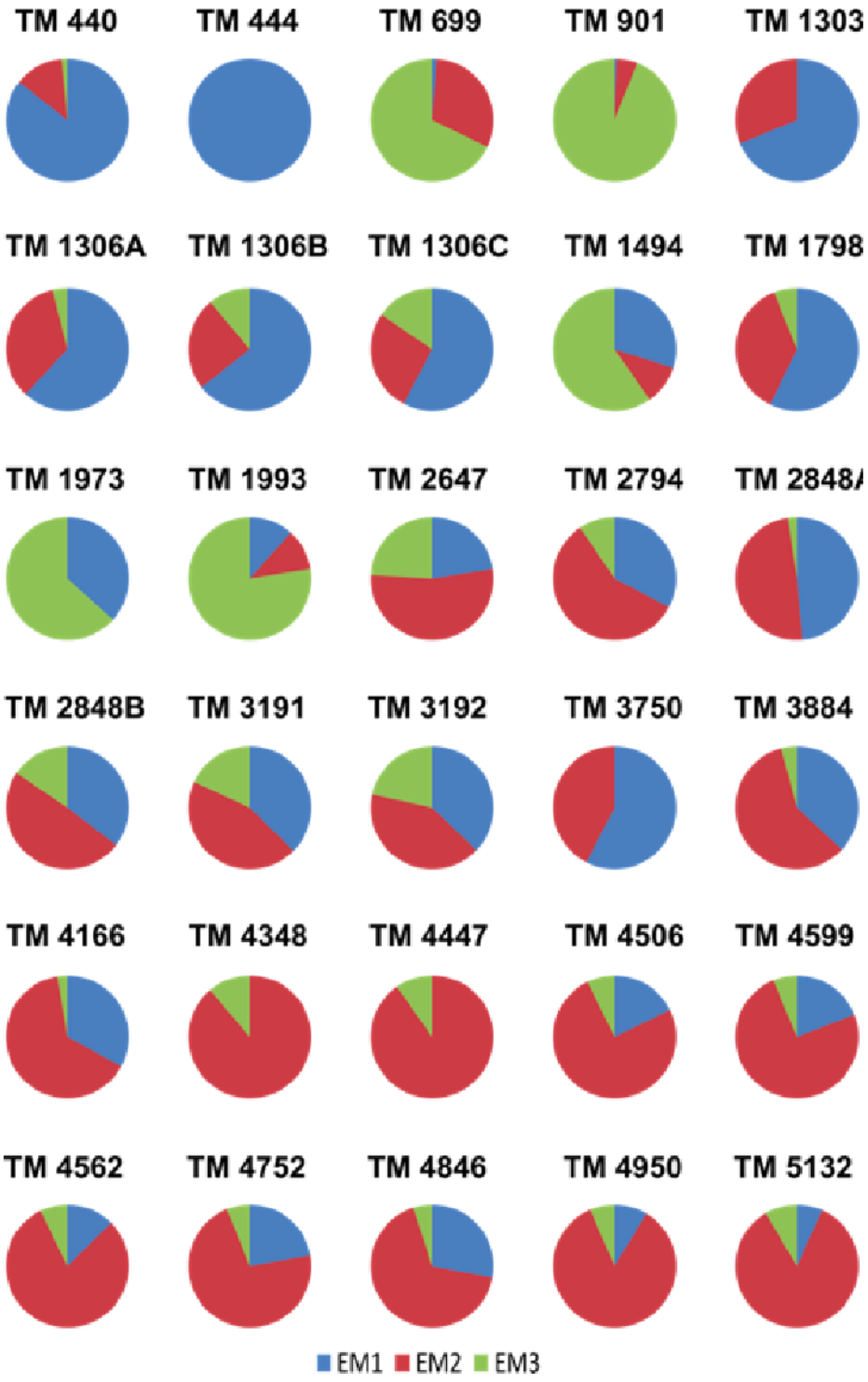

Figure 41: Pie charts showing the contribution of the end-member towards the sampling sites.

M - Timeseries

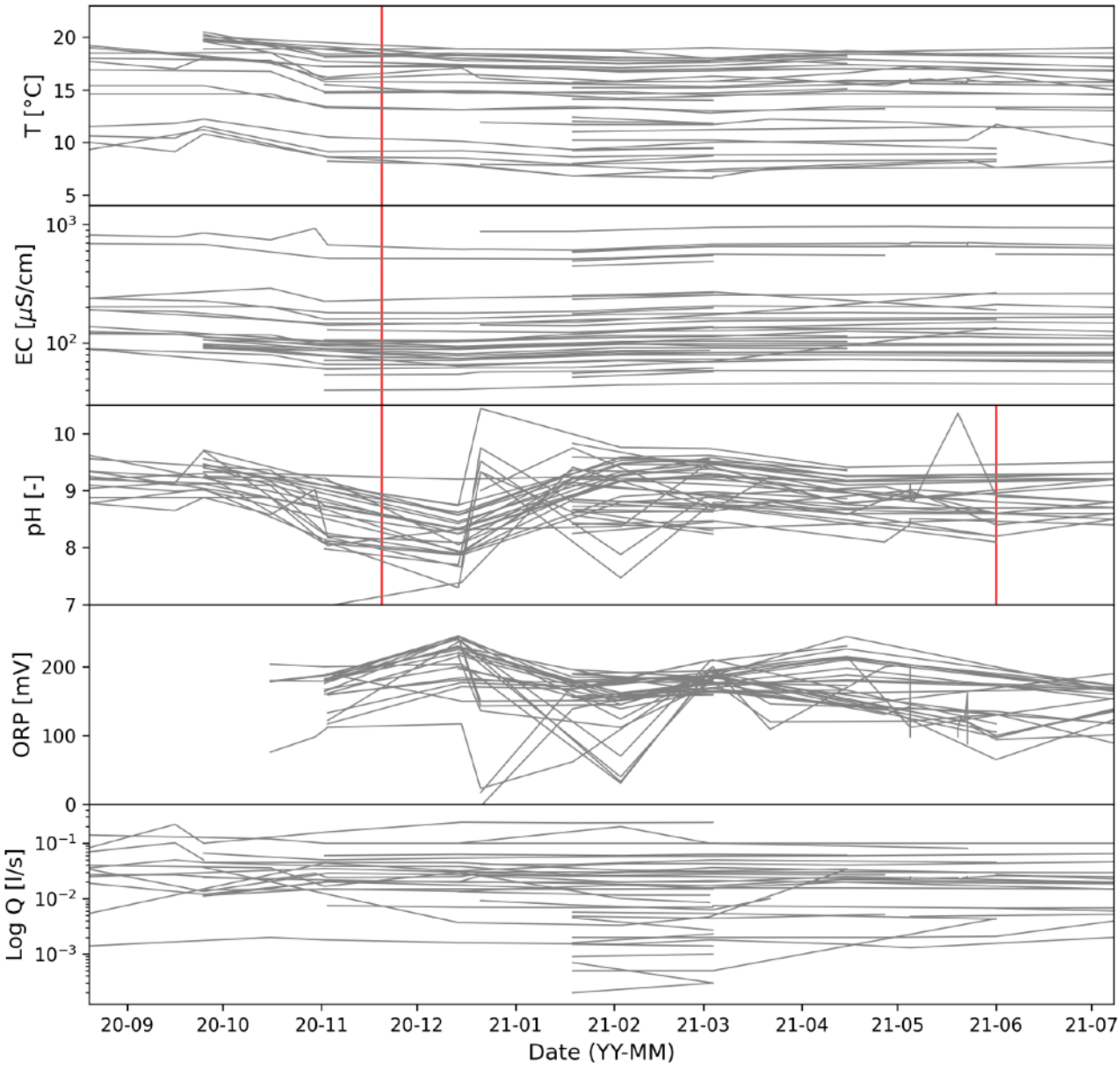

Figure 42: Temporal evolution of each site between August 2020 and July 2021 of the standard water quality parameters.

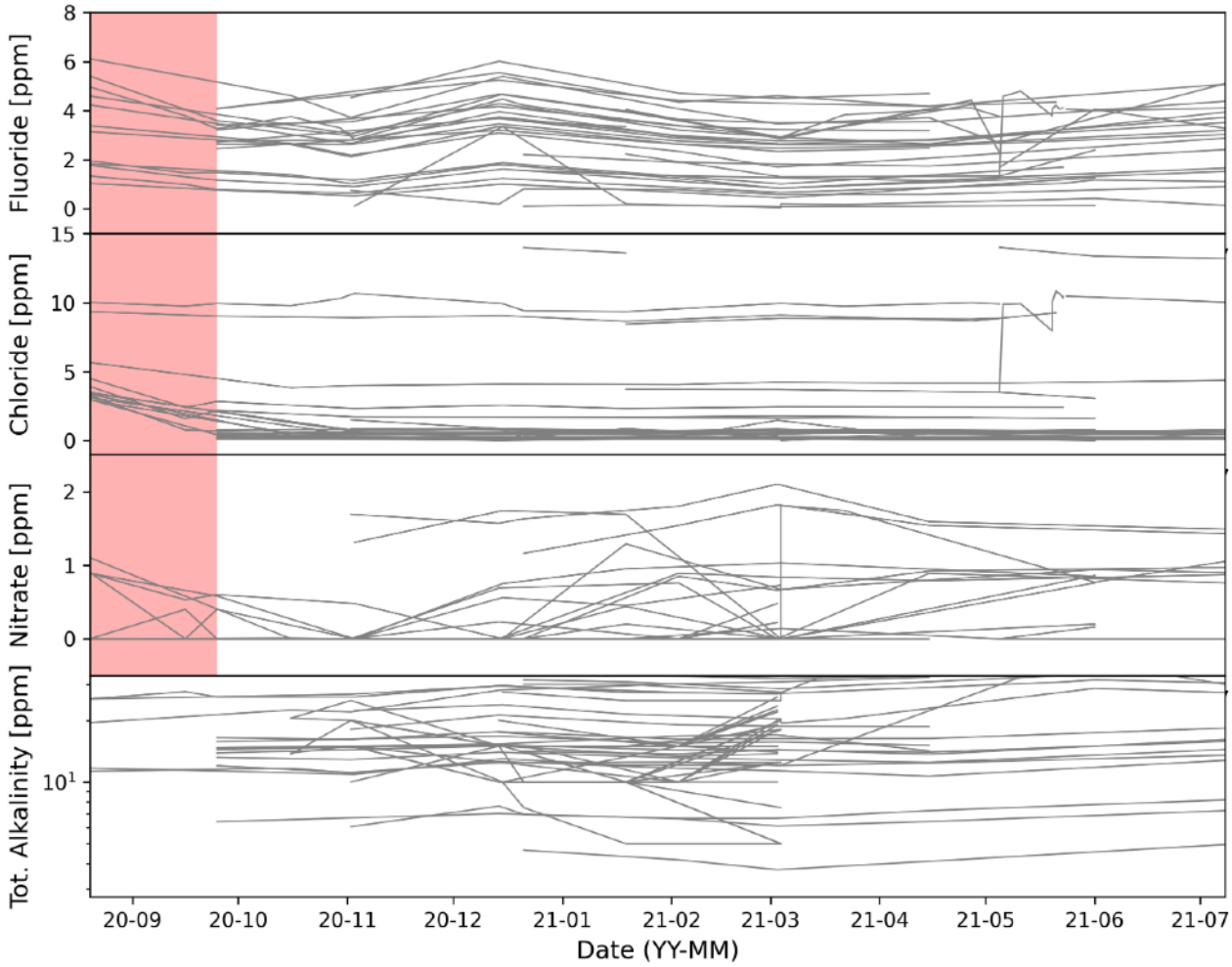

Figure 43: Temporal evolution of each site between August 2020 and July 2021 of the measured anions.

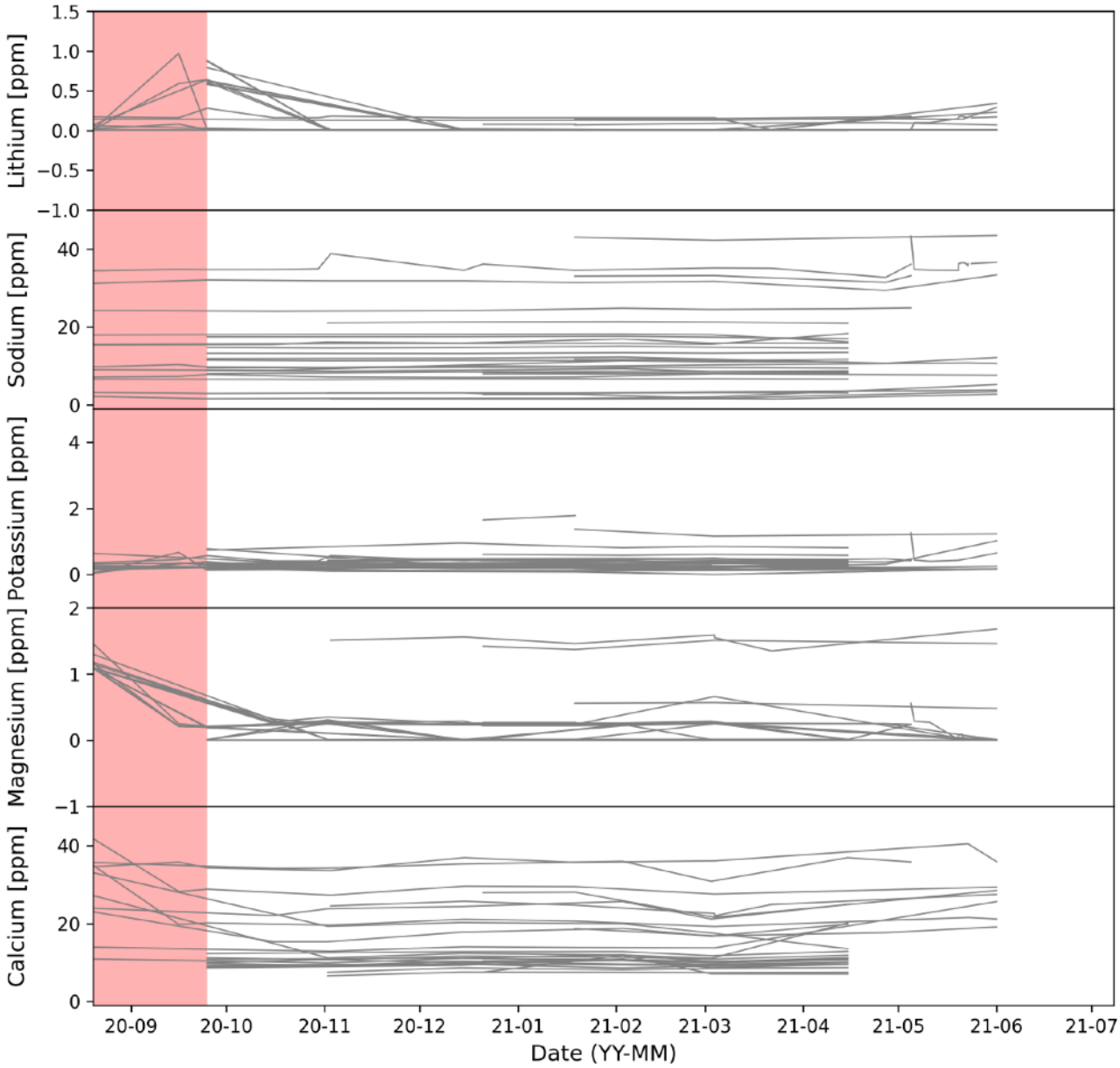

Figure 44: Temporal evolution of each site between August 2020 and June 2021 of the measured cations.

N - Surface Water Composition

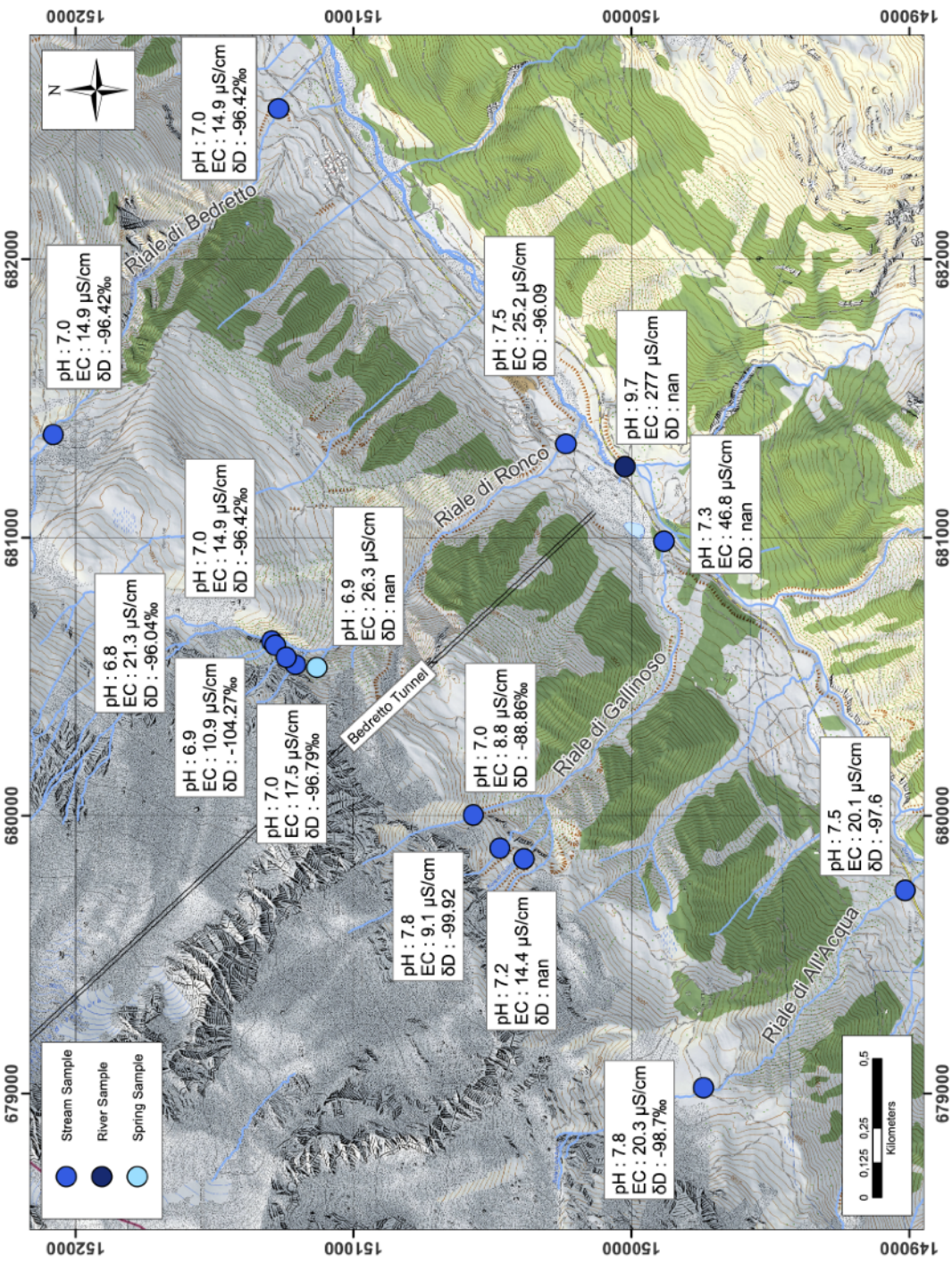

Figure 45: Locations of the sampled streams (Riale di All'Acqua, Riale di Gallinoso, Riale di Ronco, Riale di Bedretto), the Ticino river and the Ronco spring, as well as pH, EC and δD results of the surface survey on the 27.06.21. The distance between the up- and downstream samples is between 1 to 1.5 kilometers.

O - Mixing Concept

Simple mixing problems include a number of end-members, which are mixed together without knowing each contribution factor ('mixing ratio'). The contribution of each end-member can be estimated by linear mixing, as shown in equation 9 (Behrouj-Peely et al., 2020).

$$X_1\delta_1 + X_2\delta_2 + ... + X_n\delta_n = Y_o \tag{9}$$

X_1 to X_n are the different end-members which get mixed. δ_1 to δ_n are the individual mixing ratios, which add up to one.

To be able to estimate the mixing ratios correctly, one needs a conservative (non-reactive) tracer which has an end-member specific concentration. A binary mixing problem can be solved knowing the concentrations of one such a conservative tracer. Each contribution of an additional end-member to the mixture demands for an additional conservative tracer.

P - Suitable Tracers to Detect Mixing Processes at BULGG

Which specific tracer performs best is strongly depending on the surrounding environment. Three major points have to be considered when choosing a hydrochemical tracer: i) the tracer has to exhibit a conservative behaviour, means the tracer does not undergo chemical reactions with the surrounding system (as for example fluid-rock interactions or biological reactions) during the tracer experiment and ii) the tracer concentration should show a sufficient high contrast between the mixed end-members (Christophersen & Hooper (1992); Pelizardi et al. (2017)), iii) the tracer concentration should be estimated with a least amount of uncertainties.

- **Conservative behaviour:** To find a tracer of a non-reactive behaviour, hydrogeological studies often use water constituents like dissolved ions or stable water isotopes. A widely known conservative tracer are the stable water isotopes (δD /δ^{18}O). This is based on the fact, that the stable water isotopes are close to chemically inert, thus do not react with the surrounding system once reached the subsurface (Jasechko, 2019) (Note that this approach does not account for very old and developed groundwater as found in crystalline basement brines, (Kloppmann et al. (2002); Gat (1971))). Another example for a conservative tracer in groundwater studies is chloride. This is based on the fact that the chlorinity is understood be directly linked to the groundwater age, since the Cl^- concentration is often in direct relation with the percentage of incorporated old pore water (Note that this is only valid, if chloride has no additional geochemical source (Wanner et al., 2020)). Major ions are generally seen as non-conservative. Cations are very prone to ion-exchanges, where of the anions only Cl^- (see above) and SO_4^{2+} are reasonably conservative. However, SO_4^{2+} is less conservative than Cl^-, mainly due to its redox sensitivity (loses its conservative behaviour in reducing environments (Tubau et al., 2014)). Standard water quality parameters (T, pH, ORP) are understood to be non-conservative, except the EC (or TDS) which can be a potential conservative tracer if the difference between the two end-members is large enough Choi et al. (2005). However, when estimating potential conservative tracers at BULGG, the application duration is very important. Herein, tracer experiments were conducted on a i) short-term (few days) and ii) long-term basis (over the sampling period of a year). In the short-term experiment, water-rock and biological interactions are likely to be minor, making the requirement for conservative behavior negligible. Long-term monitoring however needs a more careful estimation of a parameters behaviour.

- **Concentration contrast**: A high enough concentration contrast between trageted end-members are exhibited by the following hydrochemcial species (compare table 14, Appendix Q): Cl^-, SO_4^{2+}, Na^+, Ca^{2+}, T, EC/TDS, ORP, (δD), (δ^{18}O)

- **Concentration estimation reliability:** Parameters which are connected to measurement uncertainties have to be excluded in the selection of suitable tracers. In the context of this thesis, this concerns the following parameters: ORP, pH and all ions with a concentration below 10 ppm in the targeted end-members (Cl^-, F^-, NO_3^-, Li^+, K^+, Mg^{2+}).

Taking into account the above mentioned criteria for suitable tracers, the following parameters for the **short-term monitoring experiment** were considered as suitable tracer:

- δD and δ^{18}O (conservative, high contrast, reliable concentration measurement)
- EC or TDS (non-conservative, high contrast, reliable concentration measurement)
- SO_4^{2+} and Ca^{2+} (non-conservative, high contrast, reliable concentration measurement)

The parameters considered most suitable as conservative tracer during the **long-term monitoring experiments** are as follows:

- δD /δ^{18}O (conservative, low to intermediate contrasts*, reliable concentration measurement)

*The stable water isotope baselines between the injection and fracture fluid at TM 1993, as well as the interval fluids of CB2 are generally quite close, making the use of stable isotopes difficult. This is especially relevant for the fluid from the fracture at TM 1993 and CB2 intervals five, since for these sites the mean natural isotopic variability encountered in BULGG fluids (mean std δ^{18}O: 0.077‰/mean std δD: 0.26‰) would exceed the different between the mixed waters.

Q - Hydrochemical Baseline Estimation

The hydrochemcial baselines of the injection fluid (taken from the ditch draining towards the Ronco Portal at TM 2097 and represents an integration of the inflows of the northwestern tunnel part) and the formation water of the ST1 interval 1 + 2, the CB2 intervals and the fracture at TM 1993 are shown in table 14.

Six (of eight) measurements were taken to estimate the baseline values of the injection water during December 2020 and May 2021.[46] The hydrochemical baseline values of the ST1 int 1+2 represent the measurements of the last sample taken after to the hydraulic stimulation works in May 2021 (which represents the highest EC and ion concentrations). The estimated baseline of the fracture at TM 1993 were computed out of five samples taken before November 2020. The CB2 baseline values are representing the measurements taken on the 21.12.2020 (thus after the second stimulation experiment).

Table 14: Hydrochemical baseline of the injection (ditch) water at TM 2097, the formation water of ST1 interval 1 + 2, the fracture at TM 1993 and the monitored intervals of CB2. FM = Field Meter, LG = EC-Logger. * Missing data has been replaced with measurements of samples close to the baseline.

Parameter	**Unit**	Injection Fluid	BH ST1	Frac TM 1993	BH CB2			
			int1+2		int7	int5	int4	int3
F^-	**ppm**	2.2	5.5	3.8	6.6	7.0	-	-
Cl^-	**ppm**	0.3	4.4	10.0	4.4	6.2	-	-
NO_3^-	**ppm**	0.2	0.0	0.00	0.0	0.0	-	-
SO_4^{2-}	**ppm**	14.2	242.0	361.0	55.3	179.7	-	-
Li^+	**ppm**	0.0	0.01	0.2	0.1	0.1	-	-
Na^+	**ppm**	10.7	35.1	34.7	23.8	28.6	-	-
K^+	**ppm**	0.4	0.5	0.4	0.5	0.7	-	-
Mg^{2+}	**ppm**	0.1	0.0	0.4	0.0	0.0	-	-
Ca^{2+}	**ppm**	11.4	86.3	143.8	19.8	72.4	-	-
T	**°C**	15.0	20.2	17.3	16.1	16.3	16.4	16.2
pH	**-**	10.4	-	8.8	9.58	10.24	10.1	10.33
EC	**μS/cm**	86.4	486 (FM) 490 (LG)	699.4*	173.6	377	415	546
TDS	**ppm**	61.4	343.0	497.0*	123	267	295	387
ORP	**mV**	147.0	-13.9*	87	-151	-99	-27	-18
$\delta^{18}O$	**ppt**	-14.25	-13.95	-14.17	-14.11	-14.20	-14.15	-14.01
δD	**ppt**	-98.45	-96.52	-98.04	-96.56	-96.83	-96.88	-96.76

[46] The two ditch samples taken on the 30.04.21 and 04.05.21 were estimated as outliers.

R - EC-logger Data Post-Processing

The continuous measurements with the EC-logger showed higher magnitudes than measured with the field meter. The differences was initially 40 μS/cm, which than increased with an increasing electric conductivity and stagnated at about 75 μS/cm when the baseline was reached. Since all reference measurements were taken with the field meter, the EC-logger measurements were corrected and adjusted to the field meter values. Where calibration data (measurements of the EC-logger and the field-meter at the same time) was missing and large changes occurred, the EC was interpolated (between 22.05.21 at 20:45:31 and 23.05.21 at 07:36:59, CET) using the linear interpolation function from the pandas library.
In a further step, the time series was downsampled using the resampler module from the pandas library. To compute a representative sample the method 'mean' was chosen. This method is computing the mean of groups (excluding missing values) based on the determined sampling frequency. A sensitivity analysis indicated that one sample per 45 minutes is a sufficient sampling frequency to reduce volume without losing information about temporal data trends. Downsampling was performed to obtain a more homogeneous temporal data distribution and to minimize data resolution to reduce data volume.

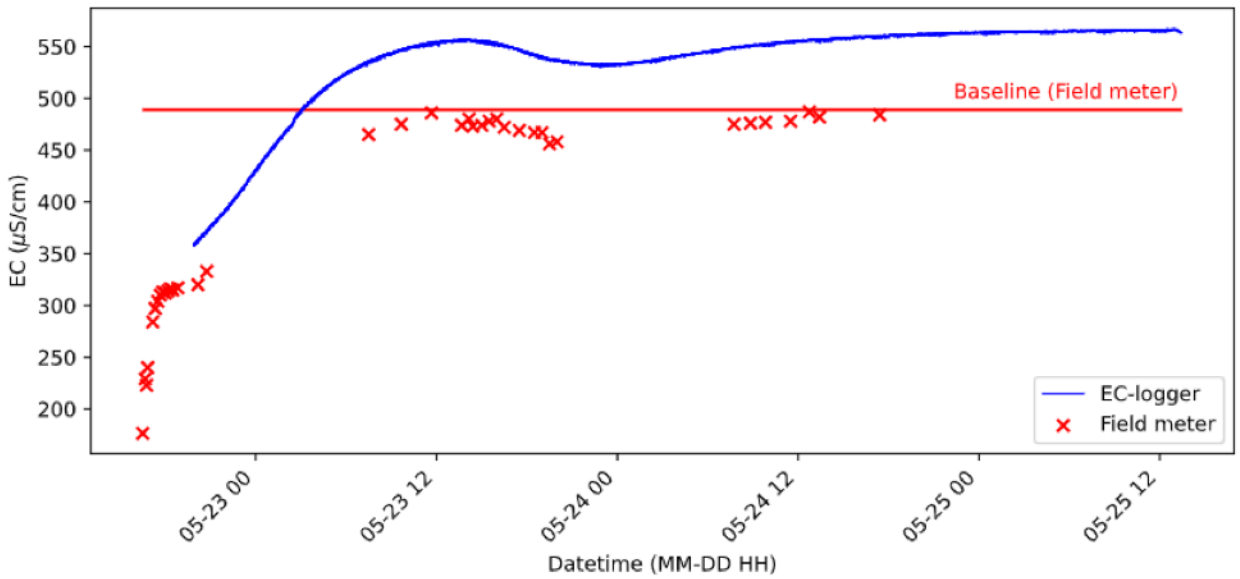

Figure 46: Divergence of the EC-logger data versus handmeter data during the short-term monitoring experiment in ST1.

S - ST1 Log

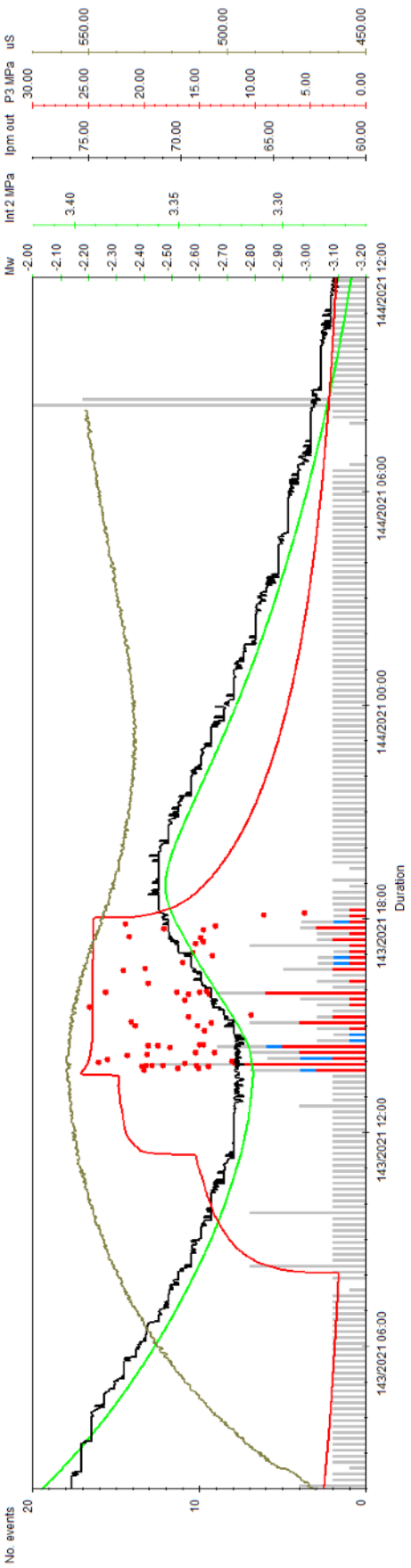

Figure 47: Monitoring ST1 interval 1 during a one day injection in the lower part of ST2. The monitoring includes the down hole pressure of interval 2 (which is hydraulically connected to interval 1), the down hole pressure of the lower part of ST2, the flow rate at ST1 interval 1 (and 2) and the electric conductivity of the outflow at ST1 interval 1 (and 2). The histogram plots show triggers (grey), un-locatable seismic events (blue) and located seismic events (red). The red disks are the located events by magnitude on the Y axis (= number of events). The pressure and flow rate monitoring has been performed by Geo Energy Suisse (GES). The hydrochemical monitoring has been performed by the autor of this thesis. The figure has been compiled by GES.

T - Lab versus Field Measurements

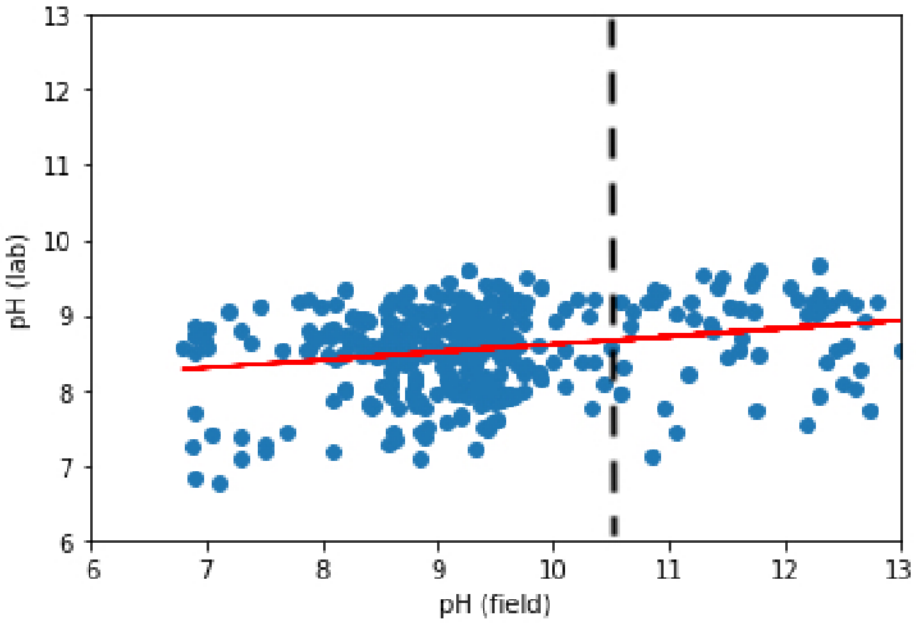

Figure 48: Relationship of the measured field and lab pH values. The r-squared value (0.07) reveals no correlation between the field and lab measurements. Measurements on the right side of the black dotted line are not trusted.

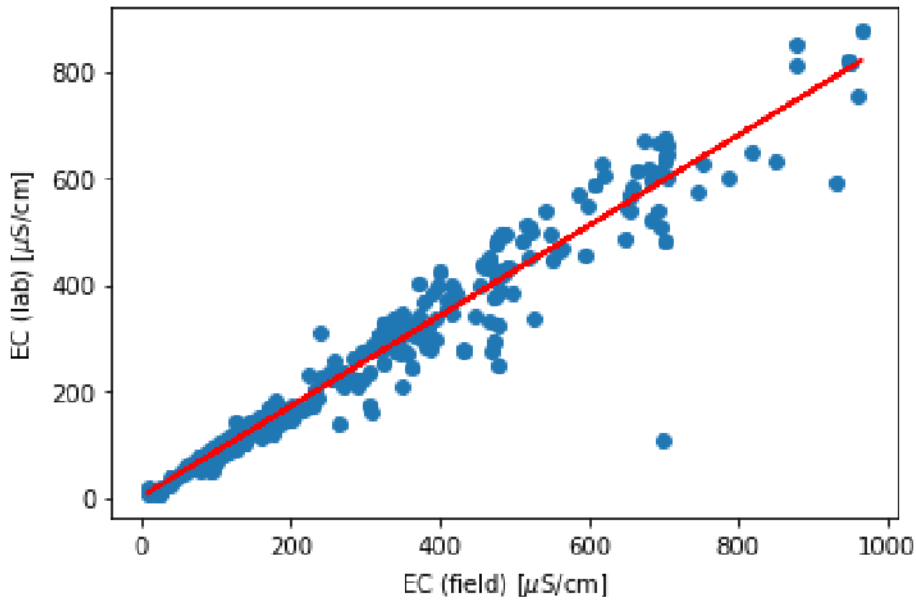

Figure 49: Relationship of the field versus lab EC values measured. The r-squared value (0.95) indicates a significant correlation.